# Synthetic Source Injection in The Dark Energy Survey

*Measurements of the Survey Transfer Function and Applications to Precision Cosmology*

by

Megan Tabbutt

A dissertation submitted in partial fulfillment of
the requirements for the degree of

Doctor of Philosophy
(Physics)

at the UNIVERSITY OF WISCONSIN–MADISON

2023

Date of final oral examination: 12/12/2023
The dissertation is approved by the following members of the Final Oral Committee:
Keith Bechtol, Associate Professor, Physics
Matt Bershady, Professor, Astronomy
Peter Timbie, Professor, Physics
Brian Yanny, Scientist, Fermilab

*In dedication to Chris, Fred, George, and Rocko. My light in the darkest of times. My anchors to reality. The unconditional love that is never predicated on my success or failures. None of this would be possible without you.*[1]

[1]This would also not be possible without Dressler. An inspiration, a role-model, the epitome of the word "teacher", the person who believed in me before I believed in myself. Your impact lives on through your effect on all those lucky enough to have encountered you.

# abstract

Presented here is the Dark Energy Survey's (DES) Synthetic Source Injection (SSI) methodology and applications to precision cosmology for our Year 6 analysis of large-scale structure. Our methodology is predicated on injecting models of real objects obtained from our very high signal-to-noise Deep Field observations into our single-epoch wide field images which are then processed identically to the original wide images. Inherent to this methodology, is that the synthetic sources automatically inherit the same systematics of the real wide field data, a highly sought after achievement for many systematics modeling pipelines that is nearly impossible to achieve from forward modeling techniques alone. In the end, we obtain wide field photometry catalogs of the deep field objects including their inheritance of the systematics. These catalogs are a Monte Carlo sampling of the transfer function of the survey. They can be used for calibration and diagnostics, as well as aid in the calculation and validation of our key project analysis and consequentially our measurement of cosmological parameter constraints through the photometric redshift calibration of the weak lensing sources and the magnification bias estimate for the lens galaxy samples. Both of which are critical to the measurements of the three 2-point correlation functions: cosmic shear, galaxy clustering and galaxy-galaxy lensing, from which we constrain cosmological parameters. This methodology was introduced for our year 3 analysis, and was the first example of using SSI to directly calibrate the cosmological measurements from a wide field survey. The refinement and expansion of the methodology is presented here. Specifically, we improved our mirroring of the wide field image processing pipeline to now fully recreate it. We refactored our code-base to be able to run our SSI at multiple super-computing centers, minimizing wall time and maximizing allocations. We also developed a new injection scheme that injects sources which are preferentially more useful to the

cosmological analyses. These as well as other updates, our initial year 6 SSI results, and their applications to precision cosmology will be discussed at length in this thesis.

# contents

# list of tables

# list of figures

# contribution statement

Most significantly, in December of 2022, I was awarded **Builder Status for the Dark Energy Survey**, where the criterion is as follows: "DES Builders are a subset of DES members and participants who have contributed at least 2 FTE-years of effort on DES project infrastructure or have otherwise made significant contributions to the project." This represents the significant contributions that I have made to the DES project and our scientific achievements. As such, this grants me automatic (opt-in) authorship rights on all science papers based on DES data.

Chronologically: I joined DES in July of 2020, when I started work on infrastructure tasks with the synthetic source injection (SSI) group (Balrog). Coming in on the tail end of the year 3 Key Project, I was able to immediately contribute.

I first participated in the year 3 SSI process by reproducing part of the analysis as an independent verification of the results that were reported in the Y3 paper, which I am a co-author on. Additionally, I contributed to the Y3 Large Scale Structure tasks by using the Y3 SSI data products to provide an independent null test of the Y3 LSS systematics weighting scheme. This lead to being a co-author on the Y3 Galaxy clustering paper as well as the Y3 key project cosmological constraints paper.

In July 2021, I became the co-lead of the year 6 SSI efforts, along with Brian Yanny. One of the main tasks that I undertook was rewriting and expanding the code base to be able to compute at multiple super-computing centers, maximizing allocation and minimizing wall time for running the computationally expensive SSI. This allowed us to push to 5x area coverage in Y6 in order to cover the full footprint. SSI improvements were also made, so as to better reproduce the exact image processing pipeline that the wide field images are processed through, and to create a new injection scheme that makes our SSI realizations more useful for the key project

and science analyses. In conjunction, I continued my work with the Large Scale Structure group continuing to use SSI to mitigate LSS systematics.

In October 2021 I both trained as well as lead on observations of the Euclid Deep Field South which is being used to expand the area of our Deep Field observations for DES Y6.

The following publications are from my direct contributions in Y3 to the Key Project, specifically through the use of Synthetic Source Injection.

**Dark Energy Survey Year 3 Results Co-Author Papers:**

- Measuring the Survey Transfer Function with Balrog [Everett et al., 2022]
- Galaxy clustering and systematics treatment for lens galaxy samples [Rodrí guez-Monroy et al., 2022]
- Cosmological Constraints from Galaxy Clustering and Weak Lensing [Abbott et al., 2022]
- Constraints on extensions to $\Lambda$CDM with weak lensing and galaxy clustering [Abbott et al., 2023]

Unfortunately, the DES Y6 Key Project extends well past the natural timeline of my PhD. In addition, many of the supporting papers for the key project, of which the SSI work I have done plays a key role, are published in batches as they are highly interconnected. This batch publishing for clarity sack on the reader's behalf means that they will also not be coming out for some time, despite my being a co-author on many of them. Finally, DES uses blind analysis techniques to minimize confirmation bias, such that the results of the Y6 analysis won't be known until all of the methodology is complete, validated, and unblinded, an extensive process explained here: [Muir et al., 2020]. Due to all of these compounding

factors, I am unable to share any Y6 results in this thesis and instead turn to the Y3 results as a baseline, where we expect to improve in Y6. In addition, lists of co-authorship and methodology papers have not been finalized. Below I list some of the papers I expect to be named as co-author on. As well, I point the reader to this list of $\sim$30 papers: *https://www.darkenergysurvey.org/des-year-3-cosmology-results-papers/* from the Y3 Key Project as a representation of the scale that we expect Y6 to follow, most of which I expect to have contributed to through my SSI work.

**Dark Energy Survey Year 6 Results First Author Papers:**

- Measuring the Survey Transfer Function with Synthetic Source Injection (in prep)

**Selected (anticipated) DES Year 6 Results Co-Author Papers:**

- Cosmological Constraints from Galaxy Clustering and Weak Lensing
- Galaxy clustering and systematics treatment for lens galaxy samples
- High-precision measurement and modeling of galaxy-galaxy lensing
- Cosmology from Cosmic Shear and Robustness to Data Calibration
- Magnification modeling and impact on cosmological constraints from galaxy clustering and galaxy-galaxy lensing

**Additional Co-Author DES Papers:**

- Expediting DECam Multimessenger Counterpart Searches with Convolutional Neural Networks [Shandonay et al., 2022]

# Part I

# Cosmology within the Dark Energy Survey

# A Cosmological Introduction

A brief introduction to Cosmology, specifically as it pertains to the work presented in this thesis and the Dark Energy Survey.

## 1.1 Introduction

A (very) brief introduction to cosmology is given here. It will be particularly in the context of the work that my thesis focuses on and due to the finite length of the thesis will surely neglect other, very important, cosmology topics. In addition, there are not a lot of derivations in this work, but instead statements of fact and commonly accepted estimations and approximations. I turn the reader to these suggested texts and resources for further details on the topics presented here and other wonderful cosmological areas.

- *A Graduate Level Cosmology Text:* Modern Cosmology by Scott Dodelson & Fabian Schmidt [Dodelson and Schmidt, 2021]
- *An Undergraduate Level Text:* Introduction to Cosmology by Barbara Ryden [Ryden, 2003]
- Cosmology by Michael Rowan-Robinson [Rowan-Robinson, 2004]
- Seeing Red: Redshifts, Cosmology, and Academic Science by Halton Arp [Arp, 1998]
- Cosmology by Nicola Vittorio [Vittorio, 2018]
- Observational Cosmology by Stephen Serjeant [Serjeant, 2010]
- *Article:* Growth of cosmic structure: Probing dark energy beyond expansion [Huterer et al., 2015]

## 1.2 An Expanding, Euclidean Universe

### The Hubble Constant

In 1929, while studying extra-galactic nebulae, Edwin Hubble made his famous, and original, *Hubble Diagram*, figure 1.1. He was measuring the distances to these extra-galactic nebulae, and relating that to their radial velocities which he found using their redshifts. What he found was a roughly linear relationship between the distances and velocities, and although it was later found that the distances were off by about an order of magnitude, the relationship was still valid. This relationship would be named, *Hubble's Law*. More colloquially, this law states that the further a galaxy is from us, the faster it's moving away from us. This is evidence that instead of being in a static universe, we are instead in an expanding one, where the space between us and other galaxies is actually getting larger over time.

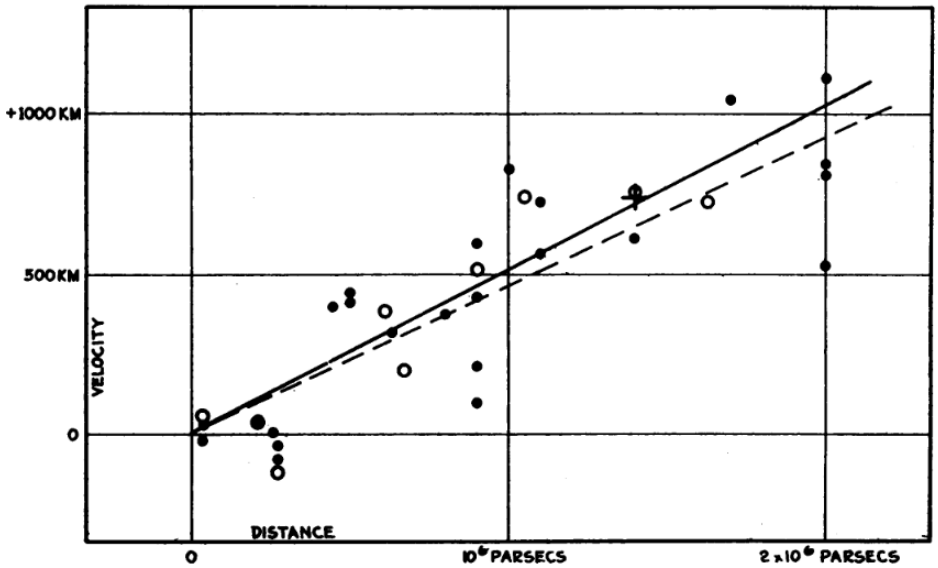


FIGURE 1

**Velocity-Distance Relation among Extra-Galactic Nebulae.**

Figure 1.1: A velocity-distance diagram for extra-galactic nebulae from Hubble's 1929 paper. These are radial velocities corrected for solar motion. You can see a clear positive correlation between distance and velocity. Using this plot, known now as a Hubble Diagram, he was able to estimate a value of the Hubble Constant at 500 km/sec/Mpc [Hubble, 1929].

The universe is expanding, meaning that the distance between us and distant objects was smaller previously than it is now. It is convention to quantify this expansion as a *scale factor*, a. With convention dictating that today, $a = 1$, and previously $a < 1$. As a direct result of this expansion of space-time the wavelength of light from distant objects is stretched, or reddened, on its way to us. We call this effect "redshifted" and this specific cause of the effect is often referred to as a *cosmological redshift*. There are two other common causes of redshifts: gravitational potential, and relative motion, but we will put those aside for now. Redshift is denoted by: z. It can be related to the scale factor as given in equation 1.1.

$$1 + z \equiv \frac{\lambda_{\text{obs}}}{\lambda_{\text{emit}}} = \frac{a_{\text{obs}}}{a_{\text{emit}}} = \frac{1}{a_{\text{emit}}} \tag{1.1}$$

We are interested in the expansion rate of the universe, and we could measure this, for example, by measuring how quickly distant galaxies are moving away from us. We can define the *Hubble Constant*, $H_0$ to be parameterized by a dimensionless number, $h$ such that we arrive at equation 1.2. There has always been some contention with the measurements of the Hubble Constant, which have increased greatly as of late, leading to the "Hubble Tension". Early-time, high redshift, probes, tend to favor lower values of the Hubble constant around $H_0 \sim 67$ km s$^{-1}$ Mpc$^{-1}$, where as low z, or late-time probes are favoring $H_0 \sim 73$ km s$^{-1}$ Mpc$^{-1}$. This is discussed further in section 1.2, but it's important to mention it here, as it motivates putting $H_0$ in terms of $h$, a parameter that we will often factor out as to not need to choose a specific value if $H_0$ right away.

$$H_0 = 100\ h \text{ km s}^{-1} \text{ Mpc}^{-1} = \frac{h}{0.98 \times 10^{10} \text{ years}} \tag{1.2}$$

We would like to quantify the expansion of the universe over time, or in other words, how the scale factor varies as a function of time. The specific scaling of $a(t)$ depends on what regime we are in as we will see. It will be helpful to introduce the *Hubble Rate*, $H(t)$, given in equation 1.3, which measures the rate of change of the scale factor.

$$H(t) \equiv \frac{1}{a}\frac{da}{dt} \tag{1.3}$$

A few examples of this scaling can be seen in figure 1.2. In the early universe, we were in a radiation dominated regime where $a \propto t^{1/2}$. This then transitioned into a matter dominated era where $a \propto t^{2/3}$. In this regime, $H = (2/3)t^{-1}$, and if this was our current era, then $H_0 t_0 = 2/3$, with $H_0$ being *Hubble's Constant*. In general, the relationship between $H$ and $t$ is governed by the Friedmann Equations which we will see in the

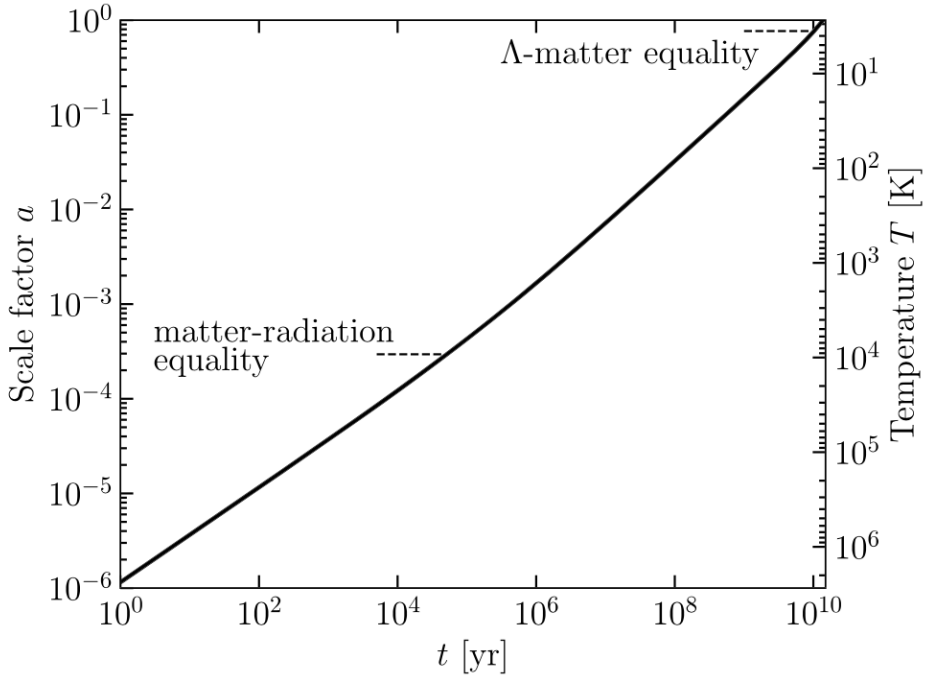


Figure 1.2: The relationship between the scale factor and cosmic time. You can see the dominate components of the universe labeled as well. The relationship between scale factor and time depends on which component is dominating. Starting first with radiation, then matter, and now dark energy ($\Lambda$) [Dodelson and Schmidt, 2021].

following section.

## The Geometry of the Universe

We have just established the fact that the universe is expanding observationally, but let us show that through the context of the geometry of the universe. In cosmology, we are typically most interested in the largest scales of the universe for mapping out the chronology of it. This endeavor is aided in the fact that the universe appears to be very isotropic on large

scales. Meaning that there is no preferred direction, or as we look out in different directions we see the same universe. Put another way, the universe is roughly symmetric on large scales. Furthermore, the universe is also mostly homogeneous on large scales, meaning that there are not preferred locations. There is nothing particularly special about our location in the universe.

We can also examine the curvature of the universe. There are three choices for the geometry of the universe. The first, a flat or Euclidean universe, is one where two objects which start travelling on parallel paths, continue on such paths. In a closed, or positively curved universe, these two initially parallel objects would eventually intersect paths, similar to lines of longitude which are parallel on the equator but both terminate at the pole. Finally, you might have an open or negatively curved universe, where the initially parallel paths diverge such as in a saddle type shape.

It will be helpful if we start introducing some math into our understanding. We first start by defining the metric. This metric will tell us about the distance between two infinitesimally close points in a specifically defined geometry. We start with the Friedmann–Lemaître–Robertson–Walker (FLRW) metric used to describe our universe, given in equation 1.4 in spherical polar coordinates.

$$ds^2 = -dt^2 + a^2(t)\left(\frac{dr^2}{1-Kr^2} + r^2 d\Omega^2\right) \tag{1.4}$$

Given the FLRW metric we can calculate the distance away from some origin that an object is, given in equation 1.5. This distance will depend on the curvature of the universe as parameterized by $K$, in the FLRW metric.

$$d(r,t) = a(t)\int_0^r \frac{dr'}{\sqrt{1-Kr'^2}} = a(t) \times \begin{cases} \arcsin(r) & K = +1 \\ \operatorname{arcsinh}(r) & K = -1 \\ r & K = 0 \end{cases} \tag{1.5}$$

Here, $a(t)$ is the *scale factor*, and $K$ defines the curvature, with a value of 0 representing a flat universe, and $+-1$ representing a positive or negative curvature universe respectively. Furthermore, using equation 1.5, we can define the velocity relationship, given in equation 1.6.

$$v = \frac{\partial}{\partial t} d(r,t) = \frac{\dot{a}(t)}{a(t)} d(r,t) \equiv H(t) d(r,t) \tag{1.6}$$

Where here we see that we have established the linear relationship between the velocity and distance, just as Hubble observed in 1929. Hence, we defined the relationship parameter to be the *Hubble parameter*, as given in 1.7. This is the same relationship we defined above in equation 1.3 and called the *Hubble rate*.

$$H(t) = \frac{\dot{a}(t)}{a(t)} \tag{1.7}$$

We still need to get a handle on the curvature of the universe, however. Luckily, general relativity allows us to relate the curvature of the universe to its energy density which we will see shortly. Let's first start with Einstein's equations from General Relativity, given in equation 1.8.

$$R_{\mu\nu} - \frac{1}{2} g_{\mu\nu} R + \Lambda g_{\mu\nu} = 8\pi G T_{\mu\nu} \tag{1.8}$$

Where, $R_{\mu\nu}$ is the Ricci tensor, $R$ is the Ricci scalar, G is Newton's constant, $T_{\mu\nu}$ is the energy-momentum tensor, and $\Lambda$ is the famous *Cosmological Constant*. Solving the Einstein equations will lead you to the two Friedmann Equations given in equation 1.9 and equation 1.10 which describe a homogeneous and isotropic universe.

$$\left(\frac{\dot{a}(t)}{a(t)}\right)^2 = \frac{8\pi G}{3}\rho(t) - \frac{K}{a(t)^2} + \frac{\Lambda}{3} \tag{1.9}$$

$$\frac{\ddot{a}(t)}{a(t)} = -\frac{4\pi G}{3}(\rho(t) + 3p(t)) + \frac{\Lambda}{3} \tag{1.10}$$

Here, $\rho$ and $p$ describe an energy density and pressure respectively. By differentiating and combining the Friedmann equations above we can derive the continuity equation, given in equation 1.11. This will become important in the following section.

$$\dot{\rho}(t) + 3H(t)(\rho(t) + p(t)) = 0 \tag{1.11}$$

**Constituents of the Universe**

When thinking about the constituents of the universe, or types of energy and matter, cosmologists tend to group these types into three. First, *non-relativistic or cold matter*, *radiation*, and *the cosmological constant*. All these constituents obey the relation 1.12. Combining this with the continuity equation, we arrive at equation 1.13. $w$ is referred to as the *equation of state parameter*.

$$p(t) = w\rho(t) \tag{1.12}$$

$$\rho(t) \propto a(t)^{-3(1+w)} \tag{1.13}$$

An example of non-relativistic matter are stars and galaxies. Interestingly, the largest fraction of cold matter is made up of *dark matter*. This constituent has $w = 0$, so that the density scales with the scale factor as $\rho(t) \propto a(t)^{-3}$ meaning that as the universe expands the density of cold matter decreases. An example of radiation is of course, light, which has an equation of state parameter, $w = 1/3$ and scales as $\rho(t) \propto a(t)^{-4}$. The additional factor in reduction is due to the additional stretching of the wavelength. Finally, the cosmological constant has $w = -1$, meaning that it has a constant energy density for any scale factor, and does not get "diluted" in strength as the the former two constituents did.

Going back to the first Friedmann equation, 1.9, we can see that if we

are in a flat universe, where $K = 0$, then we can solve for $\rho$. We call this the critical energy density, given in equation 1.14.

$$\rho_{\text{cr}}(t) = \frac{3H(t)^2}{8\pi G} \tag{1.14}$$

Furthermore, we can now define a new parameter for each of the constituents called the *density parameter* given by the relation 1.15.

$$\Omega_s(t) = \frac{\rho_s(t)}{\rho_{\text{cr}}(t)}, \quad s \in \{m, r, \Lambda\} \tag{1.15}$$

Where, each of the constituents, matter (m), radiation (r), and cosmological constant ($\Lambda$) are represented by the subscript, $s$. It should also be noted that the critical value for the energy density of the universe today is given by: $\rho_{\text{cr}}(t_0) \sim 10^{-29}$ g cm$^{-3}$.

We can also now write the sum of the density parameters of each type in terms of the curvature parameter, $K$, as given in equation 1.16.

$$\Omega_{\text{tot}}(t) = \sum_s \Omega_s(t) = 1 + \frac{K}{\dot{a}(t)^2} \tag{1.16}$$

Now, from here we can start to see how we are measuring the curvature parameter of the universe. If $\Omega_{\text{tot}} < 1$, then we are in a closed universe, $\Omega_{\text{tot}} > 1$ is an open universe, and $\Omega_{\text{tot}} = 1$ is a flat universe. Within our error of measurement, we believe that we are in a flat universe, measuring $\Omega_{\text{tot}} \sim 1$.

## The Universe Today

### A Cosmic Inventory

We are now going to break down our constituents a bit more and discuss explicitly their currently accepted measured values.

Following our previous equations we can write the density of the constituents that we will be working with as equation 1.17. $\rho_{\text{cr}}$ is a function of the Hubble Constant, which is not as precisely defined today, thus we use the parameterization of the constant in terms of $h$. Thus, any bound on the density of a parameter, $\rho_s$, is in turn really a bound on the quantity, $\Omega_s h^2$. Also note that equation 1.17 assumes that $w_s$ is time-independent.

$$\rho_s(a) = \Omega_s(t)\rho_{\text{cr}} a^{-3(1+w_s)} \tag{1.17}$$

*Photons*. Of the total amount of radiation in the universe, most of that comes from the Cosmic Microwave Background (CMB). Taking this as the total contribution, and using that it is approximately a black-body emitter, along with observational measurements of the CMB's temperature and chemical potential, we can estimate the contribution of radiation to the universe's total energy, which turns out to be quite small, as seen in equation 1.18.

$$\Omega_\gamma h^2 \sim 2.4 \times 10^{-5} \tag{1.18}$$

*Baryons*. As is standard (colloquial) nomenclature in cosmology, baryons include all ordinary matter: nuclei and electrons, despite the fact that electrons are in fact leptons. We decided this was fair, as most of the mass is in the nuclei, and not the electrons, and just group them together. Unlike the photons which were mostly tied up in the CMB which can be modelled relatively easily; baryonic matter is much more complicated. It's tied up in stars and galaxies, dust, plasma, planets, and more. While there has been research aiming to directly "count up" the baryonic matter in the universe, as you can imagine, that is very difficult, has many assumptions, and large error bars. Instead, you can try to be more clever. If you look at the Big Bang Nucleosynthesis (BBN) model, the amount of certain elements that can be formed depends on the abundance of various baryonic matter.

The Planck collaboration constrained the baryon density in 2018, given in equation 1.19 [Planck Collaboration et al., 2020]. While these estimates can vary a bit, this is a good approximation to an agreed upon value. Given an estimation of $h \sim .7$, about 5% of the matter in the universe is baryonic.

$$\Omega_b h^2 \sim 0.0224 \tag{1.19}$$

*Dark Matter*. The majority of matter in the universe is actually dark matter, not the baryonic matter we discussed above (although there is a possibility for "baryonic dark matter", I am not excluding this physical possibility here, I am simply splitting the matter components into "baryonic" and "dark" for ease of nomenclature). Both the idea of dark matter and the overwhelming evidence of such are not new ideas to cosmology. We can't "see" dark matter in the same way we can see the baryonic matter mentioned above. However, its effect can be seen very clearly, in for example, strong gravitational lensing. And indeed, the main method for studying and constraining the amount of dark matter in the universe is through gravity and dark matter's gravitational affect on baryonic matter, which we can directly see. There are several different probes of dark matter, discussed in more depth later, let me just mention here another Planck Collaboration result, which used anisotropies in the CMB to constrain the total matter density parameter, $\Omega_m$ to $\sim 30\%$ the total energy budget of the universe, seen in equation 1.20 [Planck Collaboration et al., 2020]. Combining this with the previous result for the portion that baryonic matter represents, we see that dark matter is $\sim 25\%$ of the total energy budget of the universe, and $\sim 80\%$ of the matter energy budget.

$$\Omega_m h^2 \sim .1431 \tag{1.20}$$

*Dark Energy*. One piece of evidence for dark energy comes naturally from

our discussion up to this point. The substantial evidence that we have for our universe being flat implies we need a total density parameter that sums to one. So far we have photons (and neutrinos) contributing a negligible amount, and matter (baryonic and dark) contributing $\sim 30\%$. So where is the other $\sim 70\%$? Incidentally, this is why it is named "dark energy" it represents the missing 70% of the energy budget of the universe, and we use "dark" in the context of "unknown"; this holds as well for the namesake of "dark matter". Furthermore, we know that the universe is in a state of accelerated expansion from observations, meaning that $\ddot{a} > 0$, such that this constituent's equation of state is negative. This is akin to a negative pressure. Again, there are many probes that are measuring the dark energy contribution: both geometric probes which measure the direct expansion history, as well as measuring the growth of structure in the universe which is affected by the dark energy amount. This will also be touched on again later.

$$\Omega_\Lambda h^2 \sim .35 \tag{1.21}$$

**The Hubble Tension**

Although a bit of a deviation away from the main topics of this section, I would be remiss not to discuss the currently topical issue of the, so called, Hubble Tension. We think of measurements of the Hubble Constant as falling into two categories typically, early-time and late-time probes.

Early probes are looking at the very high redshifted (early) universe, $z > O(1000)$ [Valentino et al., 2021]. The 'Gold standard' in these early time probes is the Planck mission measurements of the cosmic microwave background (CMB) anisotropies. Their full mission measurements of the Hubble constant assuming a base-$\Lambda$CDM Cosmology, is $H_0 = 67.4 \pm 0.5$ km s$^{-1}$ Mpc$^{-1}$ [Planck Collaboration et al., 2020]. Several other early time probes, such as from the Baryon Oscillation Spectroscopic Survey

(BOSS) agree with this lower value of $H_0 \sim 67$ km s$^{-1}$ Mpc$^{-1}$. These probes are also often referred to as 'indirect' probes.

On the other hand, late time probes, or 'direct' probes, are low redshift, and are favoring a Hubble constant value of $H_0 \sim 73$ km s$^{-1}$ Mpc$^{-1}$ . These probes rely on measuring the distance-redshift relation using very specific classes of stars that can be seen at very far distances. This typically includes Cepheid variable stars and Supernova (Type Ia). There have been several well known late-time surveys measuring the Hubble constant including The Hubble Space Telescope (HST), and The SH0ES Project. A summary of some of the early and late time probe measurements can be seen in figure 1.3 from [Valentino et al., 2021].

There are seemingly two possible causes of the Hubble Tension, either there are unaccounted for systematics plaguing one of these two types of probes (or both), or there is unknown physics at the works here. A review of the possible solutions to the tension is given in this reference: [Valentino et al., 2021].

## 1.3 A Brief Cosmological Chronology

We have mentioned what our universe looks like today, but it will be useful here to pause, and review a brief chronological of the universe. A (quintessential) visual representation of this history can be seen in figure 1.4 and we will step through the most pertinent epochs.

### The Very Early Universe

The very early universe starts with the *big bang*, immediately after which is known as the Planck epoch. As time progresses, the four fundamental forces develop. After about $10^{-36}$ seconds the epoch of *inflation* begins, which is a period of extremely rapid, exponential expansion of the universe, ending at around $10^{-32}$ seconds. It is believed that tiny, quantum,

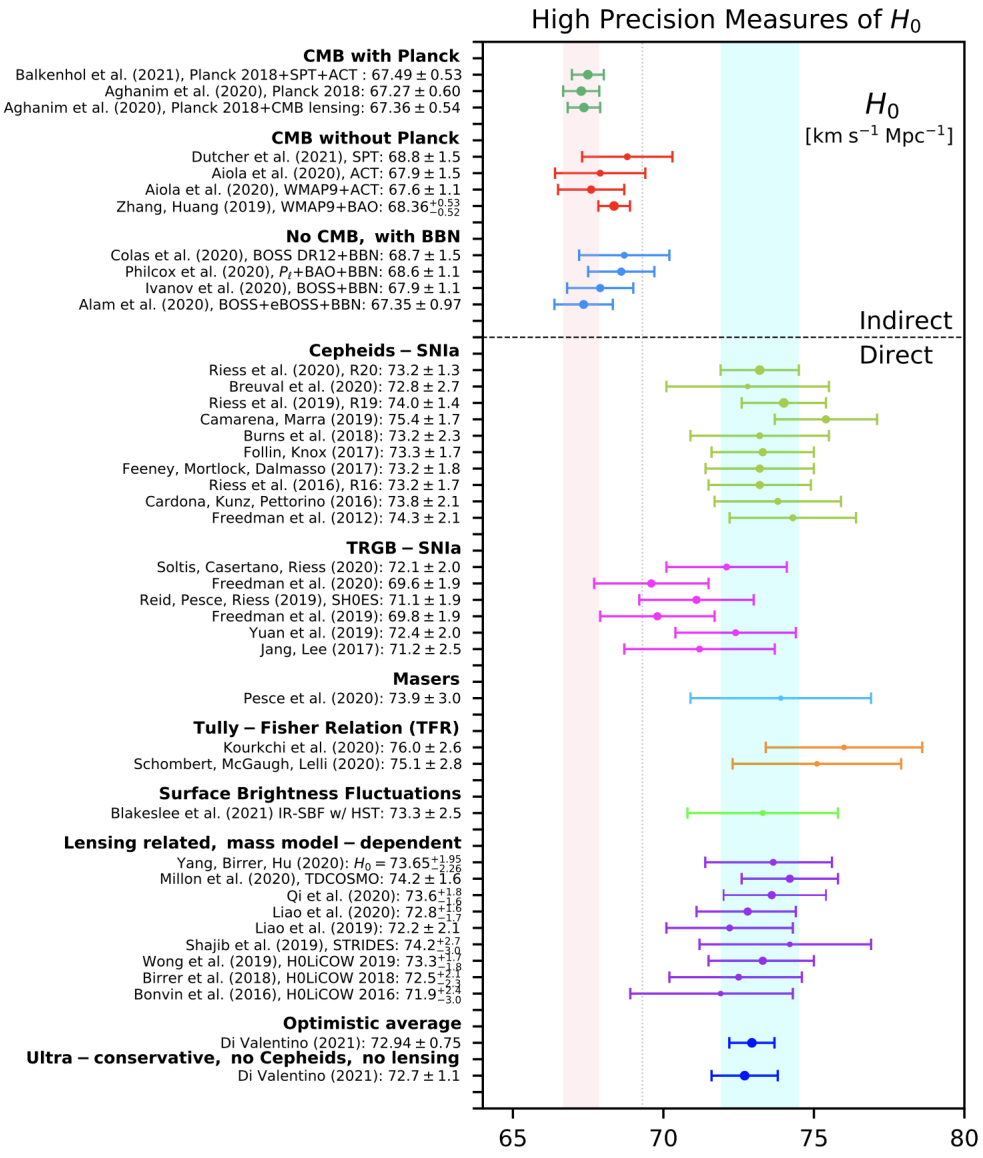


Figure 1.3: Various measurements of the Hubble Constant. There is a clear preference of the direct measurements to tend higher, and the indirect to tend lower. This is known as the "Hubble Tension". [Valentino et al., 2021]

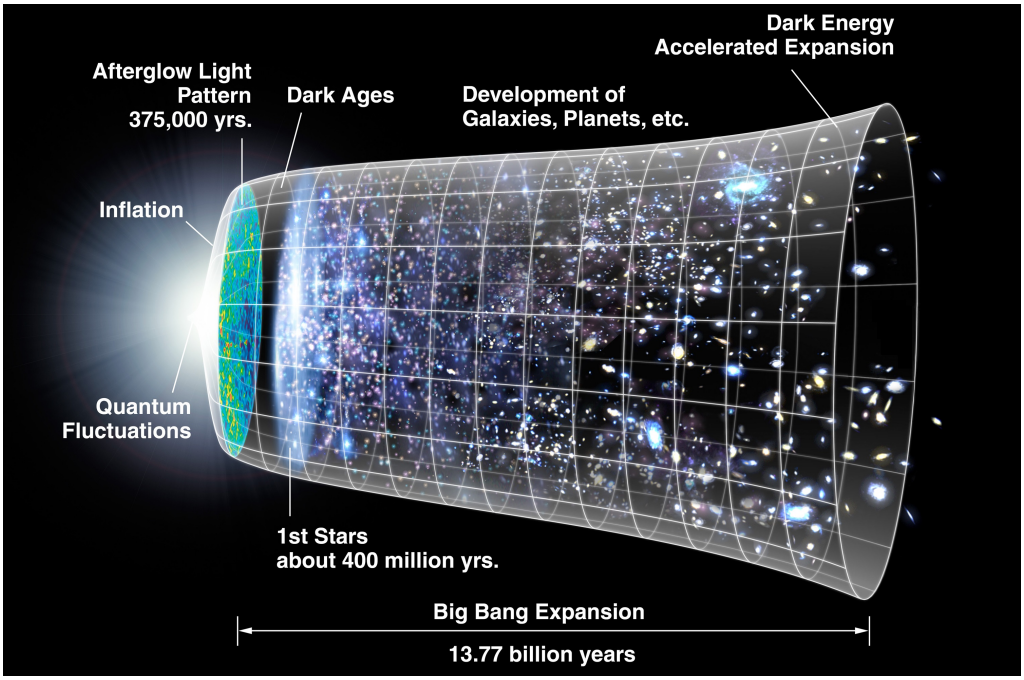


Figure 1.4: A visual representation of the chronology of the universe, made by NASA. Starting on the left hand side time moves forward to the right. Quantum fluctuations in the very early universe grow during inflation and seed the formation of structure in the later universe. The growth of structure can be seen throughout time as well, starting with stars, then galaxies, and clusters of galaxies [NASA, 2012].

fluctuations at this stage seeded the large scale structure that we will observe forming later.

## The Early Universe

After inflation, we begin to enter a period of time with more familiar physics. We are in a period of radiation dominance at this point. Sub-atomic particles are formed, and are thought to be formed in almost equal quantities of matter and antimatter, quickly annihilating and leaving behind the small amount of extra matter we see today. As time continues to

progress, composite particles start to emerge, such as protons and neutrons. At this time the universe was still so hot that any nuclei that were formed were quickly ripped apart by energetic photons.

After about 2 minutes, *Big Bang Nucleosynthesis (BBN)* starts, where the formation of multi-baryon nuclei is now possible. Large amounts of Deuterium are formed which rapidly fuse into Helium-4 and small amounts of Lithium and Beryllium are created as well. At about the 20min mark, the universe has now cooled so much that nuclear fusion can no long take place. At this point, the universe is still too hot to create neutral atoms, or for photons to travel very far, but its too cold for nuclear fusion anymore, thus it's an opaque plasma.

At $\sim$ 50k years we reach the matter-radiation equality where there is so much matter now that it overtakes the amount of radiation in the universe, and we enter a matter dominated era. After this we enter a period known as *recombination*. As the universe continues to cool, electrons start to bind with Hydrogen nuclei to form neutral Hydrogen. Electrons binding to an excited state is more energetically favorable, and thus as they fall to the ground state photons are emitted. This process of photon release is referred to as *photon decoupling*. The decoupling leads to photons being able to travel freely through the universe for the first time and is known as the *Cosmic Microwave Background (CMB)*. This timing corresponds to roughly 380k years after the big bang, or a redshift of $\sim$ 1100.

## The Formation of Structure

From photon decoupling until $\sim$ 400 Million years, is referred to as the *dark ages*. Large gaseous clouds of Hydrogen are forming but are not yet collapsing to create the first stars. During this time the only photons travelling in the universe are from photon decoupling (the CMB) and some 21cm Hydrogen emission. Incidentally, we call this the dark ages as the light from the CMB has already been redshifted out of the visible range

by $\sim$ 3M years. At somewhere between 200M and 400M years, the first stars and galaxies start forming, and are mostly Hydrogen (non-metallic); believed to be forming around dark matter structure that already exists. Between 150M and 1B years (or $20 < z < 6$), we enter a period known as *reionization*. As the gas clouds collapse, some become dense and energetic enough to reionize the Hydrogen gas.

At about 1 Billion years after the Big Bang the universe is finally in a state that is similar to what we know today. Although, it was hotter and denser, with smaller galaxies and clusters in general. After about 10 Billion years, the universe transitions into a Dark Energy dominated era.

## 1.4 Structure in the Universe

One might naively assume that if you looked out into the universe, the galaxies and objects would just be randomly scattered. This is demonstrably false though. There is structure to the universe. In the very early universe, inflation leads quantum fluctuations into density fluctuations. The fluctuations are very small, with over-densities on the order of $10^{-4}$. However, over time these over-densities seed the large structure that we see today. As time marches on, matter accumulates in these over-dense spots due to gravity, and grows. In a universe that is not-expanding, under the force of gravity we would expect these over-densities to grow exponentially with time. If however, you have an expanding universe, that will slow this exponential growth, as the expansion is tending to move particles apart from one another. Measuring (over-)densities is then a way to gather information about the structure and expansion of the universe.

First, let us define a density perturbation, a region in space where there is an over(under)-density as compared to the mean across all space, $\bar{\rho}$, as given in equation 1.22.

$$\delta(\vec{x},t) = \frac{\rho(\vec{x},t) - \bar{\rho}}{\bar{\rho}} \tag{1.22}$$

For a continuous density field, $\rho(\vec{x})$, the two-point correlation function is then given in equation 1.23.

$$\xi(r) = \frac{\langle[\rho(x+r) - \langle\rho\rangle][\rho(x) - \langle\rho\rangle]\rangle_x}{\langle\rho\rangle^2} = \langle\delta(x+r)\delta(x)\rangle_x \tag{1.23}$$

It is also often useful to switch to Fourier space. There we can more easily ask questions about the amount of structure on different scales. We will first express the density as a function of Fourier components given in equation 1.24.

$$\delta(\vec{r}) = \frac{\sqrt{(V)}}{(2\pi)^3} \int \delta_{\vec{k}}\, e^{-i\vec{k}\vec{r}}\, d^3k \tag{1.24}$$

The two-point correlation function in Fourier space can then be written as equation 1.25. Note that, $\delta^{(3)}$ is a Dirac delta function, not a density. Here, $P(k)$ is the *power spectrum*, or the Fourier transform of the two-point correlation function. The power spectrum, aptly named, tells us the amount of power in various scales.

$$\left\langle \delta_{\vec{k}} \delta^*_{\vec{k}'} \right\rangle = (2\pi)^3 \delta^{(3)}(\vec{k} - \vec{k}') P(k) \tag{1.25}$$

Further, we can tie this back around and write the power spectrum in terms of the two-point correlation function. This is given in equation 1.26.

$$P(k) = \frac{4\pi}{k} \int_0^\infty \sin(kr)\, \xi(r)\, r\, dr \tag{1.26}$$

Next, we turn to the *amplitude of mass fluctuations*. The rms amplitude (squared) of mass fluctuations smoothed over a scale, $R$, is given in equation 1.27. Where, $j_1$ is the spherical Bessel function of the first kind, order 1.

$$\sigma^2(R) = \frac{1}{2\pi^2} \int k^2 \, P(k) \, \left( \frac{3j_1(kR)}{kR} \right)^2 \, dk \tag{1.27}$$

This is a very important quantity for observational cosmologists. Specifically, we choose $R = 8h^{-1}Mpc$, and define the quantity: $\sigma_8$. $\sigma_8$ can be measured from clustering and weak lensing and is in fact one of the main cosmological constraints that DES measures. Talked about in more detail in section 2.5. In practice, $\sigma_8$ and $\Omega_m$ are correlated, specifically in weak lensing, as can be seen in figure 2.4, so we typically also constrain the parameter, $S_8$, given in equation 1.28.

$$S_8 \equiv \sigma_8 \left( \frac{\Omega_m}{0.3} \right)^{1/2} \tag{1.28}$$

## 1.5 Cosmological Surveys

There are many different categories of cosmological survey, broken up by the specific cosmology questions they are answering, but also by the physical characteristics of the telescope they are using for the survey. In this section we will explore this space and the trade-offs made with specific choices. This list is not by any means exhaustive and is from a specific view point of the Dark Energy Survey, favoring surveys that we interact with often and which compliment our own.

### Wavelength Range

The first distinguishing feature of different cosmological surveys is the electromagnetic range that the telescope will operate in. Typically these include, optical, radio, infrared, Gamma ray, X-ray, and UV.

The photon collection method for all of these types varies and thus the configuration and construction of the telescope is very different. For

instance, X-Ray telescopes need mirrors capable for reflecting X-rays and oriented in a specific configuration such that they graze the mirrors as they are focused into the collection apparatus. Where as optical telescopes use mirrors, lenses, filters, and CCDs in very similar ways to everyday cameras.

The wavelength range also determines, or rather is determined by, the type of cosmology that you want to study. Optical telescopes are capable of looking at late-times up to a couple z in redshift, this will be discussed at length in the following chapters. Whereas, The Planck Observatory can image from about 300 microns to 11mm, which spans from infrared to radio. A few of their main objectives include mapping the CMB (peak emission $\sim$ 1 mm), bright active galactic nuclei (bright in the radio), and the interstellar medium.

Once a wavelength range (science goal) is determined, the next choice becomes easier. Ground vs Space based telescopes. As seen in figure 1.5, the atmosphere is opaque to some wavelengths. Such that, the next decision will depend greatly on your wavelength range.

## Ground vs Space Telescopes

As referenced above, the first consideration in ground vs space based telescopes is the wavelength range. As can be seen in figure 1.5, the atmosphere is essentially 100% opaque to some wavelengths such as X-ray meaning that if you need a telescope in that range, it is going to be space based, or similar, including balloon-borne telescopes which are lifted above the lower dense regions of the atmosphere.

If you are working in the visible or NIR regions, you now have a choice of ground vs space based. Space based telescopes are primarily limited by their size. The physical size of the telescope corresponds to a mass of payload that needs to be launched. This is restricted by our rocket capabilities and funding. The size of ground telescopes are ultimately

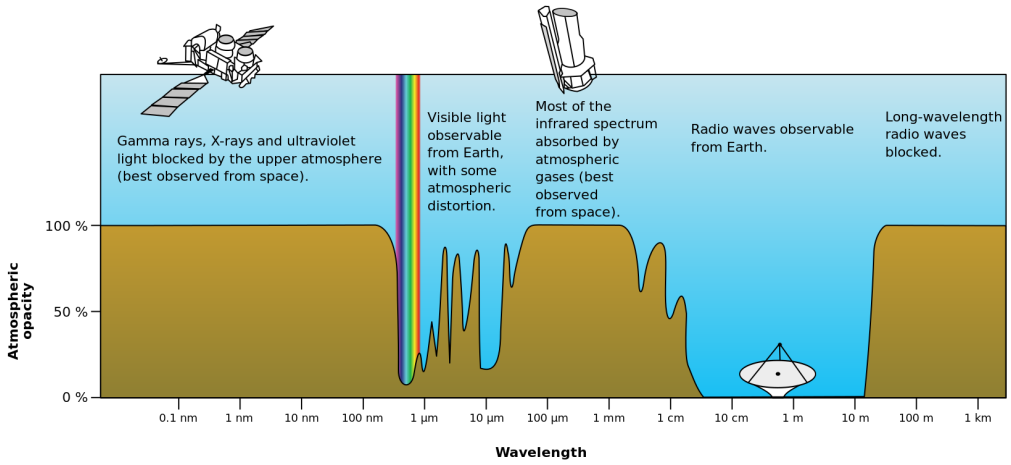


Figure 1.5: A graphic from NASA depicting the atmospheric opacity in different wavelength ranges from the highest energy (shortest wavelength) on the left to the lowest energy (longest wavelength) on the right. Also shown are the different requirements of telescopes: either space or ground based depending on if the atmosphere is transparent to the wavelengths or not. The wavelength range that you are interested in depends on the science that you want to do. (Image Credit: NASA)

limited mostly due to funding as well. In addition, they are restricted, to a lesser degree, by transportation and construction restraints for building on a mountain in the desert (typically). Another significant limitation comes from our ability to develop larger and larger mirrors. Although, some telescopes, like the currently being built Extremely Large Telescope (ELT), are circumventing this issue by having their $\sim$40m primary mirror built out of $\sim$ 800 smaller hexagonal mirror segments. This mirror constraint is also only applicable to optical telescopes, radio telescopes such as the former Arecibo Telescope, due to the diffraction limit at longer wavelengths, have a much smaller precision requirement on their radio reflectors, and thus can be made much larger, $\sim$ 300m in the case of Arecibo. Most radio telescopes are in fact ground based, with a couple notable exceptions which are space based.

There seems to be a clear favor on ground based telescopes being easier to build and being able to be built far larger than space based telescopes. There are no rockets and payload to worry about, so why even launch a telescope into space? The atmosphere. The atmosphere interrupts and distorts light throughout the Visible and NIR regions that we might want to be collecting from. Incredible systems are created in order to account for and correct this distortion including laser guide star systems coupled with adaptive optics to alter mirror shapes in real time. Even with these systems, surveys that use ground based telescopes are constantly needing to account for the atmosphere in their image processing pipelines. The atmosphere and it's affect on images varies as a function of wavelength, so ideally you need to both know the atmospheric conditions as a function of time, as well as the wavelength of light transmitting; and these corrections would be extremely nontrivial to apply to the data. Space based telescopes, however, don't have to deal with the atmosphere at all. The James Webb Space Telescope for instance only needs to reposition it's main mirror every few days to retain focus, as opposed to the constant adaptive optics working on ground based telescopes.

## Spectroscopic vs Photometric

Of particular importance to the Dark Energy Survey's area of cosmology is the difference between photometric and spectroscopic surveys. A photometric survey, like DES, uses broad band-pass filters for collecting wavelength information. An optical photometric survey has typically $\sim$6 filters, through which observations of the sky will be taken. By comparing the flux of an object in each filter color, you can make a very low resolution Spectral Energy Density (SED) for the object. This does not allow us to make very precise estimations of the redshift of an object, though. Spectroscopic surveys on the other hand, use spectroscopy to map out very well defined SEDs for objects, and thus by using well known emission

features, can very accurately assign redshifts to objects. The downside of the spectroscopic survey is that per area on the sky they take a much longer time to image. Here in lies a very important trade-off for galaxy surveys like DES. As a photometric survey, we are able to cover large areas of the sky, taking $\sim 10$ images per location on the sky across bands. These leads to a very large catalog of objects, with low cosmic variance. But at the cost of precision redshift information.

## 1.6 Conclusion

The field of observational cosmology is vast and there are many many efforts to measure cosmological constraints, variations on gravity, mapping the CMB, and so much more. There are a wide variety of telescopes and instruments used as well. I have skimmed just the surface here and in the specific context of the Dark Energy Survey and my work. Next we will get even more specific, and introduce the DES, both from an instrumentation and scientific context.

# 2

# The Dark Energy Survey

An overview of the survey, including the telescope, image processing pipeline, data products, and main cosmological analyses. In other words, how we get from photons to physics.

## 2.1 Introduction to DES

The Dark Energy Survey (DES) is an international collaboration of hundreds of people working across more than a decade of time, making some of the most precise measurements of cosmological constraints to date [DES, 2017]. The survey has mapped hundreds of millions of galaxies, thousands of supernovae, and cosmic structure across ∼5,000 sq. deg. or ∼12% of sky [Sevilla-Noarbe et al., 2021]. One of the main science goals of DES is

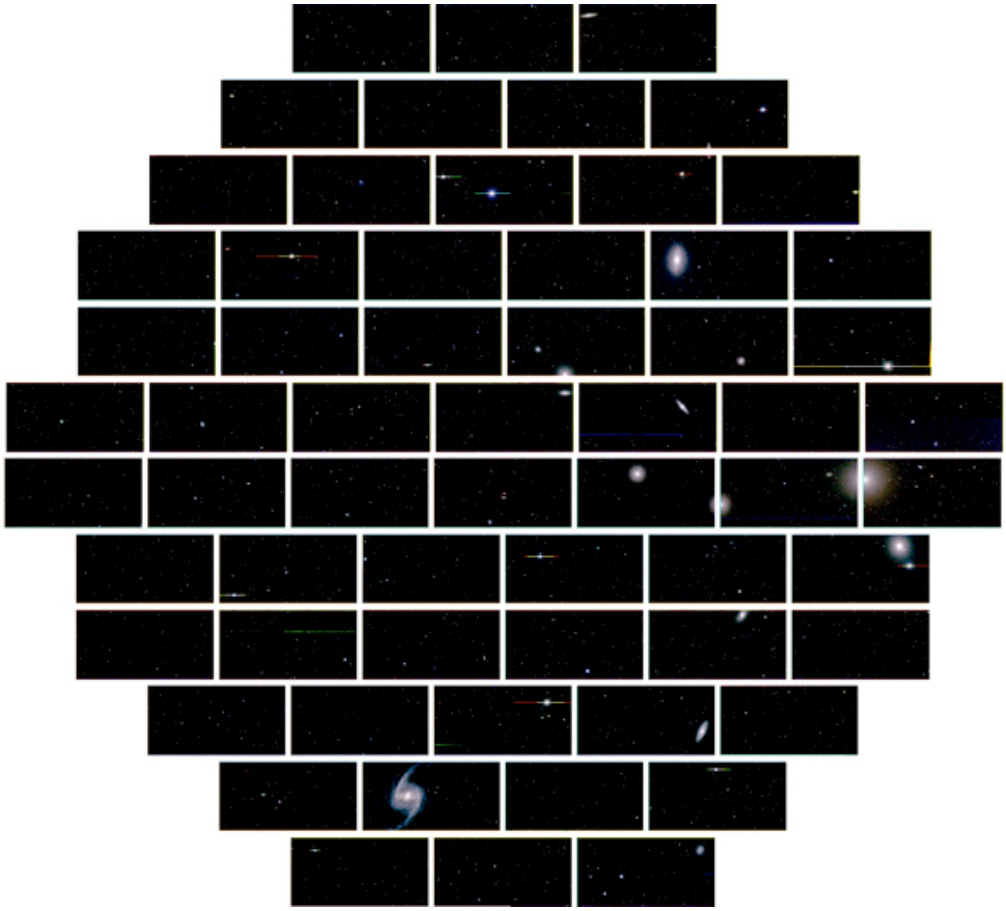

Figure 2.1: An image from the "first light" of DECam and the DES. You can see the individual CCDs. For a sense of scale: about 14 images of the full moon could fit in this one focal plane of the camera. [DES, 2017]

to investigate Dark Energy which is driving the accelerated expansion of the universe.

## 2.2 The Telescope and Survey

### The Telescope and Camera

The telescope that DES uses is located at The Cerro Tololo Inter-American Observatory (CTIO), located south of the Atacama Desert in the Chilean Andes. The peak of Cerro Tololo is 2200m above sea level, where CTIO operates the Víctor M. Blanco 4-meter Telescope used by DES; which as the name suggests, has a 4m diameter primary mirror.

Mounted on the Blanco 4-meter Telescope is the Dark Energy Camera (DECam) [NOIRlab, 2023]. The focal plane of the camera consists of 74 CCDs: 62 used for science imaging, 8 for focusing and alignment, and 4 for guiding. Each of the science CCDs are 2048 x 4096 pixels, and the camera has in total 520 Megapixels. An image obtained using DECam during first light can be seen in figure 2.1 where the CCDs are apparent. The field of view (FOV) is about 3 sq deg.

The wavelength range of DECam is 350–1050 nm, and we image using five filters, in general, g, r, i, z, and Y; spanning the range 400nm to 1080nm, as seen in figure 2.2.

### The Survey

The survey was conducted across 6 years of imaging starting in 2013. There was a main "wide field" survey which consisted of imaging the full footprint, $\sim$5,000 sq deg; and an auxiliary survey called the "deep fields" which imaged small specific regions to a much higher depth. Both of these will be discussed in the following sections.

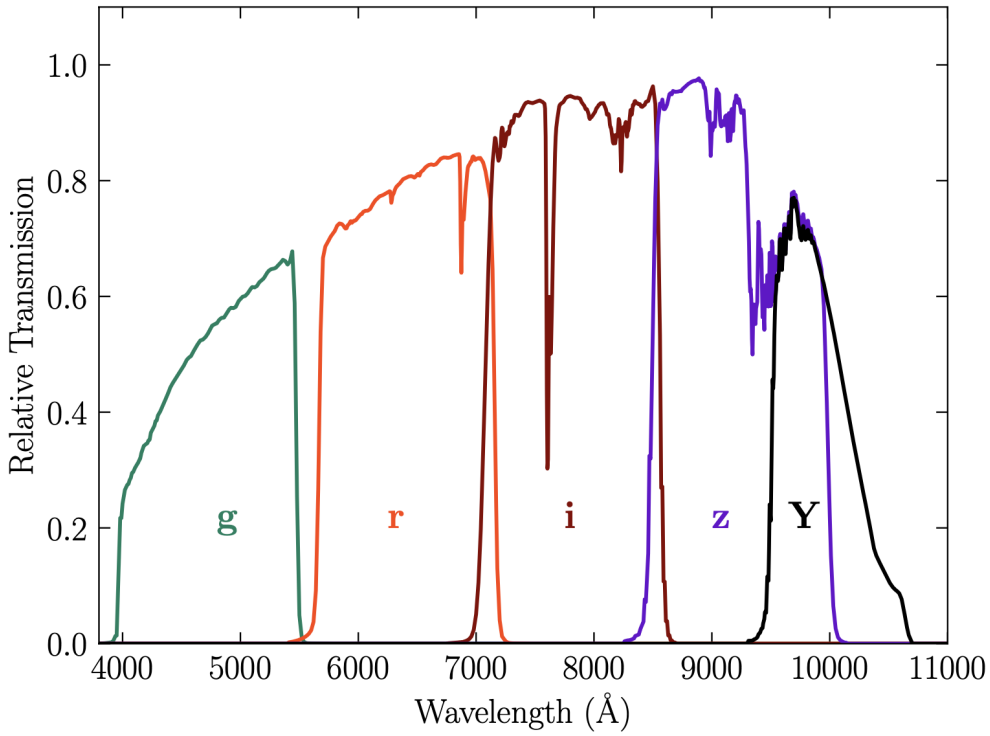


Figure 2.2: The relative transmission rate for the 5 standard band-pass filters on the DECam, g, r, i, z, and Y. They span most of the optical range, as well as some NIR [The Dark Energy Survey Collaboration, 2018].

## The Wide Field

The shallower, wide field (WF) survey consisted of covering a ∼5,000 sq deg contiguous footprint in the southern high Galactic latitude sky. The shape of the footprint, seen in figure 2.3, was very intentional, not intentionally tank shape, but intentional. The plane of the Milky Way can be seen in the solid black lines, with the galactic pole marked by a "+". A large portion of the survey is far away from the galactic plane and the galactic center (marked with an "x"). The bottom cuts off to avoid the Magellanic clouds shown in grey. The bottom portion of the footprint also overlaps with the South Pole Telescope Survey (SPT). And the top stripe

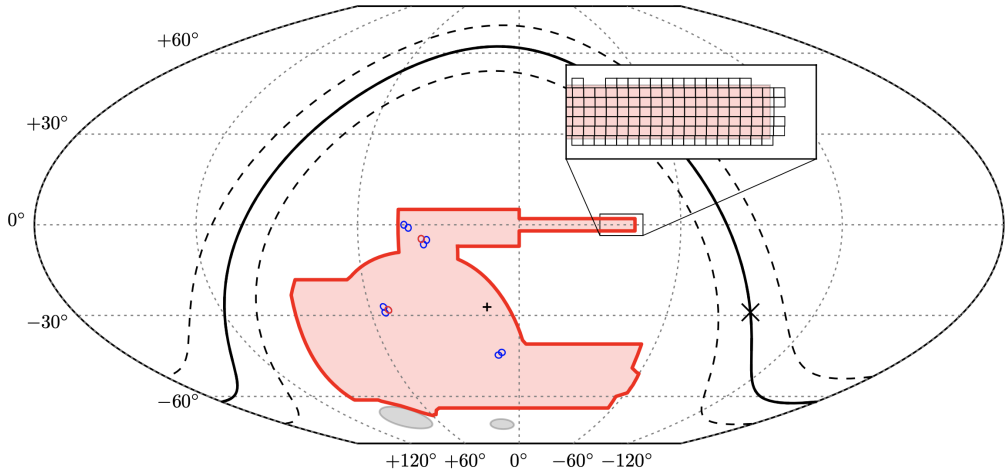


Figure 2.3: A plot of the DES footprint in celestial coordinates. The black plus in the center is the southern galactic pole, with the solid black line being the Milky Way plane. The Large and Small Magellanic clouds are in grey. There are 10 Deep Fields pointings shown in blue and red around the footprint. In addition, the inset shows the tiling pattern that we use, where each rectangle is one "tile" a unit of area that we use to break the footprint into manageable handling and computing sizes [The Dark Energy Survey Collaboration, 2018].

is known as *Stripe 82* which overlaps with the Sloan Digital Sky Survey (SDSS) [Abbott et al., 2021].

The WF survey consisted of 90-second exposures in the griz bands, and either 45 or 90 second exposures in the Y band for Y1-Y3 and Y4-Y6 respectively. Each position on the sky was typically observed 7-10 distinct times in each of the griz bands [Abbott et al., 2021]. Each of these exposures uses the 62 CCDs previously mentioned. For each specific exposure, we refer to each image from a CDD as a *single-epoch* (SE) image. The pointings are dithered such that the gaps between the CCDs are covered. The single-epoch exposures are combined into *coadd tiles* to achieve a deeper image. While a single epoch (CCD) image is 2048x4096 pixels, a coadd tile is 10,000 x 10,000 pixels, or .5338 sq deg [Abbott et al., 2021]. More about the

coadding process will be discussed in section 2.3.

The public release of the Y1-Y3 data is referred to as Data Release 1 (DR1), and the public release of the Y1-Y6 data is DR2. Internally, the data catalogues and analyses were broken down into three eras, Y1, Y3, and Y6. We also internally release a "GOLD" catalog for each era that is a sub-sample of the total data reflecting quality cuts that create a high precision cosmological sample used for science. This catalog creation process will be discussed more later in this chapter.

Y1 is not so relevant in the context of this thesis. Instead we will focus more heavily on Y3 and Y6. Having joined DES and the Synthetic Source Injection project towards the end of Y3, much of our discussion will relate to the shift from Y3 into Y6, including changes and upgrades, as well as the key projects of Y3 and Y6. As was mentioned previously, there is a public data release for Y1-Y3, DR1, of which the Y3Gold sample is a subset. Similarly, there is a DR2 public release of data (Y1-Y6), of which the Y6Gold is a sub-sample.

**Y1**

Y1 consisted of the first year of data covering about 1800 sq deg, with 3-4 images per band per observed location. More details about Y1Gold can be found in: *Dark Energy Survey Year 1 Results: The Photometric Data Set for Cosmology* [Drlica-Wagner et al., 2018].

**Y3**

In the first Data Release, covering Y1-Y3, $\sim$5,000 sq deg was covered. The median depth in magnitudes of the coadded catalog was: g = 24.3, r = 24.1, i = 23.4, z = 22.7, and Y = 21.4. Where this depth is defined for a 1.95 arc-second diameter aperture at a signal-to-noise ratio of 10 [The Dark Energy Survey Collaboration, 2018]. This data release contained about 400 Million objects in total, with $\sim$310M galaxies, and $\sim$80M stars. More details

about the general Data Release 1 can be found in *THE DARK ENERGY SURVEY DATA RELEASE 1* [The Dark Energy Survey Collaboration, 2018]. The Y3Gold sample was created from the Y1-Y3 data and served as the the cosmological sample. More about this specific sample is discussed in section 2.4.

#### Y6

Y6 covered the whole footprint, with 83,706 wide-field exposures, resulting in ∼18TB of coadded images. The median depth in magnitudes of the coadded catalog was: g = 24.7, r = 24.4, i = 23.8, z = 23.1, and Y = 21.7, about half a magnitude deeper than DR1. The galaxy sample was ∼543M objects and the stellar sample ∼145M. More information about Data Release 2 can be found in *The Dark Energy Survey Data Release 2* [Abbott et al., 2021]. The Y6Gold sample is currently being finalized from the Y1-Y6 data and will serve as the cosmological sample for the Y6 analyses.

### The Deep Fields

The Deep Fields (DF) also referred to as supernova fields or deep drilling fields, are a very special ancillary campaign run by DES, and absolutely critical to our cosmological analyses. These fields can be seen in figure 2.3, as the blue and red circles, which are actually specific pointings of DECam. There are four regions shown inside the DES footprint, named SN-[S, X, C, E]. C and X have three pointings each, while S and E have two. There is one additional pointing outside the footprint, not shown in figure 2.3, which is the COSMOS field, which lies inside the COSMOS footprint in the northern galactic hemisphere. Importantly, these 11 fields overlap with other surveys, which allows us to obtain spectroscopic and many-band photometry for the objects that we image. This is a quintessential piece that allows us to tie our less precise 5-band wide field photometry to well

known high precision redshifts. Deep fields will provide us with a catalog of objects with very well known redshifts and distributions that we can then use Synthetic Source Injection to map to the wide field. This process will be discussed further in chapter 5.

The 11 Deep Fields cover ∼30 sq deg, reaching a maximum i-band depth of 26.75 measured with a 2 arc-second diameter aperture at a signal-to-noise of 10. You can contrast this with the Y6 Data Release i-band magnitude depth of 23.8. It's this fact, of the deep fields being much deeper and thus having a much higher signal-to-noise per object compared to the wide field, that lets us treat these objects' measured properties as "truth" in our injection process. More specifics about the Deep Fields can be found in *Dark Energy Survey Year 3 Results: Deep Field Optical + Near-Infrared Images and Catalogue* [Hartley et al., 2021]. In addition, the specific Deep Fields catalogs will be discussed more in section 2.4.

## 2.3 Image Processing Pipeline

**Note:** There have been changes to the image processing pipeline over the course of the survey. This section will focus on the current pipeline that is relevant in Y6, and any changes to this pipeline that are pertinent to this thesis. More details about the pipelines and changes can be found in the Data Release and Photometric Data Set papers [The Dark Energy Survey Collaboration, 2018, Abbott et al., 2021, Drlica-Wagner et al., 2018, Sevilla-Noarbe et al., 2021].

### Preprocessing

Starting on the mountain top, the observation schedule is handled by an electronic software that optimizes based on the survey plan, current observing conditions, and previous data collected. Preprocessing is a set of initial processing steps that are not image specific, but rather general.

After the initial step of correcting for cross-talk, the PIXCORRECT[1] code is used for bias subtraction, correcting non-linear pixel response, bad pixel mapping (from faulty hardware in the camera), saturated pixel masking, and flat-fielding, among other various calibrations, detailed here: [Morganson et al., 2018].

## First and Final Cut

The first cut pipeline processes images within hours of being taken, specifically to identify if they pass science quality minimums, or need to be added into the queue to be taken again on following nights. Initial astrometric solutions for the single-epoch (SE) images are calculated using the SCAMP software [2] utilizing SExtractor[3] (Source Extractor) catalogs of bright objects in the SE images. Next, we mask saturated pixels and the associated bleed trails, fit and subtract the sky background, mask cosmic rays and satellites, and model an initial point spread function using PSFEx[4]. Finally, single-epoch SExtractor catalogs are created, and the science quality of the images is evaluated to determine if they need to be re-imaged [Morganson et al., 2018].

The final cut pipeline is run well after observations, and is used to assemble the final data products for release. While very similar to the first cut there are code changes as well as calibration changes between the first cut and final cut pipelines. In the final cut, the images are photometrically calibrated using the Forward Global Calibration Method (FGCM) [Burke et al., 2017] which uses overlapping exposures and calibration stars to calibrate across the whole survey [Morganson et al., 2018].

[1] A DES specific code
[2] Part of the AstrOmatic Software suite
[3] Part of the AstrOmatic Software suite
[4] Part of the AstrOmatic Software suite

## Multi-Epoch Processing

Taking multiple exposures at the same point on the sky (typically between 7-10) and *coadding* the images is critical for DES science. The coaddition results in more information than from just a single image, and creates a deeper image overall. For instance, in the DR2, the single-epoch i-band magnitude limit at a signal-to-noise of 10 was 22.78, where as the coadd i-band magnitude limit at the same signal-to-noise was 23.8, a full magnitude deeper [Abbott et al., 2021]. The coaddition process, and specifically taking multiple images of the same regions of the sky at different points in time allows us to better distinguish faint objects from background noise.

The first step is to break the sky into coadd tiles, 10,000 x 10,000 pixels in size, or 0.7306 degrees per side. They are tiled on the sky in rows of constant declination, and there is approximately 1 arc-minute of overlap between tiles. This can be seen visually in figure 2.3.

Astrometric solutions are rerun per tile, by running SWARP on all single-epoch images in a particular tile simultaneously which allows for a more consistent solution across images, and a minimized coadded PSF. With the astrometric solution recalculated for the whole tile, the single-epoch images can be mapped to their correct position and overlaid pixel by pixel, keeping only good pixels (unmasked), in order to create the coadd, which is done using SWARP. In addition to the separate grizY coadded images, a special detection coadd image using r, i, and z bands is made (g and Y are omitted due to their much broader PSFs and more noisy backgrounds). SExtractor is run on this detection image to create the tile's master source list. PSFEx is then used to create PSF models for the 5 individual bands as well as the detection coadd.

### Coadd Catalog Creation

The detection coadd image (which is an riz composite), is used to locate sources which have a signal-to-noise above a specific threshold, $\sim$10. SExtractor is then run with two image inputs, the detection coadd, and the band specific coadd; using the detection coadd to define the location of the sources, the photometry is extracted for those sources from the band specific coadd. This photometry catalog is the main Data Release catalog that I have been referencing, Data Release 2 in this instance, which comprises all 6 years of observations. The photometry values recovered from SExtractor include: MAG_AUTO, MAG_PSF, FLAGS, ALPHAWIN_J2000_DET, DELTAWIN_J2000_DET, and more [Morganson et al., 2018]. While this is the basis catalog, there are more measured quantities for these objects that get added to this catalog, as well there are more data products in general that are made from this master source list.

## Data Products

One of the most important supplementary data products made is the Multi Epoch Data Structure (MEDS) files. A MEDS exists for every object in the coadd detection image. Specifically there are MEDS files for each band, and within that for each source in the coadd detection master list, there exists postage stamps (small individual source cut-out images) which include the band specific coadd as well as all of the single-epoch images corresponding to that source's location. In addition, there are postage stamps of the weight, mask, background, and segmentation maps, which divide images into disjoint outlines of pixels surrounding each detected object. Where the segmentation map was obtained from SExtractor. Finally, they also contain models of the local PSFs.

For our Gold science sample, Y6Gold, we measure additional photometric and shape parameters for the object catalogs. In Y6 the model

fitting parameters were obtained using the Bulge-Disk-Fixed-scale-ratio (BDF) method. This fitting method fits all single-epoch images of an object simultaneously and returns the fitting parameters: flux, size (T), shape (2 component), and fracDev (the fraction of light in the bulge vs disk).

Another change that was made in the Y6Gold catalog was the use of PIFF PSFs [Jarvis et al., 2020]. As light from distant sources passes through the atmosphere, it experiences wavelength dependent distortions, also called chromatic aberrations. A new PSF modelling technique was incorporated into DES processing in order to better account for this effect as well as mitigate another major issue that PSFEx wasn't. Namely, discontinuities of the PSF across chip boundaries. PIFF (PSFs in the Full FOV), works in sky coordinates instead of image coordinates which allows it to interpolate the PSF across CCDs simultaneously as well as to account for astrometric distortions better. PIFF is also a color-dependent model, meaning that the solution of the PSF depends on the object's color.

## 2.4 Catalogs and Samples

### The Gold Catalog

The Gold catalog for a given analysis cycle (Y1, Y3, or Y6) is the core catalog used for cosmological analyses. It is derived from the more broad Data Release catalog, DR2 in the case of Y6Gold, but with cuts applied as well as additional information added, such as BDF photometry, and more.

Nominally, the Y6Gold catalog contains all the same objects as the DR2 catalog, however, there is a special mask defined, called the Y6Gold Footprint, that when applied, gives you the subset of DR2 that is considered Y6Gold, which is the photometric data-set used for cosmology. Here, I will define how we made the Y6Gold Footprint mask. The mask is defined in heal-pixels at a resolution of NSIDE $= 4096$ [Gorski et al., 2005]. In order

for a pixel to be included in the masked region, three conditions must be met. First, for each band, griz separately, the fraction of high-resolution pixels that have been observed needs to be greater than .5; stated another way, the fraction of the 4096 pixel that has been observed in each band needs to be greater then 50%. Second, The combined coverage in all four bands is greater than 50%. Finally, there are at least two exposures for each band.

There are additional masks that get created and can be applied depending on the cosmological analysis that is using the Gold catalog. Here I will list the two that are usually always applied. The first is a foreground mask, referred to as FLAGS_FOREGROUND, which masks out regions containing bright foreground objects. The mask contains flag bits representing the situation that gave rise to the flag including, bright GAIA or 2MASS stars, bright galaxies, Milky Way satellites, etc. A second mask that is created is the bad regions mask, FLAGS_BADREGIONS, which contains bits denoting the reason it got flagged, such as failures in the PSF fitting, errors from the BDF photometry fitting, high density of anomalous measurements, etc.

## Survey Property Maps

Observing conditions are tracked across the footprint as well, referred to as survey property maps. Some of the various conditions tracked include: exposure time, airmass, sky variance, detection fraction, and many others. These maps will become very important to the Large Scale Structure analysis and the Y6 Key Project as a whole. In general, these survey property maps are critical to re-weighting our galaxy populations. Differences in observing conditions such as airmass and exposure time can create a boost or dampening in observed galaxy number that needs to be corrected for as it's not representative the true universe. I also did some cross-group collaboration between LSS and Synthetic Source Injection

regarding these maps that will be addressed in section 9.1.

## The Deep Fields Catalog

### Y3 Deep Fields

The Y3 Deep Fields catalog is the fiducial input catalog that we are using for the Y6 Synthetic Source Injection project. The Y3DF catalog was created using three of the supernova fields (C3, E2, and X3) as well as the COSMOS field. Those four resulted in 5.88 sq deg, and 1.6 Millions objects after masking. The $10\sigma$, 2 arc-second aperture i-band magnitude depth of the four fields ranges from 25.04 to 25.54 mag. For the images, there is a depth resolution trade off. In the deepest coadd, DEEPEST, the highest possible signal-to-noise image is created by stacking a large number of exposures, however, this results in the largest effective resolution (FWHM). COADD_TRUTH is less deep, and was created for the Synthetic Source Injection project in Y3, and targeted a depth that is 10x the depth of the wide field survey that we would be injecting these "truth" deep field objects into. Finally, there exists the shallowest coadd images, SE_TRUTH, which has very good seeing, better FWHM and exposure times than 90% of the wide field survey. More information on the Y3 Deep Fields can be found in *Dark Energy Survey Year 3 Results: Deep Field Optical + Near-Infrared Images and Catalogue* [Hartley et al., 2021], as well as section 4.

### Y6 Deep Fields

The Y6 Deep Fields are still being constructed and validated as of writing this thesis, but the hope for the Y6 DF was to increase the area coverage, from 10 fields in Y3 to 14 in Y6. Part of this effort involved observing in the Euclid-Deep-Field-South region, which I was a part of. Since we did not use the Y6 DF as input to our Y6 SSI effort (we used Y3 DF), I

encourage the reader to check out the Y6 DF paper once it is published for more details.

## Galaxy Samples

In order to do the Y6 Key Project and many other ancillary projects, we will need to define specific galaxy samples. Here will focus on two types of galaxy samples, the more distant source galaxy sample, and the foreground, lens galaxy sample. Named as the light from the source galaxies gets gravitationally lensed through the intermediate matter before arriving to us.

### Source Sample

In Y3 the weak lensing shape catalog (or source catalog) was created using the metacalibration technique. In Y3, out of the ∼390M objects, ∼100M made it into the shape catalog. The cuts include those to mitigate stellar contamination, PSF errors, and several others in order to optimize the sample. The same mask that will be applied to the lens samples is applied here and brings the total area down to 4143 sq deg. The source galaxy catalog is broken into 4 redshift bins as seen in figure 2.6. More details about the shape catalog can be found in: [Gatti et al., 2021b].

### Lens Galaxy Samples

For Y3 there were two lens galaxy samples created, RedMaGiC and a larger, optimized sample: MagLim. MagLim become the fiducial Y3 lens sample.

**RedMaGiC** The RedMaGiC sample is sub-selected from the Gold catalog by the RedMaGiC algorithm which selects Luminous Red Galaxies (LRGs) with high quality photometric redshift estimates [Rozo et al., 2016]. In

Y3 RedMaGiC is broken into five tomographic (redshift) bins as follows: $z = [0.15, 0.35, 0.50, 0.65, 0.80, 0.90]$, where the bin edges have been chosen by prioritizing minimal redshift overlap between non-consecutive bins. These bins can be seen in figure 2.6. Overall there were 2.6 Million RedMaGiC galaxies in the Y3 sample. After applying masking the final area covered in Y3 was 4143 sq deg [Rodrí guez-Monroy et al., 2022].

**MagLim** The second lens galaxy sample used in Y3 is the MagLim sample. It was designed to have a simple selection criteria but optimized for constraining power in the 3x2pt analysis (discussed in the following section). More information about the optimization of the sample can be found in [Porredon et al., 2021]. The series of cuts on the Gold catalog are as follows. First, a set of quality cuts to remove poorly measured objects and processing failures. Second, a cut to remove stars. Next, a cut to preferentially include bright galaxies. Finally, another cut to remove residual stellar contamination and other bright objects. This sample is broken into six tomographic bins: $z = [0.20, 0.40, 0.55, 0.70, 0.85, 0.95, 1.05]$, which can be seen in figure 2.6. Overall, there were 10.7 Million MagLim galaxies in Y3, again covering 4143 sq deg [Rodrí guez-Monroy et al., 2022].

## 2.5 3x2pt Analysis

The 3x2pt analysis, also known as the Key Project (KP), is a large-scale structure analysis that combines three 2-point correlation functions, the combination of which leads to a measurement of the clustering amplitude, $S_8$, and the matter density, $\Omega_m$ in $\Lambda$CDM, and dark energy equation-of-state parameter, $w$ in $w$CDM [Abbott et al., 2022].

There are two different galaxy samples that we have access to and can extract information from, the distant source galaxies and the nearer

lens galaxy sample. From this there are two quantities we can probe, the distant shear field, and the nearer galaxy density field. In order to gather information about these two fields to constrain cosmology, we calculate three two-point correlation functions: cosmic shear, galaxy clustering, and galaxy-galaxy lensing. Each of these will be discussed in the next sections, followed by the final combination of the three and subsequently the results and cosmological constraints we achieved in Y3.

## Cosmic Shear

Cosmic shear, also known as weak (gravitational) lensing, is the coherent distortion of distant source galaxy shapes due to the intervening matter. It's an element of large scale structure and is sensitive to both dark matter and dark energy. As well, it serves as both a probe of geometry through the lensing kernel which is a function of both $H_0$ and angular scale, and the growth of structure and its redshift evolution. While rich with information and constraining power, as a statistical measurement of millions of galaxies on the percent level, it's a very difficult measurement to make. The shapes of galaxies can be contaminated by systematic effects that need to be modeled and accounted for. Blending effects especially in crowded fields need to be modeled using image simulations. And the interpretation of the shear signal depends on accurate redshift distribution estimations, which in turn depends on synthetic source injection, through the redshift calibration methodology discussed at length in chapter 7.

The 2-point shear correlation function estimator is given in equation 2.1, where $\epsilon_t$ is the tangential shear and $\epsilon_x$ is the radial shear of a galaxy. It's calculated as a function of separation angle $\theta$, and across redshift bins, $i, j$.

$$\xi_{\pm}^{ij}(\theta) = \langle \epsilon_t \epsilon_t \pm \epsilon_x \epsilon_x \rangle(\theta) \tag{2.1}$$

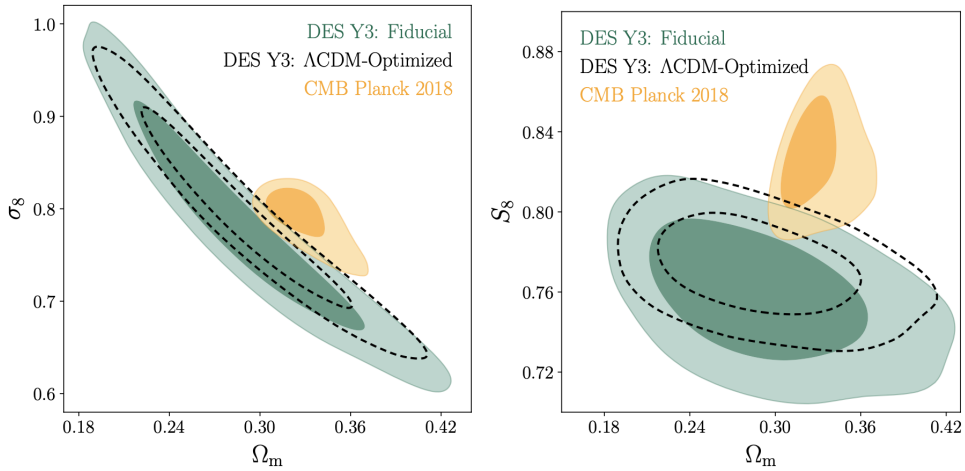


Figure 2.4: Cosmological constraints from the DES Y3 Cosmic Shear analysis are shown. The green shaded area is for the fiducial Y3 Shear analysis, with the dotted lines representing an analysis performed with scale cuts that optimize the ΛCDM model. CMB Plank results are shown in yellow in comparison. For all, 68% and 95% confidence levels are shown [Amon et al., 2022, Secco et al., 2022].

The cosmic shear correlation function can be expressed in terms of the convergence power spectrum, which itself depends on the lensing efficiency kernel, which depends on the combination $H_0^2\Omega_m$. The convergence power spectrum can also be expressed in terms of $\sigma_8$ which is degenerate with $\Omega_m$. More details about the calculations and methodology can be found in the Y3 Cosmic Shear Papers [Secco et al., 2022, Amon et al., 2022]. The results of this analysis from Y3 can be seen in equation 2.2 and in figure 2.4. Where you can see the tendency of our late time probe to favor lower $S_8$ than Planck, an early time probe.

$$S_8 = 0.759^{+0.023}_{-0.025} \quad \Omega_m = 0.290^{+0.039}_{-0.063} \quad \sigma_8 = 0.783^{+0.073}_{-0.092} \tag{2.2}$$

## Galaxy-Galaxy Clustering

The galaxy-galaxy clustering 2-point correlation measures the distribution of matter in large scale structure, using galaxies as the tracer of the matter density field. Galaxies are a biased tracer of this underlying matter density filed, and thus that bias needs to be accounted for. On top of this true bias, we also have an observational bias of the galaxies themselves. There are spatially varying survey properties which can impart a clustering signal in addition to the true cosmological signal. We need to account for this erroneous signal and re-weight the galaxies that we observe to undo its effect.

The observed projected galaxy density contrast, or rather the excess galaxy clustering above what you would expect randomly, is given in equation 2.3, for redshift bin, $i$, position $\hat{n}$, and co-moving distance, $\chi$. The first term represents the line-of-sight projection of the three-dimensional galaxy density contrast. The second is a contribution from linear redshift-space distortions (RSD) and the third is a magnification contribution. Galaxy density can be related to matter density through a linear model: $\delta_g = b\delta_m$, where $\delta$ is a density fluctuation away from the mean. Furthermore, the bias, $b^i$, is a function of redshift bin, $i$.

$$\delta^i_{g,\text{obs}}(\hat{n}) = \int d\chi \; n^i_g(z) \frac{dz}{d\chi} \; \delta^{(3D)}_g(\hat{n}\chi, \chi) + \delta^i_{g,\text{RSD}}(\hat{n}) + \delta^i_{g,\mu}(\hat{n}) \tag{2.3}$$

The goal here is to calculate $n^i_g(z)$, but as stated before this can be influenced heavily the survey conditions. A poor seeing night will result in a lower number of galaxies being observed, not from a cosmic origin but from a systematic one. Thus we re-weight the galaxies in order to undo this artificial and systematic effect.

The full re-weighting procedure is described in detail in The Dark Energy Survey Year 3 Results: Galaxy clustering and systematics treat-

ment for lens galaxy samples [Rodrí guez-Monroy et al., 2022]. In short through an iterative process, Iterative Systematics Decontamination (ISD), the correlation of a survey property map with observed galaxy density fluctuations is calculated and corrected for. In the second iteration, the next most influential map is calculated and corrected for. This continues until a threshold of influence has been obtained. There is also special consideration taken, so as to not over-correct and subsequently lower the clustering signal artificially. Once the overall re-weighting map is obtained, it's applied to the lens galaxy samples and the angular correlation function calculation can proceed. The results of this re-weighting can be seen in figure 2.5, where the red contours represent an unweighted galaxy sample, and the blue and yellow represent re-weighted galaxy samples. We are not making a statement about a true vs false $\Omega_m$ here, but rather just demonstrating how heavily the measurement of the parameter depends on the galaxy weighting of the sample. There is an extensive validation of this weighting scheme discussed at great length in the paper. As well, Synthetic Source Injection can be used to validate the weight scheme, which is discussed in detail in section 9.1.

## Galaxy–Galaxy Lensing

The last 2-point correlation function that becomes part of the 3x2pt analysis is the galaxy-galaxy lensing correlation: the cross-correlation of lens galaxy positions and source galaxy shapes. The amount of distortion (shape and magnification) of the source galaxies is correlated with the lens galaxy distribution which (biasedly) traces the foreground matter distribution and dark matter large scale structure. This correlation provides a connection between the two previously mentioned correlations, cosmic shear and galaxy clustering. In addition, combining galaxy-galaxy lensing with galaxy clustering breaks the degeneracy between the galaxy bias and $\sigma_8$. The redshift distributions for the lens and source galaxy samples can be

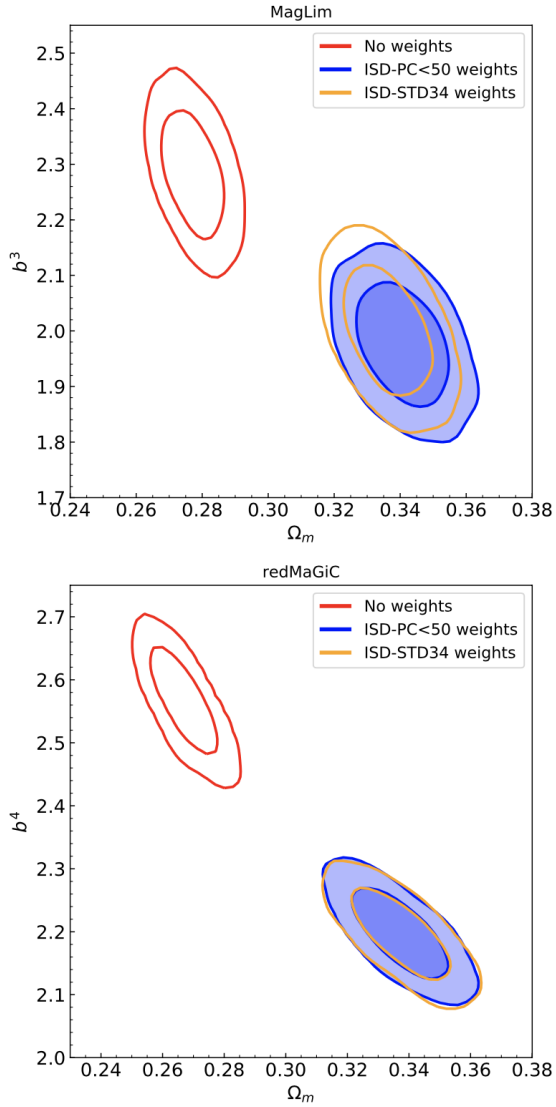


Figure 2.5: Constraints on the galaxy bias parameter and the matter density from galaxy clustering is shown. Weights need to be applied to the galaxies to undo the observed galaxy density's dependence on survey properties. The red contours show the constraints without weights and the blue and yellow show it with weights applied to undo this effect. While this plot is making no statement about the truthful relationship between b and $\Omega_m$ it is clearly showing the significance of applying weights to the galaxy samples [Rodrí guez-Monroy et al., 2022].

seen in figure 2.6.

We use the mean tangential shear as our galaxy-galaxy lensing estimator. The tangential component of cosmic shear, $\gamma$ is given in equation 2.4, where $LS$ stands for the lens-source pair, $w$ is a weight factor, and $e_t$ is the tangential component of the ellipticity of the source galaxy in equatorial coordinates. The lens weights are described in the galaxy clustering correlation section, they aim to remove non-cosmic correlations between observed galaxy density and observing conditions. The source galaxy weights are the inverse variance of the ellipticity weighted by the shear response, see [Gatti et al., 2021b] for more details. More details about the galaxy-galaxy lensing methodology in general can be found in [Prat et al., 2022].

$$\gamma_t(\theta) = \frac{\sum_{LS} w_{LS} e_{t,LS}(\theta)}{\sum_{LS} w_{LS}(\theta)} \tag{2.4}$$

## Y3 3x2pt (Key Project) Results

With the three 2-point correlations calculated we need to assemble them into what we call a "data vector". This vector includes measurements across 5 or 6 redshift bins for the lens galaxies in Y3 depending on the sample (RedMaGiC vs MagLim), and 4 source redshift bins. Furthermore, the correlation functions are split into 20 logarithmic angular bins between 2.5 and 250 arc-minutes. This results in 1300 items in the data vector. After scale and other cuts this is reduced to 461 for the Y3KP analysis. A theoretical model prediction is organized into a vector as well, which are computed using specific parameters of a given model. You can then compute the marginalized probability of a data-set having been produced from a theoretical model with a specific set of parameters.

Two cosmological models are considered, $\Lambda$CDM, and $w$CDM. In $\Lambda$CDM, there are three energy densities, $\Omega_{m,b,\nu}$, where $\Omega_\nu$ is varied as a

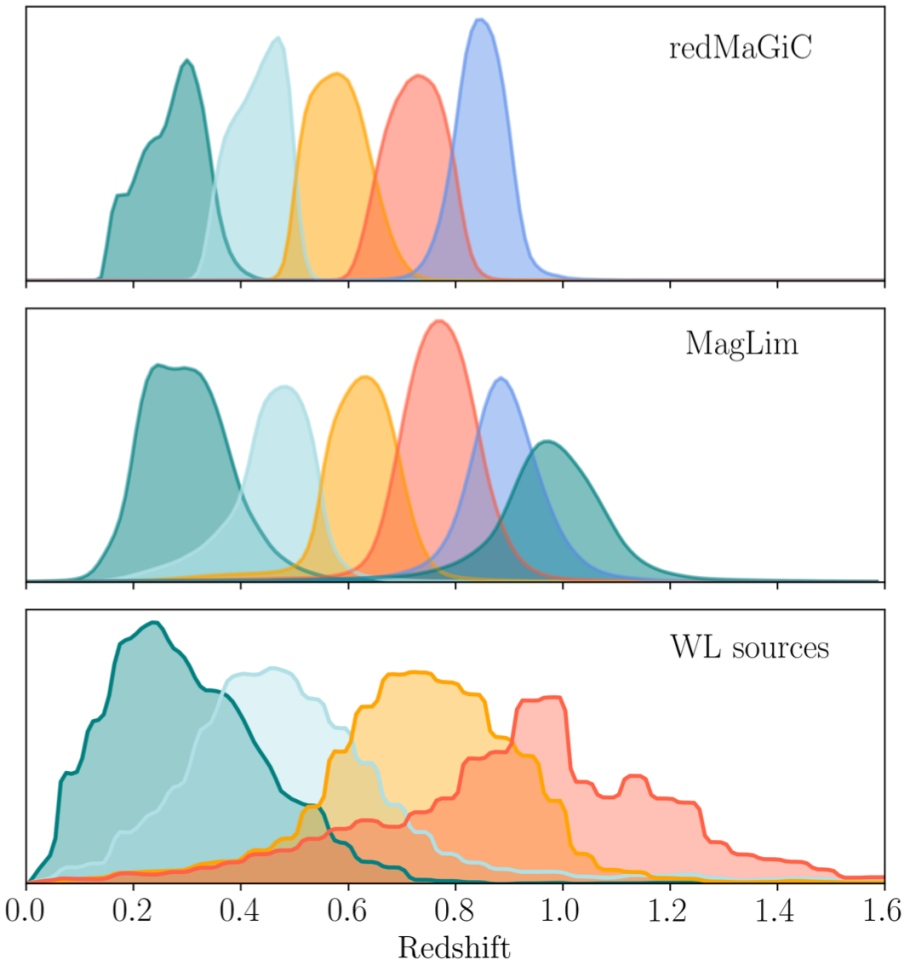


Figure 2.6: Distributions of the two lens galaxy samples, RedMaGiC and MagLim, and the source sample are shown. Note that they all have different numbers of bins. [Prat et al., 2022]

free parameter, along with the Hubble parameter, $h$, the amplitude of primordial scalar density perturbations, $A_s$, and the spectral index of the power spectrum, $n_s$. A flat model is assumed, where $\Omega_\Lambda = 1 - \Omega_m$. In $w$CDM, we allow a free dark energy equation-of-state parameter, $\omega$ that is constant in time. Recall that in $\Lambda$CDM, $w = -1$.

The parameter constraints found in the DES Y3 Key Project for the $\Lambda$CDM model are given below in equation 2.5, and the contours are shown in figure 2.7.

$$S_8 = 0.776^{+0.017}_{-0.017} \quad \Omega_m = 0.339^{+0.032}_{-0.031} \quad \sigma_8 = 0.733^{+0.039}_{-0.049} \tag{2.5}$$

The parameter constraints found in the DES Y3 Key Project for the $w$CDM model are given below in equation 2.6, and the contours are shown in figure 2.8.

$$\Omega_m = 0.352^{+0.035}_{-0.041} \quad w = -0.98^{+0.32}_{-0.20} \tag{2.6}$$

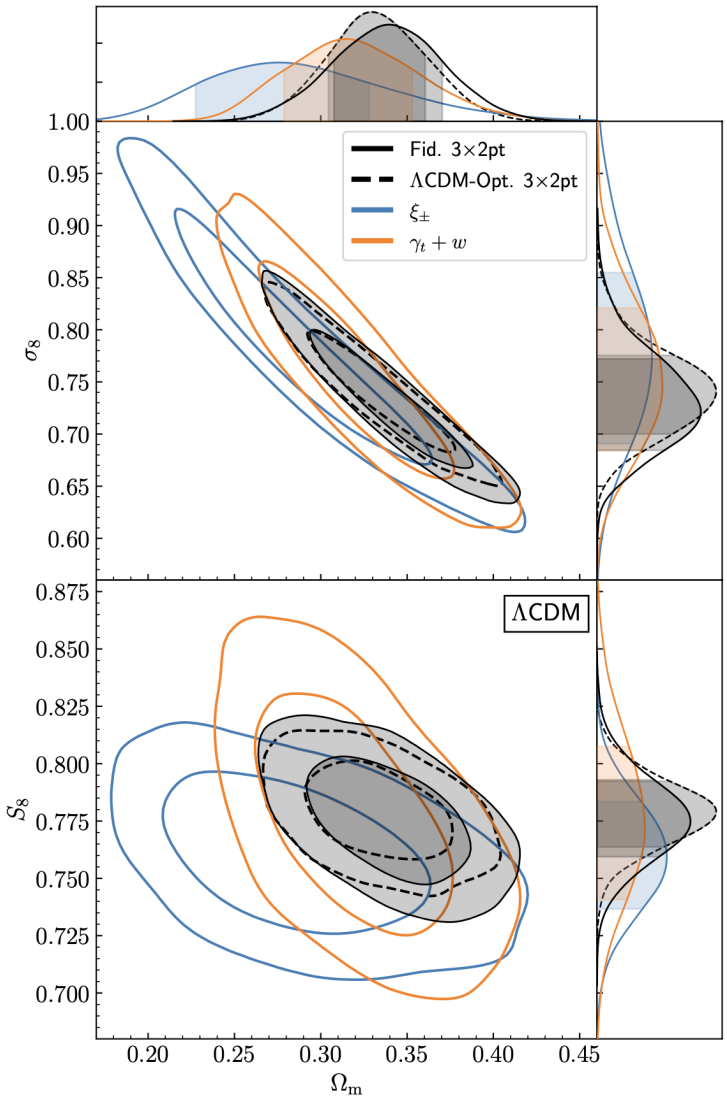


Figure 2.7: Constraints on the three parameters: $\Omega_m$, $\sigma_8$, and $S_8 = \sigma_8\sqrt{(\Omega_m/0.3)}$. The orange contours are from our 2x2pt analysis which combines the galaxy-galaxy lensing and galaxy clustering correlations. The blue contours are from the cosmic shear correlations. The solid black lines are from the combination of both, the 3x2pt analysis. With the dashed lines representing scale cuts applied to the 3x2pt analysis that are optimized for ΛCDM. It's clear that we have a tighter constraining power in the $S_8$ - $\Omega_m$ plane, especially since the 2x2pt and cosmic shear analyses compliment each-other by constraining in different orientations. [Abbott et al., 2022]

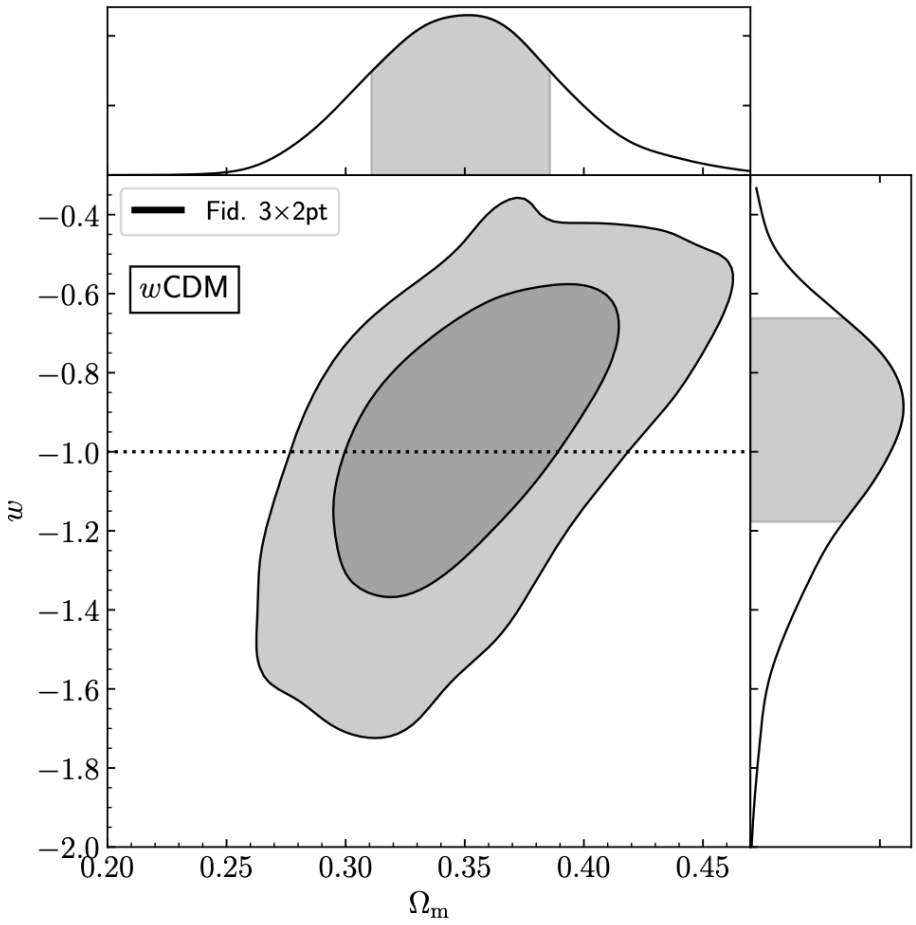


Figure 2.8: In addition to our constraints assuming a ΛCDM universe, we also consider $w$CDM, where we allow $w$ to be free parameter and constrain that. Shown above is our constraint for $w$ which is consistent with -1.0. [Abbott et al., 2022]

# Part II

# Synthetic Source Injection in DES

# 3

# Synthetic Source Injection Introduction

Here I present an introduction to the idea of Synthetic Source Injection both in the context of DES as well as how other fields and surveys are using it.

## 3.1 Introduction

The idea of using synthetic or fake data for testing algorithms is wide spread and ubiquitous across fields. Synthetic sources being added to telescope images dates back to just nine years after the first CCDs were used for telescope observations. The first Charge-Coupled Device (CCD)

was created in 1970. Quickly after, in 1975, the first small digital cameras were made, and by 1976 the first images of astronomical objects using a CCD camera were obtained. Just nine years later, in 1985, we have some of the first reports of using synthetic objects injected into the images for testing and validation.

In, *CCD Photometry of the Sparse Halo Cluster E3* [McClure et al., 1985], two "artificial star tests" were performed which determined the faint limit of the photometry. In the first experiment, 100 stars of random magnitude between 17.5 and 24.5 were inserted into the images. Nearly all of the stars, except those of the faintest magnitude, were recovered showing that the sample was relatively complete. The second set of injected stars was meant to better map the detection limit. Here 150 stars of random magnitudes between 21.5 and 24.5 were injected. The recovered star population showed that the images were complete to a B-magnitude of 23.0, with the completeness falling to just 30% by 23.5-24.0 magnitude. Incidentally, the images used in this 1985 paper were from the prime-focus camera on the 4m telescope at Cerro Tololo Inter-American Observatory (CTIO), where DECam is located now.

In the context of the Dark Energy Survey, we inject model fits of Deep Field objects into our Single-Epoch images. Due to the much higher signal-to-noise in the Deep Field we consider the measurements of their properties to be the truth. After running the injected single-epoch images through the full image processing pipeline we have measured quantities for the injected sources. We can then compare the truth and measured photometry.

The Dark Energy Survey has been using SSI since its Y1 analysis, improving the technique, from Y1 to Y3, and Y3 to Y6. SSI within DES has served as a prototype of the idea, and an example of how critical the methodology can be to cosmological constraints. It has served as a test bed to try out methodologies. We have improved upon the technique

greatly. Specifically in Y6, we focused on becoming more useful for the science analyses. The really fun and exciting aspect of SSI is that you can dream up never ending uses for it. And the main downside is your person power and compute resources to implement them.

In this part of the thesis I will go through the SSI methodology, from creating the truth catalogs, the practical overview of the methodology, the technical aspects, and the initial Y6 results. In this next section, I start by introducing a quick overview of how SSI has changed within DES over the last three iterations. As well as mentioning some of the other collaborations that are prototyping and experimenting with SSI in their analyses.

## 3.2 SSI in DES

SSI within DES (often referred to as Balrog, the name of the code base), has gotten more complex, more refined, and more useful in each of its iterations. A main theme across iterations is that the image processing pipeline is better and better emulated, with the conclusion in Y6 that we have emulated the pipeline that the wide field images go through as close as we can without having run the images at the same point in time, an interesting enhancement that LSST is pursuing. In addition, each iteration has gotten a larger area coverage, from 178 sq deg in Y1 to 1000 sq deg in Y3, and now 5000 sq deg, the full footprint, in Y6. Most of this is due to increased allocations for the SSI effort as we successively proved the utility of the tool.

When I think about Synthetic Source Injection, there are four main categories for how we use it that I categorize applications into. I have listed each below with examples from our current uses of SSI within DES. There are more uses still, almost endless it seems, and those will be discussed further in the outlook section.

**As a Validation or Test of a Process**

- Testing whether the image processing pipeline is working correctly: chapter 6.
- Testing whether the re-weighting of galaxies in order to correct for systematics is working correctly: section 9.1.

**As a Diagnostic and Outlier Finder**

- Using SSI to find populations of objects which are subject to catastrophic fitting failures: section 9.2.

**As a Calibration Technique**

- Using SSI to calibrate the photometry for the galaxy samples by mapping the deep fields to the wide field, providing more photometric information than is in the wide field photometry alone: chapter 7.

**As a Measurement Technique**

- Measuring the completeness curves for DES, and mapping the detection limit: chapter 6.
- Measuring the magnification bias coefficient of the lens galaxy sample: chapter 8.

## DES Y1 - *Forward-Modeling the Transfer Function in DES*

In Y1, there were two methods for determining the transfer function, or cumulative response of the many selection effects and measurement biases of an astronomical survey. The first was a forward modeling technique, and second a measurement technique using synthetic source injection. The forward model technique was a generative modeling method that

produced DES-like data and coadd images, which were then run through SExtractor for detection and catalog creation steps [Chang et al., 2015].

They used the Ultra Fast Image Generator to produce astronomical images which contain user specific instrument features, which generate simulated images and catalogs representative of the DES data. Overall, they simulated 244 sq deg of coadd images and catalogs of the science verification data. They also showed that the simulation outputs captured the major characteristics of the real data. The purpose of this method was to capture the most important aspects in a controlled manner through forward modeling, not to recreate the exact data. As such, there were several simplifications made including: starting from coadd images, assuming that the PSF and airmass are constant across the image, simplistic background models, and that there are no artifacts on the detectors (satellite trails, cosmic rays, etc).

One advantage of this technique is that you can explore counter-factual realizations. However, the disadvantage is that this technique requires models for many features such as: cosmic rays, diffraction spikes, CCD defects, object properties, etc. You may not be able to model all of these, its nearly impossible to make an exhaustive list, and for those that you can model, they may be more simplistic than is real. While a forward modeling method requires characterization and enumeration of effects; in SSI you inherit many of them from either the synthetic sources or the injection images.

### Y1 SSI - *No galaxy left behind: accurate measurements with the faintest objects*

This paper represents the first iteration of SSI in DES to measure the survey transfer function, and the creation of the Balrog code [Suchyta et al., 2016]. It served as a companion paper to the forward modeling technique described above. Typically, in large surveys up to this point, wanting a

high-precision data-set meant throwing away a lot of objects, and keeping only those that were highly complete, which was very wasteful of data. If instead you could characterize the transfer function and completeness, you could keep more of your data, specifically the fainter end of objects. The idea here was to measure the selection function by embedding fake stars and galaxies into real images, and remeasuring them. By doing this the output catalog would comprise a Monte Carlo sampling of the selection function and measurement biases of the survey.

In practice, in Y1 SSI, they drew their samples, not from the deep fields, but from the Hubble Space Telescope's (HST) COSMOS catalog. The object simulations were done using GalSim, like we still do today. But the Y1 SSI detections and measurements were done with SExtractor, like the forward modeling technique. Which is much simpler than our full image processing pipeline for the wide field data. The models were input on coadd images from the science verification data and in total Balrog was run on 178 sq deg of sky, or about 3% of the full survey footprint. There were $\sim$1000 objects per coadd tile injected, compared to $\sim$13,000 in Y3 and Y6. It was computationally expensive, but no where near as expensive as it is in our subsequent generations. One of the main applications for the Y1 SSI data was to use the catalog data as randoms in angular clustering measurements as an easy way to suppress systematic noise which can be larger than the signal itself in certain cases.

### Y3 SSI - *Measuring the Survey Transfer Function with Balrog*

After the proof-of-concept in Y1, there was a lot of excitement to improve the methodology, and run even more of the footprint for Y3. Ultimately, Y3 SSI would be used to directly help calibrate the cosmological measurements from the Wide Field Survey, a first in our field, and a major step forward in exemplifying the utility of the tool and the critical role that it can play in the key projects of constraining cosmological parameters [Everett et al.,

2022].

There were many upgrades that were made in Y3 to the Balrog codebase and the SSI methodology. The differences can be broken into three categories, the input catalog, the image processing pipeline, and the applications. The input catalog used as the source of truth in Y3 was the Deep Fields catalog. By moving away from using an outside catalog, COSMOS, to a catalog created from fields within our own footprint, using our same telescope, camera and image processing pipelines, we were able to create an input catalog very representative of the wide field data, which will turn out to be critical for the applications. Secondly, we injected into the single-epoch images instead of the coadds in order to more exactly recreate the image processing pipeline that the wide field data goes through. We also wanted to more accurately model the whole image processing pipeline, including using single-object fitting codes and creating MEDS files, instead of only using SExtractor for the detection and catalog creation (this will be discussed in more detail in the Y6 methodology chapter: 5). In Y3 we were able to cover about 20% of the footprint, given our computing allocations and timeline. In the end, we found that the number density fluctuations of our SSI sample varied with survey properties within 1% of a typical Y3GOLD cosmology sample. Meaning that our SSI realizations represented the distribution of objects in the GOLD sample very well.

There was an extensive list of applications of the SSI realizations in Y3, the main ones of which were as a tool for photometric redshift calibration and as a measurement of the magnification bias on clustering samples. It was also used for noise detection from undetected sources, to measure photometric response near galaxy clusters, and to find catastrophic fitting failure modes of the image processing pipeline.

## Y6 SSI - *Measuring the Survey Transfer Function with Synthetic Source Injection*

On the heels of the amazing success of SSI in DES Y3 and the proof that not only could it be used as a direct calibration methodology for the cosmological measurements from the Wide Field Survey, but that it was advantageous for us to use it as such, we were excited to get Y6 SSI underway, and improve the methodology again. Brian Yanny and myself co-lead the Y6 SSI efforts for DES. Our main focus for Y6 has been to be the most useful to the collaboration and the key project. There are a few interesting technique changes that we tried along the way, which will all be discussed further in the following chapters, but in the end we wanted to focus our efforts on the changes that would increase the utility of the tool to its applications, specifically to the key project and constraining cosmology.

All of these changes will be described in greater detail in the coming chapters, but one of the main changes in Y6 was the push to being able to cover the full foot-print. Due to how computationally expensive SSI is to run, this necessitated running on both the Fermi National Accelerator Lab (FNAL) computing grid as well as at the National Energy Research Scientific Computing (NERSC) center simultaneously. This required extensive code rewrites in order to be able to compute away from our core cluster. The motivation for running the full-print is to cover the full amount of survey property variation and to increase the statistical power. This is particularly relevant to the use of SSI in photometric redshift calibration as well as the measurement of the magnification bias in clustering samples. One of the projects that I specifically spearheaded was to update our injection scheme. In Y3 we randomly sampled the DF catalog for our injections which was great for capturing the real distribution of objects and mapping the faint end, both the completeness and the detection limit. But this

type of injection scheme is very inefficient for samples that are interested in bright galaxies, like what is used for the photometric calibration for instance. Our new idea in Y6 was to let 1/3 of the injections be randomly sampled, and 2/3 be preferentially bright galaxies to boost the usefulness of the galaxy sample SSI realizations. Finally, there were a number of small, but highly non-trivial changes made to the image processing pipeline, so as to recreate the full pipeline that the wide field images go through, something that we came close to in Y3, but was not fully realized.

DES isn't the only survey using SSI, though we have been a leader in the charge, and at the forefront of showcasing the critical utility of the technique. Especially in the use of SSI to calibrate cosmological analyses. Next, we will turn to discussing some of the other places that SSI is used in Astronomy as well as specifically other cosmological surveys.

## 3.3 SSI Related Works

### High Contrast Imaging

Another research area in astrophysics where synthetic source injection comes up is in High Contrast Imaging (HCI). This is a technique that is used to image faint objects near bright sources. This can include circumstellar disks, and exoplanets around host stars, for example. There are two common observing methods for HCI, Angular Differential Imaging (ADI) and Spectral Difference Imaging (SDI), for both of which researchers use SSI as an algorithmic test and validation technique.

In *Inverse-problem versus principal component analysis methods for angular differential imaging of circumstellar disks, The mustard algorithm*, the authors introduce a new algorithm, mustard, which uses priors on disk morphology to combat the issue of rotationally invariant signals from circumstellar disks. They use synthetic sources in order to test their method's recovery

of the true morphology against the more traditional methods which don't use these priors [Juillard et al., 2023].

In, *PACOME: Optimal multi-epoch combination of direct imaging observations for joint exoplanet detection and orbit estimation*, they propose a method of coadding single-epoch (SE) images together in order to increase the signal-to-noise measurements of exoplanets around bright stars. Through this coaddition process, exoplanets are actually able to cross the detection threshold when looking from single-epoch to coadd images. They test their coaddition algorithm, PACOME, using synthetic sources injected into the single-epoch images. They were able to show that they could detect sources in the coadd images, that are undetectable in the single images by most other SE image processing algorithms [Dallant et al., 2023].

As a final example, *Post-Processing CHARIS Integral Field Spectrograph Data with pyKLIP*, is a post-processing pipeline which reduces HCI data for the CHARIS integral field spectrograph used with the SCExAO project on the Subaru Telescope. The goal is to obtain spectra for known planets and brown dwarfs, as well as produce new discoveries. The new pipeline's performance is demonstrated and evaluated on injected spectra [Chen et al., 2023].

## Hyper Suprime-Cam's *SynPipe*

There are two well known synthetic source injection techniques similar to our DES technique, Balrog, within the galaxy survey field. The first is *SynPipe*, used by the Subaru Strategic Program (SSP) which utilizes the Hyper Suprime-Cam (HSC) on the 8.2m Subaru Telescope [Huang et al., 2017]. The SSP is a combination of three surveys, a wide, deep, and ultra deep covering $\sim$1400, $\sim$27, and $\sim$3.5 sq deg respectively. The wide field data in the i-band reaches a limiting magnitude of $\sim$26.4 for point sources, with 10 or 20min exposures in g, and r, or i, z, and y bands respectively.

Similar to DES and many other surveys, they employ a method of coadding many single "visits" into coadd images with a higher depth.

The image processing pipeline, *hscPipe*, builds on a prototype constructed for the Legacy Survey of Space and Time (LSST). The team has developed a flexible framework in Python to inject synthetic galaxies into real HSC images, similar to our efforts. Synthetic galaxy models are created using *GalSim* [Rowe et al., 2015], and the point-like models are created using HSC PSF models. The synthetic sources are injected into single visit images. Users are free to supply their own catalog of sources for injections. You are able to inject custom synthetic objects, or select either real images or models from an HSC catalog of real galaxies in the COSMOS field. The applications that they use SSI for include, the characterization of the level of blending, completeness checks for various object types (including high-z LBG and Lyman-$\alpha$ emitters), and testing magnification effects around clusters.

## Dark Energy Spectroscopic Instrument's *Obiwan*

The second well known SSI technique in galaxy surveys, similar to SSI in DES, is *Obiwan* [Kong et al., 2020], used by the Legacy Survey. The DECam Legacy Survey (DECaLS) is a part of the Dark Energy Spectroscopic Instrument (DESI) Legacy Imaging Surveys, and is a 9000 sq deg grz imaging survey, that in addition to taking new data uses existing data from several surveys including DES. DECaLS overlaps the Sloan Digital Sky Survey's (SDSS) footprint. Ultimately, DESI is going to select spectroscopic targets using the Legacy Surveys data, which this first application of *Obiwan* is testing. They apply *Obiwan* to a small portion of the SDSS Extended Baryon Oscillation Spectroscopic Survey (eBOSS) Emission Line Galaxy (ELG) sample. eBOSS selected it's targets for spectroscopic follow up from ELGs in DECam images. Thus by injecting realistic ELGs into these same images and measuring which pass the selection criteria, you can better

characterize your selected follow-up sample, and understand the effects of the selections.

Obiwan was applied to a small portion of the SDSS eBOSS ELG galaxies. Sources were injected into individual DECam exposures, run through the image processing pipeline, and then SExtractor was used to build an LSS catalog for analysis. Specifically, they measured which injected galaxies pass the eBOSS ELG sample colour/magnitude cuts. In the end, they determined the grz magnitude distributions for recovered objects, identified contaminants into the selected sample, as well as identified lost galaxies that didn't make it through the selection criteria.

# 4

# The Truth Catalog: The DES Deep Fields

For the synthetic source injection process, we need a catalog of sources and their truth properties. Here I go through what our truth catalog contains, how we make it, and why we consider it "Truth".

## 4.1 The Truth (the partial truth, and nothing but mostly the truth)

One of the essential pieces of Synthetic Source Injection is the source catalog. In our methodology we refer to our source catalog as a truth catalog. This

comes for the fact that one of the main products we output is a catalog containing both the true and measured parameters of injected objects. This comparison of measurements to the truth properties is essential for many of the applications of SSI in DES. Thus, it's imperative that we have a valid truth catalog that is representative of the DES data. Specifically, we use the observations of the DES Deep Fields as our truth. Due to the much higher signal-to-noise in the DF than the wide field, the idea of "truth" here is valid within our error budget. The DFs are also very representative of our data, as most of them are taken from within our footprint. This chapter will discuss the Deep Fields in more detail, specifically in the context of using them as truth information. It will also detail how we create the source catalogs for injection. These source catalogs are the input to the SSI methodology discussed in the next chapter.

## 4.2 The Deep Fields

*Note: There is an updated and expanded set of deep fields for Y6, however, due to the timing of projects on the critical path, it was decided to use the Y3 Deep Fields input catalogs again for the Y6 SSI efforts. Specifically, the Y3 DFs were sufficiently deep enough as compared to the Y6 Wide Field. The determination of this is discussed more in chapter 6. Thus this section and following references to the Deep Fields will be in the context of the Y3 Deep Fields.*

The DES Deep Fields (DF) comprise 11 special areas in the sky both inside and outside the footprint for which we have very deep images and many band photometry. Of these 11 fields, four were used in the DES Y3 Deep Fields cosmology catalogue (referred to as Y3 DFs, or just DF). This catalogue contains eight bands: u, g, i, z, Y, J, H, and $K_s$. There is a total area of 5.88 square degrees with 1.6 million sources, after masking.

Within this DF catalogue of 1.6M objects, there is a trade off that can

Figure 4.1: An small portion of the Deep Field coadd image types can be seen including a 2x zoom insert. The types are from left to right: SE_TRUTH, COADD_TRUTH, and DEEPEST. Note that the SSI inputs are taken from the middle of these images, COADD_TRUTH [Hartley et al., 2021].

be made in the sub-selection of images from which to build a coadd. One can either chose a higher depth with lower resolution, or a lower depth with higher resolution. Stated another way, you either want to constrain the noise level (depth) to a minimum acceptable value and get the highest resolution possible given that. Or, you need a minimum resolution (FWHM) and want to get the lowest possible noise given this requirement. Because of this trade-off and the widely varied science cases that all use the Deep Fields data, three different sets of images were produced in Y3. First, the *DEEPEST* coadd maximizes detectability of faint sources, about 3,000x deeper than a single wide field exposure. Second, *SE_TRUTH* was intended to be used for injection in single-epoch (SE) wide field (WF) images with very good seeing, with this catalog's FWHM being better then 90% of all WF SE images. Finally, *COADD_TRUTH* was created for our Synthetic Source Injection pipeline specifically and we targeted about 10X the WF coadd depth for this catalogue. An example of these three coadd types can be see in figure 4.1.

## 4.3 Truth (DF) Injection Catalogues

The Deep Field images are processed through the Single Epoch image processing pipeline almost identically to the wide field images with only a few changes such as in the selection of which exposures to combine into coadds. More details about image processing pipeline can be found in chapter 5. After processing we have a DF catalog with measured properties. These measured properties are what we consider our truth properties for our synthetic source injection, which is valid due to the much higher signal-to-noise for the DF objects than the WF objects. Specifically, a depth of 10x the WF coadd depth is targeted, with a high priority placed on the seeing, such that the DF FWHM needs to be no worse than the median SE wide field FWHM.

There are some quality cuts that we apply to the DF catalog before we have our injection sample, those are given below. The first two cut out objects with fitting failures and in masked regions. The third ensures that our deep field objects have external near-infrared (NIR) flux measurements, a necessity for the photometric calibration application. The fourth requirement is on the size of the objects, this is based on the grid size that we inject objects into, and is so that we don't have SSI-SSI blending between injections (an interesting future work, but not something that we are looking for here). The fifth cut is to exclude negative flux values, a change we made in Y6 SSI. Finally, we have a cut on magnitude. This limit represents an object having a 1% chance at detection in the wide field, and is discussed more in chapter 6.

$$
\begin{gathered}
\text{flags} = 0 \\
\text{AND mask flags} = 0 \\
\text{AND in VHS footprint} \\
\text{AND BDF\_T} < 100 \\
\text{AND BDF\_FLUX} > 0
\end{gathered}
$$

AND BDF_MAG $< 25.4$

With these cuts applied, we have our catalog of sources, and their truth properties. There is one more alteration to this catalog that will be made. It will be discussed more in chapter 6, there will be weight columns added. For every object in this catalog a probability to be injected will be added based on the photometric properties of the objects. This weight is how the new injection scheme is implemented.

## 4.4 Estimating the Y6 Depth Limit of Balrog Injections

An interestingly circular problem that we have with SSI is that we want to balance the efficiency of injections with going sufficiently deep so as to be able to map out the faint end of the detection limit curves for the survey. If we just randomly injected deep field objects of any magnitude, we would have a very low detection efficiency, $N_{\text{detected}}/N_{\text{injected}}$, as there are more and more objects as you go fainter, and subsequently deeper into the sky, so we constructed a cutoff. We would inject DF objects up to the magnitude where the object had a 1% chance of being detected in the wide field. The magnitude that we use for this is an riz average. How can we know this without doing the injections though? We do a small sample, 100 tiles in Y6, with objects that go past where we believe the limit to be, and calculate the cutoff point.

After running 100 test tiles through SSI, I created an injection catalog which lists what objects were injected where and their true DF properties. I then matched this catalog to the Wide Field detection catalogs to create a matched catalog. This matching was done with a 1.5 arc-second match radius. A few simple cuts were applied to this matched catalog to exclude

masked regions, and fitting failures, which reflect similar cuts for a GOLD sample. These cuts are given below.

$$\begin{gathered}\text{FLAGS\_FOREGROUND} = 0 \\ \text{AND FLAGS\_BADREGIONS} < 2 \\ \text{AND FLAGS\_FOOTPRINT} = 1 \\ \text{AND FLAGS\_GOLD\_SOF\_ONLY} < 2 \\ \text{AND EXTENDED\_CLASS\_SOF} >= 0 \\ \text{AND MATCH\_FLAG 1.5 ASEC} < 2\end{gathered}$$

The detection fraction is plotted as a function of the injected object input magnitude in figure 4.2. With three variations shown, no cuts on the catalog, all cuts, and all cuts minus the extended class SOF. What's clear is that with more cuts the detection fraction is lowered as would be expected. Further, the curves look as expected and transition smoothly toward zero in the 25-26 magnitude region. A zoom in on the 1% detection region is shown in figure 4.3. Here, we can actually see that for the curves without cuts they never cross a 1% combined threshold. Both this effect as well as why the g-band is higher is discussed at length in the completeness curve Y6 SSI results chapter: 6. In short the object detection is done on an riz coadd image, such that if an object is bright in one band, but not the other two, it can still be detected. This causes an asymptote and turn up at the faint end of these curves. If we turn to the last two plots, it can be seen that the 1% combined riz detection limit for Y6 is $\sim$25.5 magnitude. Ultimately, for Y6 SSI, we chose to use 25.4 as the cut off limit, as we already created and used this catalog for Y3 SSI, and it was highly validated and vetted. We don't believe the difference in the .1 magnitude will have any impact, as the 1% limit was a simplistic choice itself.

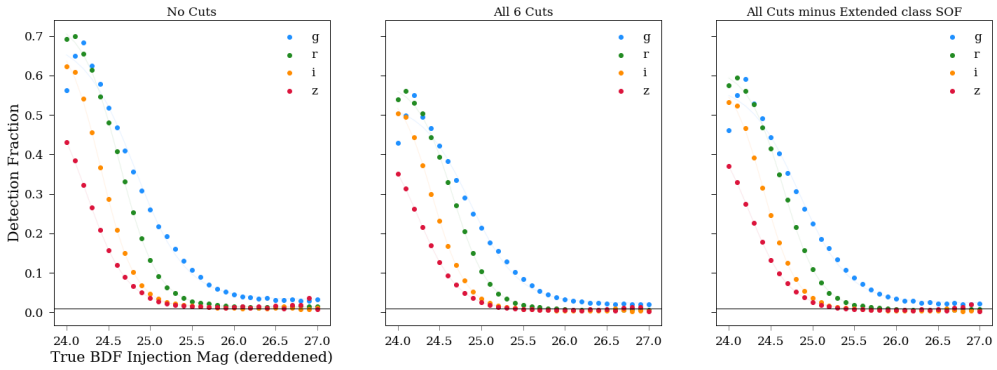


Figure 4.2: Plotted above are completeness curves for Y3 Deep Field objects injected as model fits into 100 Y6 test tiles to determine the 1% cutoff that we want to use for the fiducial Y6 SSI runs. The three subplots represent making either: no cuts, the standard six cuts, or those standard 6 excluding the extended SOF class cut (a star-galaxy cut). While it is clear that the presence of cuts pushes the asymptotic behavior at higher magnitudes, the difference between all 6 cuts or the subset of 5 doesn't appear to be significant.

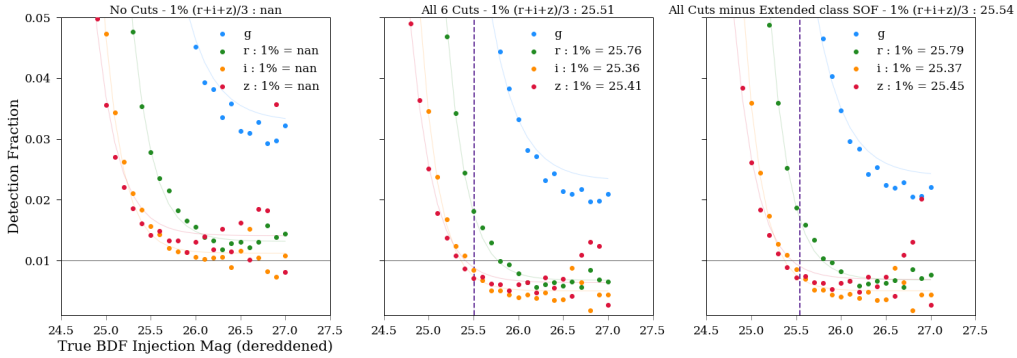


Figure 4.3: A zoom in of the above plot including the addition of interpolation curves for the completeness as a function of true DF object magnitude. The goal is to find the riz average magnitude where there is a 1% detection chance. This will determine our injection limit for the DF input catalog to the Y6 SSI runs. With cuts, this turns out to be $\sim$25.5 riz average magnitude.

## 4.5 Y6 SSI Upgrades

### Cutting Negative Flux Objects

In Y3 a looser cut was preformed in regards to negative flux objects in the deep fields. The cut that was applied was: BDF_FLUX / BDF_FLUX_ERROR $> -3$. This removed objects that had large negative fluxes, but left in objects with small ones. We didn't find any utility in having these negative flux objects in the sample in Y3, and so decided to cut them all together in Y6. Although they represent a small fraction of objects, it still helps the over all efficiency of injections to remove them if they aren't needed.

#### Postage Stamp Injections

One of the suggested improvements to the SSI method from Y3 that we thought of was to inject the actual postage stamps of the objects instead of the model fits. Our motivation behind this, was that the actual images of the objects contain all of the morphological variance you might expect to see, at least to the extant that the DF represents the WF. Whereas the model fits are simplistic fitting routines, reducing the complex morphology down to a few parameters.

I put in a lot of work along with Brian Yanny, reworking the code-base in order to be able to inject postage stamps (images) of objects into the single-epoch images through the SSI process. The results of this and the comparison between the model fits and the postage stamps can be seen in figure 4.4. The model fit objects on the right hand side correspond one-for-one to the postage stamps on the left hand side. That is to say that for each postage stamp on the left side, for which you can see 12, the object in the center of that postage stamp, is the object that we are trying to inject, and the model fit of that exact object can be seen on the right hand side in the same location on the sky. This is very clear with

the bottom row, second object from the left in both sets. If you turn your attention to the bottom row, third from the left, however, you will see the issue with this methodology. The center object, for which the stamp was created, is near other objects, which also show up in the stamp, since it is a cutout of a real image. But how do we account for these other objects in our injections? This became one of the main obstacles in the practical implementation of injecting real images. You need to create "neighborhood" information where you are tracking what other objects you are injecting along with the center object as those might be picked up in the detection step. Furthermore, there are certainly stamps which contain objects we didn't detect the first time, but might now given the new environment that the stamp is injected into which wouldn't be tallied on this neighbors list. And a myriad of other problems arise.

Another consideration here is how the seeing of the stamp convolves with the local single-epoch image. If the stamp has about the same or better resolution and background, it seems like this should be fine. What about stamps which are of worse quality than the SE image you are laying into. How do we determine this? Are we doing this on the fly? That would be an immense rewrite of how the code-base works currently. Perhaps we limit all of our injections to only the highest quality, but then we need to check the bias that that might introduce. We leave this as an outstanding problem, and an interesting science question to research. How to properly convolve the two images when they have different PSFs, seeing, backgrounds, etc. In this context you also need to think about one of the really useful aspects of our SSI methodology, which is that the injections inherit the local survey properties.

At the end of the day, we showed that you can inject stamps, which we did successfully. But ultimately, we decided that this was a very interesting research project that we would save for later. We wanted to focus on making Y6 SSI the most useful for our key project, and while

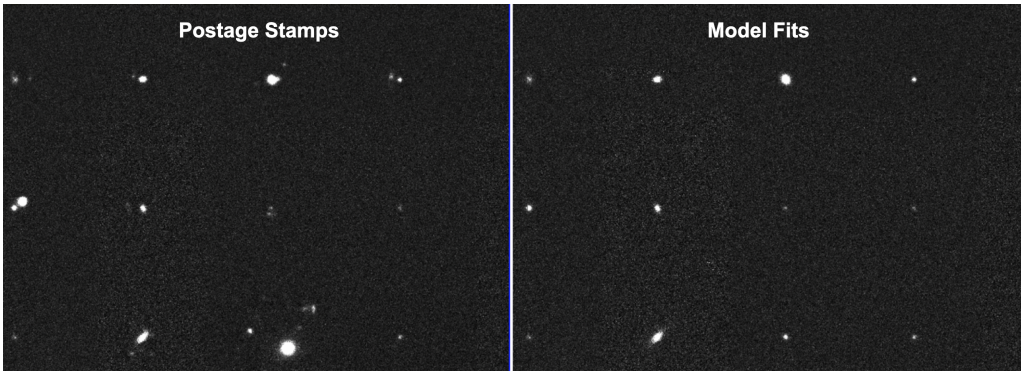


Figure 4.4: Here are two sets of injections onto a blank sky background. The left side shows postage stamp injections which are small image cutouts centered on one detected object. They often contain other objects that are nearby the detected object as seen in the bottom row third from the left. On the right are the model fits for the exact same detected objects on the left. Clearly, with the model fits, we only inject the specific object and as such do not inject extraneous objects as is the case on the left.

this was a very interesting trail to go down, the amount of time that this upgrade would've taken combined with the fact that we have no way of knowing its true impact on the calibration of the cosmological samples until it's implemented fully and tested, meant that we decided to put it into the future work category and focus on the upgrades that we knew would have a large impact for the science.

## 4.6 Delta Star Injections

There is one more catalog that we create as a source injection catalog and that is a *delta stars* catalog. Which is simply a list of star fluxes, which are convolved with a Point Spread Function (PSF) and injected at a given position on the sky. Thus the idealization of a PSF-de-convolved stellar image as a delta-function is realized. In Y3 10% of the injections were these simulated stars. The motivation for including this sample was

to test the baseline performance of the image processing pipeline for a really simplistic morphological case. As such, we were able to test the photometric performance of a pure star sample. We have star-galaxy classifiers for the DF objects, but you will almost certainly have some amount of galaxy contamination, especially at fainter magnitudes. The stars are pure delta functions convolved with the local PSF on the SE images. The color and magnitudes are representative of the the local stellar population in a per tile region.

While this was an interesting test of the image processing pipeline in Y3, there were only a couple use cases for this data-set. Namely, looking at the completion curves. Due to the fact that this sample did not turn out to be as relevant to the science projects, we decided to lower the fraction of delta stars run in Y6. Instead of all the tiles being a mixed grid of 90% DF injections and 10% delta stars, we are running the full footprint as 100% DF object injections. We are then going to select a small amount of tiles randomly, and run those as 100% delta star injections. We also think that this will work better with the timeline of the key project. The DF object samples can be given to the downstream science tasks as quickly as possible with the highest injection fraction possible. We can then focus on re-running some tiles with the delta stars which are less critical time-wise.

# Y6 Synthetic Source Injection Methodology

Here I will describe how we implement Synthetic Source Injection in The Dark Energy Survey. The process is done using our SSI code: Balrog. In addition to explaining the specific implementation of SSI, I will also highlight the SSI and Balrog upgrades that we completed in Y6.

## 5.1 Overview

One of the critical tasks in the Dark Energy Survey's (DES) Year 6 (Y6) key project is to use Synthetic Source Injection (SSI) as a calibration and

diagnostic framework both to aid in the calculation and validation of our quintessential 3x2pt analysis and consequentially our measurement of cosmological parameter constraints. Our framework consists of using a catalog of objects with very well known properties, which we refer to as truth, and injecting them into the individual single-epoch survey images. We then run those images through the same image processing pipeline that the non-injected wide field images go through. By making a catalog of the measured quantities of the injected objects, we can then compare those to the truth quantities. We then use these catalogs of true and measured properties to characterize and measure the transfer function of the survey. The details of this framework in the context of our Y6 project will be discussed further in the following sections.

While the following sections will give a very detailed methodology of our SSI technique, there are a lot of details of the actual technical implementation which will be deferred.

## 5.2 Synthetic Input (Truth) Catalog

*Note: A more full explanation of the source catalog and it's creation is given in chapter 4. But here I will outline the big picture.*

Our Synthetic Source Injection technique is predicated on having the "true" information for the sources that we inject into our images and then measuring these object's photometry in the wide field. In practice, what we mean by "true" is that they contain highly accurate information with the error being well below the characteristic error level of the downstream measurements that we make. We obtain the sources from the DES Deep Fields (DF), a campaign that surveys a small fraction ($\sim$ 6 sq. deg.) of our wide-field survey area ($\sim$ 5000 sq. deg.), to a much greater depth than we do for the wide field [Hartley et al., 2021]. In particular, for the Y3 DF which is the source of our injections for both the Y3 SSI and Y6 SSI efforts,

the catalog had an i-band magnitude depth of between 25.06 and 25.54, depending on field. In comparison, the Y3 Gold WF data had an i-band depth of 23.34.

In order to make the source injection catalogs, we create a catalog of objects from the Deep Field sources that have some simple quality cuts applied which include: removing objects so large that they would blend with one another on the injection grid and removing objects too faint for our use cases. Once we have this catalog, we obtain the model fits for these objects, which are ultimately what we inject. For a discussion on injecting real images instead of the model fits, see chapter 4. In short, we had great success with the model fits in Y3 and have chosen to continue with them in Y6. Once we have the (injection) source catalog containing the Deep Field objects along with their fitting parameters and truth information, we can move forward in the process. In practice, this is a pre-processing step that we curate first and validate extensively before we do our full SSI runs.

It should also be noted that there are a couple other source catalogs we use as well for ancillary runs. We also have a catalog of *delta star* injections which are simplistic delta function objects convolved with the local PSF. The properties of the delta stars also mimic the local stellar populations on a tile-by-tile basis. While in Y3 SSI we injected the delta stars with the DF objects on a mixed grid in a 10/90 ratio, for Y6 processing we have opted to inject only DF objects on the tiles, and to go back and run a smaller delta stars set with randomly chosen tiles. This is discussed more in chapter 4.

Finally, we have a very important ancillary run that we refer to as the magnification runs. These happen after the regular SSI tiles have been processed. We inject the exact same objects, in the same positions, with the same rotations, but with a 2% magnification applied. The re-measurement of these let us estimate the magnification bias coefficients. Specifically, you can see with these runs more detections which represents objects crossing the detection limit as a result of the magnification alone. The

magnification estimation is discussed more in chapter 8. In practice, we use the exact same injection catalog, but add a configuration argument to GalSim in order to do the magnification of the objects.

## 5.3 Obtaining the Base (null-weight) Images

A note before we start: The SSI process is done on a per-tile basis, meaning that these subsequent sections about the image processing pipeline are in the context of one specific tile. We then run many tiles in parallel through the SSI process.

The first step in our SSI methodology is to obtain the base images that we are injecting onto. We inject onto what we call "null-weight" images (single-epoch images with bad pixels set to have zero weight so they don't contribute to coadds when stacking). A full account of the standard image processing pipeline can be found in [Morganson et al., 2018], with specific Y6 updates enumerated here: [Abbott et al., 2021]. I will give a brief overview here as it pertains to SSI. After taking the images with the camera on-sky the first set of processing done is, "preprocessing" which is non-image specific in nature. This includes pixel and CCD corrections such as cross-talk correction, and bad pixel masking. Instrumental effects are accounted for using various calibration images, including masking saturated pixels, and applying brighter-fatter corrections.

Following this preprocessing within a few hours of being taken, the images go through what is called a "first-cut" pipeline which evaluates the images for a baseline quality and flags those that do not meet this baseline for re-observation on a later night. It is from within this first-cut pipeline that we take the null-weight images that we inject onto. While the images that we use to inject onto come from the middle steps of this first-cut pipeline, we only go back and retrieve these images after the full Y6 image set has been fully processed so that we are only retrieving images

that have passed all the quality checks. In the first-cut pipeline: initial astrometric solutions are created by making a catalog of detections using SExtractor and matching the brightest sources to reference catalogs. These solutions are refined later in the image processing pipeline. Next we mask saturated pixels and their associated "bleed trails" where the electrons have overflowed into neighboring pixels. Finally, the images are sky-subtracted, which is a process of subtracting off a template background from the image, images are then flattened. At this point these images are referred to as the "immasked" images (a name that will become apparent in the next step). And these are the exact images that we download from the archive in our SSI pipeline.

The next step is the process of "null-weighting" an image. This is a step that we replicate in our pipeline in the same manner as was done on the original Y6 images. This step consists of masking the final set of artifacts not yet accounted for on the "immasked" images; such as: cosmic rays, which can show up as dots or streaks, and streaks from satellite trails. This masking is accomplished by setting flagged pixels to "0", hence the name "null-weighting". At this point we have our initial set of images that we are going to add sources to.

## 5.4 Balrog - The Injection Step

The process of actually injecting sources from the input catalog onto the null-weight images uses the "Balrog-GalSim" code, referred to simply as *Balrog*. Here I will explain this process, specific to our Y6 implementation. Changes in the methodology from Y3 to Y6 will be called out specifically.

### Define the Injection Grid

The first step in the Balrog process is to create a hexagonal grid across the tile that you are injecting onto. The spacing of this grid is 20 arc-

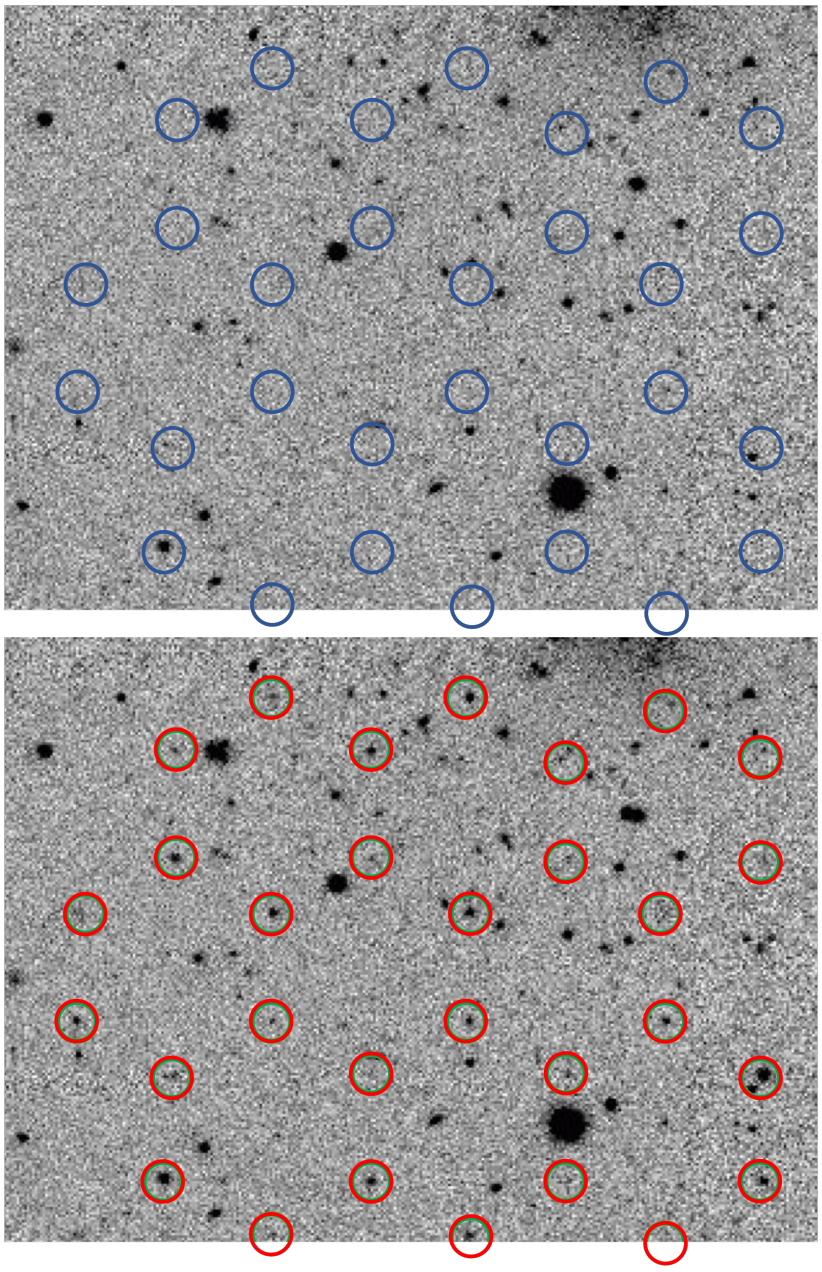

Figure 5.1: A small section of one tile is shown above. The top image is the tile before injection and the bottom image is after. The red circles highlight places an injection has been laid down on, and the blue circles are those same positions but in the original image to make the comparisons easier. The hexagonal lattice that we use to space our injections is apparent here.

seconds; chosen, in part, to balance our ability to inject large objects without blending between injections and inject a high number density of objects. This geometry was also chosen to minimize the correlation signal of injections. Two neighboring tiles in the DES survey, also share an overlap region, which we don't want to inject onto as that would double the injection density tracing the tile structure on the sky. As such, we define the grid only on the "unique" tile area, an area defined such that it only exists on one tile. Furthermore, a small buffer region is added to avoid large injections from bleeding over into the overlap region. This grid is defined by a list of RA, DEC coordinates, which then needs to be converted into individual X, Y pixel coordinate lists for each Single-Epoch chip image that we will inject onto. As such, the data structure that results is a list of single-epoch (SE) images which correspond to a specific chip and band. For each of these SE images, a list of X, Y pixel coordinates which correspond to the RA, DEC grid coordinates for the coadd tile is generated. The hexagonal grid can be seen in figure 5.1.

## Assign Injections to the Grid

Now that we have our lists of injection locations, we need to choose objects and assign them to these locations. In Y3 SSI we randomly selected from the DF catalog for each location. Thus the SSI injections were a fair representation of the true objects that would be found in the wide field up to the cosmic variance limit that the DF have due to their small sample size.

### Y6 Upgrade: New Injection Scheme

One of the big changes that I lead in Y6 was a new Injection scheme. This idea was created by Alex Alarcon and myself, with the big motivation being the photometric redshift calibration application of DES SSI. Very

simply, the photometric calibration technique leverages that fact that the deep field galaxies have very well known redshifts in order to better calibrate the wide field redshifts. This is achievable thanks to SSI, which holds the mapping from the DF to the WF. Thus, we can more tightly constrain WF redshifts by gaining more information about them through the DF. The key to this methodology, is having many wide field realizations (measurements) of the same DF galaxy. Specifically, of DF galaxies which would be used in the redshift calibration, which are bright galaxies.

With the Y3 methodology of sampling the DF catalog randomly, the overall detection efficiency is quite low at 0.37 - 0.60 depending on the depth run of Y3 SSI (two different SSI depth limits were run in Y3). While sampling randomly is important for some use cases of SSI, it's very inefficient for others. So I decided to do 1/3 of the injections (randomly) as the random sampling technique, and 2/3 of the injections would be preferentially bright galaxies which are more useful to the redshift calibration. One of these thirds is a brighter sample than the other third. And for each of these two bright galaxies samples, I require that at least half of the injections have very high quality redshift information. All of these selections get encoded as a "weight" that is given to each DF object based on its magnitude and size. The details of this weight calculation can be found in chapter 6.

So for the assigning of galaxies to injection spots, 1/3 of the grid locations, chosen randomly, are assigned DF galaxies based on the bright galaxy weights, 1/3 are based on the faint galaxy weights, and the remaining spots are sampled from the catalog randomly (each object has the same weight). The results of this choice can be seen visually in figure 6.6.

In practice objects are assigned grid locations by taking the per chip X, Y location lists mentioned above, and adding in the DF object IDs that we just generated from the weights. After this, there are a couple more pieces of information that need to be carried around. The first is a random

rotation that every object receives. The second, is the object's $g-i$ and $i-z$ colors. This is going to be critical when injecting the objects, as our new Y6 PSF modeling code, PIFF, is color dependent. The inclusion of these colors was another Y6 code upgrade that was made. Specifically, I added another mode to run the Balrog code in, so that it can be run with the original PSFEx PSF method, or this new PIFF method; with these being user specified.

**Y6 Upgrade: PIFF PSF Models**

An essential component to the process is that the objects are convolved with the local PSF before being laid down on the images. In Y3 we used PSFEx PSFs, but in Y6 we upgrade to PIFF [Jarvis et al., 2020]. PIFF stands for PSFs In the Full FOV. As light from distant sources passes through the atmosphere, it experiences wavelength dependent distortions, also called chromatic aberrations. This new PSF modelling technique was incorporated into DES processing in order to better account for this effect as well as mitigate another major issue that PSFEx had: discontinuities of the PSF across chip boundaries. PIFF works in sky coordinates instead of image coordinates (unlike PSFEx) which allows it to interpolate the PSF across CCDs simultaneously as well as to account for astrometric distortions better. PIFF is also a color-dependent model, meaning that the solution of the PSF depends on the object's color. The color dependence of the model means that for our injections we need to calculate each object's $g-i$ and $i-z$ colors on the fly (in practice a look-up table is created at the start of a Balrog run). We also need to carry along this color information and feed it forward into the GalSim modeling process.

## Injecting onto the Null-Weight Images

These lists of injections, their locations, and various other information such as the chip name to inject onto, the object's colors, etc, all get formatted as a multi-yaml file that is compatible with the GalSim code. The next step in the Balrog code process is that this GalSim configuration file is read in through the GalSim code and the actual injecting onto images is done. Here GalSim, following the directions in the configuration file, will pull together the null-weight image for the specific chip, the local PSF model, and the model parameters for the objects. After convolving the injection model with the PSF, and injecting the source onto the image, this image is then written out in an identical format as the original images would be found in our archive. This is a tedious detail, but imperative to being able to run the rest of the image processing pipeline on these images in the same manner that the wide field images were run.

The other product that is written out along with the GalSim configuration file is the truth catalog. This is the catalog of all the objects, where they were injected onto, and what their truth properties are. This catalog is set-up such that the same Deep Field object will appear many times as separate injections, and thus each individual object is assigned a unique Balrog ID.

## An Aside: Magnification

For a magnification run, almost everything is the same except for two very important changes. First, instead of letting Balrog choose a random seed to run with, I need to collect the random seed that the original tile was run with, and specify that in the Balrog configuration file. This ensures that all the same objects are laid down in the same locations with the same rotations, etc. Second, I need to specify a 2% magnification in the GalSim configuration file. GalSim handles the actual magnification of the object.

After all of the injection is done, which is computed in parallel to maximize computational resources. We will have a set of null-weight images that contain the injections, a truth catalog of where all the DF objects were laid down and their properties (including the random rotations, and injection probabilities), and our master GalSim configuration file, which contains all the information we need to rerun the tile exactly the same way including the random seed it was run with. This is critical for when we rerun with magnification.

## 5.5 Image Coaddition and Source Detection

Now that we have the null-weight images for a tile we need to proceed through the image processing pipeline. The first step that was run for the wide field images is an astrometric refinement step using SCAMP [Bertin, 2006]. Using SCAMP, a global overall astrometric solution is calculated for all overlapping exposures for the tile using the Gaia DR2 catalog as a reference sample [and T. Prusti et al., 2016, and A. G. A. Brown et al., 2018]. However, we do not rerun SCAMP for our injections, we carry forward the original astrometric solutions from the wide field processing for the tile. The injections should have no influence on the astrometry.

With the astrometric solutions in hand, we can turn to coadding the single-epoch exposures into a tile. We use SWARP to do the coaddition [Bertin et al., 2002]. SWARP takes as input all SE exposures which overlap the tile area, the astrometric solution, and the photometric zero-point for each CCD. Some CCDs are excluded from the coaddition due to known quality issues. SWARP also performs its own background subtraction. SWARP is run in each of the bands, grizY in order to create a band specific coadd image. It is also run once more to create an riz detection image.

A detection catalog is created by running SExtractor on the riz coadd image. Where we exclude g and Y band due to PSF modeling errors that

are too large. For the redshift range that DES is interested in, the exclusion of objects that would show up in just the g or Y band images is not an issue. This source catalog is the list of objects that we consider having been detected. In the wide field (without SSI), this catalog IS the list of objects that we report as our detections for DES. The rows of this table will stay the same, but additional columns will add more photometric measurements of the objects, discussed in the next steps of the pipeline.

## 5.6 Creating MEDS Files for Detections

Using this catalog of sources (which for SSI includes both real objects and our injected objects), we can create the MEDS files [Jarvis et al., 2016]. Multi-Epoch Data Structures, MEDS, is a type of storage format for the pixel level information. For every band's coadd image, there is a corresponding MEDS file. For every object in our source catalog that we obtained from SExtractor (real and injections), we create a series of postage stamps in the MEDS file. The first of these stamps is the band-specific coadd image of that source, and each subsequent stamp are the individual single-epoch images of that source that went into the coadd. Each of these postage stamps contains the image, along with the corresponding weight maps, segmentation maps, and a few other relevant data. These postage stamps, are the single object images that were discussed in the postage stamp section, where we wanted to upgrade the pipeline to inject real images of objects, discussed in chapter 4.

## 5.7 Single-Object Fitting:

### Y6 Upgrade: Fitvd

Now that we have per-band MEDS files and image cutouts for the individual detections, we can move onto the object fitting codes. In Y6 we use the fitting code, Fitvd. The first step is to run a friends-of-friends algorithm to determine the spatial relationship of objects based on the segmentation maps. This algorithm returns a list of object groupings, where the groups of objects will be treated together. These groups are next run through SHREDX, a code that deblends neighbors within a group based on the coadd image. Finally, these deblending solutions, along with the MEDS files are passed to the fitting code, Fitvd.

Fitvd fits a Bulge-Disk-Fixed-scale-ratio, or BDF, profile to the objects. The model that is used contains the parameters: flux, size (T), 2-component shape (g1, g2), and the fracDev, the fraction of light in the bulge (and subsequently 1 - fracDev, the amount of light in an exponential disk). Fitvd fits this profile to the object using all of the SE images simultaneously. It should be noted that the Fitvd code still uses the simpler PSF model, PSFEx, as that gave more robust photometric measurements when combined with Fitvd, over the use of PIFF+Fitvd.

The use of Fitvd as the single-object fitting code is an upgrade from how the Y3 SSI was processed. This upgrade was a critical one, as the Deep Field objects were measured with BDF profiles. However, in the Y3 SSI we used a different fitting model for the SSI realizations called CModel fits. This discrepancy meant that we were always comparing BDF parameters to CModel parameters (magnitudes, sizes, etc). There was always a question about whether a bias that we were seeing between true and measured parameters was due to this mismatch. Thus it was very important to us to switch to Fitvd for Y6 SSI. This turned out to be a

large computation task, specifically to get Fitvd and its companion codes, FoFs+Shredx to run outside our regular computing environment, and on our second allocation, NERSC. After Fitvd is run, we have our measured catalogs, complete with sof model fitting. These catalogs are called sof catalogs, and contain both the real and injected objects. The separation of this will be discussed in the catalog creation section.

## 5.8 Metadetection

Another really important process that is run on the injected tiles is Metadetection [Sheldon et al., 2020]. Metadetection involves including object detection in the metacalibration process. The metacalibration process which was used in the Y3 SSI pipeline worked by artificially shearing small postage stamps of objects and measuring the response. However, object detection can be shear dependent due to the PSF, and we needed to account for this effect. Metadetection, instead, breaks the tile into larger than individual object stamp (but still smaller than tile size) chunks called pizza-slices (Chicago style). Artificial shears are then added to these chunks, and detection and measurement is run on both the non-sheared and sheared chunks. The number of detections on each version will be slightly different due to shear-dependent object detection. Finally, measurements of the shear response are calculated from the images.

## 5.9 Truth and Matched Catalog Creation

Once we have both the regular and the metadetection measured catalogs we can make the matched catalogs. In order to do this, we read in the truth catalogs which lists all of the sources that we laid down, and match those to the measured catalogs. We match by centering an injected object in a circle of a given radius and looking for matches in the measured catalog

that lie within that circle. With only the closest object being counted as the match. This matching is typically done based on 0.5 arc-second circle. All tile's injected and matched catalogs are vertically stacked and these are the data-products passed to the down-stream processes.

# 6

# Initial Y6 SSI Results

As of writing this thesis we are in the process of running SSI over the full footprint, a time intensive process. Here I will present the initial results from the first 1000 random tiles, or ∼10% of the footprint.

## 6.1 Introduction

As of writing this thesis, we are in the process of running the ∼10,000 tiles of SSI for full footprint coverage for Y6. In addition we are also running 2,000 magnification tiles to supplement. The results presented in this section will be for the first random 1000 tiles that we currently have catalogs for, in other words, a random 10% sample from the final sample. This is also already 50% of what was completed in Y3 for the total SSI run.

## 6.2 New Y6 Weighted Injection Scheme

One of our main goals for the Synthetic Source Injection project in Y6 is to map out the detection limit for the survey. We purposefully inject objects past the detection limit in order to precisely measure what that limit is based on our recovered SSI object population. By running a small set of deep injections on Y6 tiles, I found that the limit at which there was a 1% chance to recover an injected object was $\sim$25.5 riz average magnitude. More details about this process can be found in section 6.4.

Inherently, this science goal is a very inefficient way to use injections. Typically, as you push fainter in magnitude you are simultaneously pushing to galaxies farther away from us, and subsequently there are more and more galaxies at those distances that we observe. The effect that this translates into is that if you look at the distribution of objects in magnitude space for a single image of the sky, it will look much like the injected distribution in the third panel in figure 6.1. There is an exponential increase in number as you push fainter, up to some detection limit of your telescope where the number falls off quickly. In the faintest region, you are recovering $\sim$1% of the objects that you inject, meaning that a huge number of injections are "wasted". Of course, they aren't actually wasted, the shape of this curve was exactly what we want to measure with Y6 SSI.

The issue with injection inefficiency comes from the fact that we have other main goals for Y6 SSI besides mapping the detection limit; namely to help with redshift calibration for galaxy samples. Synthetic source injection is used to provide a mapping between the wide field and deep field. Our process takes deep field galaxies, injects them into the wide field and recovers their wide field properties, providing a map between deep and wide field galaxy properties. Using this key you can exploit the much more accurately known deep field galaxy redshifts in order to put better constraints on the wide field redshift distributions. The aspect

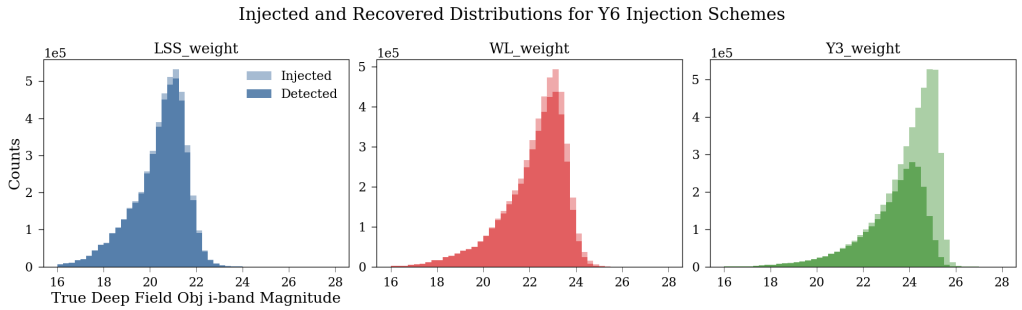


Figure 6.1: Shown here are the histograms of detected (bright bars) and injected (faint bars) objects for the three different injection schemes used in Y6 SSI. The LSS and WL are brighter and fainter, bright galaxy samples, where as the Y3 scheme is random selection from the DF catalogs. It's clear that by using a combination of these three schemes we achieve a higher recovery rate of objects than if we just use the Y3 scheme alone.

of this process that is most important to the injection scheme is that the characterization of the wide field redshifts depends on the number of times the same deep field galaxy is injected and recovered in the wide field. With a statistical reduction in noise for higher numbers of repeat deep field object injections and detections. Thus we would love a high detection efficiency to maximize our impact, which is at odds with the inherent inefficiency of the scheme described above.

In Y3 the injection scheme was to randomly sample from the Deep Fields input catalog. This catalog was made from detections of deep field objects with only simple cuts made. In this way we obtained a mostly statistically fair representation of real objects that could be observed in the wide field survey. As discussed above, this sampling is great for mapping the detection limit of the wide field survey, but naturally ends up injecting exponentially more objects as you go fainter. For Y6, this injection scheme, represented by the third panel in figure 6.1, has an overall detection fraction of $\sim$59%.

However, for the purposes of the photometric redshift calibration, the

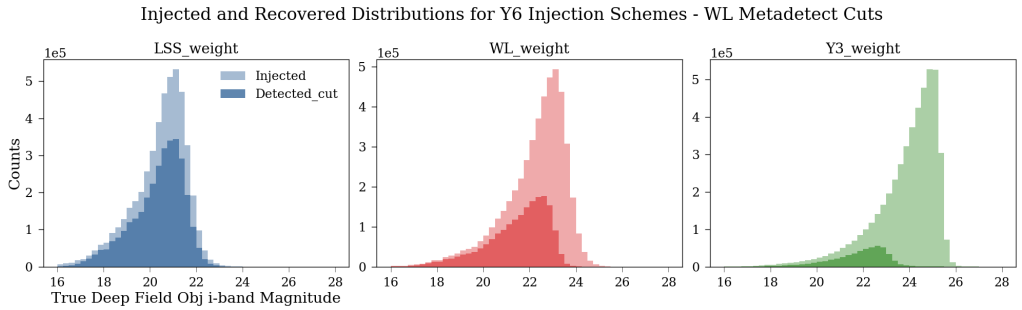


Figure 6.2: This plot is the same as above, showing the relative detection to injection histograms for the three Y6 weighted injection schemes, but now with basic Metadetection cuts applied to the detections. This represents a realistic estimate of which objects would make it into the galaxy samples. By just using the Y3 scheme, we lose a very large fraction of objects, combining that scheme with the LSS and WL though, allows us to recover a higher percentage of objects in the science samples, boosting the statistical power of the injections.

sample has selection cuts applied to the metacalibration photometry in order to achieve a more homogeneous catalog, described in more detail in: [Myles et al., 2021]. Applying these cuts to the above catalog, we can evaluate the effective detection fraction of objects that would make it into the weak lensing source catalog. As seen in the third panel of figure 6.2, only ∼11% of objects injected would make it through detection and Metadetect cuts for a Y3 Scheme. So, for every 10 random objects we inject, only 1 is making it into the redshift calibration catalog. This was the motivation to create a new injection scheme in Y6 SSI.

## Boosting the Number of Bright Galaxies

The new Scheme that we proposed for Y6 included splitting the grid into two different types of injection schemes. One third of the grid would stay the fiducial 'Y3 weight' of randomly injecting objects from the deep field catalog. Since we increased the area that we are injecting from ∼2,000 tiles

to the full ∼10,000 tiles, we are still getting an increase of 5/3 in injections for this purpose. But now the other 2/3 of each tile will be injected using a weighted scheme which preferentially injects brighter galaxies. Resulting in a higher injection efficiency for the redshift calibration sample. The 2/3 of injections were further split into a fainter "WL weight" and brighter, "LSS weight" sample. Each with the same logistic shape, discussed next, but with different turning points in magnitude space.

The new scheme adds weights to all objects in the deep field catalog, such that when randomly chosen for injection, the probability that they get selected is weighted based on their i-band magnitude, "mag_i", and their characteristic size parameter, "bdf_T". There are two different effects that we wanted to achieve. First, we wanted to create a logistic probability as a function of i-band magnitude such that the LSS and WL samples will sample a brighter distribution of objects than the whole DF input catalog contains. This probability function can be seen in figure 6.3 column 2. And is represented by the equation 6.1.

$$P_{gals}(x, m, h, k) = \frac{h}{1 + e^{-k(x-m)}} \tag{6.1}$$

Here, $x$ is the deep field object's BDF i-band magnitude, $m$ is the midpoint of the logistic function, which we set to $21.5$ and $23.5$ for the LSS and WL samples respectively. $k$ is a growth parameter specifying the steepness of transition from 0 to 1, which we set to $4.0$, and $L$ is the supremum set to $1.0$ so that this function returns a probability to select the object for injection.

This probability function alone isn't sufficient for our use case, as it will end up injecting a lot of bright stars which dominate in number over bright galaxies in the magnitude range that we are looking at. So we need another function that will exclude a majority of stars. This can be accomplished by creating another cut based on the characteristic size parameter of objects, bdf_T, which is ∼0 for stars. The probability shape that we want to create

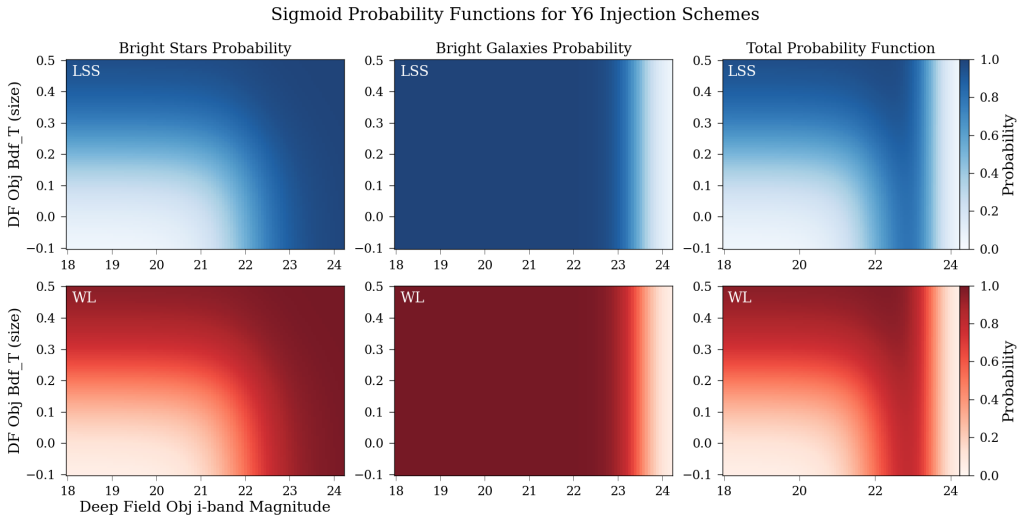


Figure 6.3: The third column shows the probabilities of injection assigned to the DF objects as a function of their measured size and magnitude for both the "LSS" and "WL" Y6 Injection Schemes. Note that the LSS sample is a bit brighter than the WL sample. The first and second columns show the two components that are combined to create the final probability: a de-selection of stars, and a de-selection of faint objects in general. These two combine to create a weight for the random selection of objects that prefers bright galaxies. We make smooth cuts with logistic functions, so as to include other objects as well and avoid a hard cut that might bias our samples.

is like a bowl in size and magnitude space and can be visualized in the first column of figure 6.3, with the corresponding equation given by equation 6.3 which depends on two logistic functions for each dimension given by equation 6.3.

$$f(x, m, h, l, w) = \frac{h - l}{1 + e^{(x-m)/w}} + l \tag{6.2}$$

$$P_{stars} = 1 - f_{bdf_T}(x_T, m_T, h_T, l_T, w_T) * f_{mag_i}(x_m, m_m, h_m, l_m, w_m) \tag{6.3}$$

Similar to equation 6.1, $x_T$ and $x_m$ represent the deep field object's bdf_T size and i-band magnitude. $m_T$ and $m_m$ are the midpoints for each dimension, selected as 0.2 and 22.0 respectively. $h_T$ and $h_m$ still represent the supremum and are selected as 1.0 for each, again to normalize these into probabilities for injection. $l_T$ and $l_m$ adjusts the logistic in the "y" direction, here set to 0.0005 for both. And finally, $w_T$ and $w_m$ represent the growth factor, similar to $k$ but inverse functionality representing width of the transition in this form, set to 0.1 and 0.5 respectively. All of these parameters are the same for both the LSS and WL samples.

$$P^i_{total} = P^i_{gals} * P_{stars} \tag{6.4}$$

The final combined probability for injection of a deep field object into a sample is given by equation 6.4 and can be seen in the third column of figure 6.3. Where the $i$ denotes either the LSS or WL sample. The distribution of these samples from 1000 tiles in magnitude space can be seen in figure 6.2.

The overall distribution of objects in true deep field BDF_T (size) and i-bang magnitude space can be seen in figure 6.4. As all three sub-plots are normalized to the same binning and log-counts scale, you can see that more bright galaxies are being injected in the "LSS weight" then the "WL weight" then the "Y3 weight". This is especially obvious when comparing the area from 0.1 to 0.5 in BDF_T and 16 to 20 in i-band magnitude space.

## Ensuring High Quality Redshift Truth Information

There is one more alteration that occurs in the "WL weight" and "LSS weight" samples, again, in order to increase the utility of the injections for the wide-field photometric calibration of the weak lensing source catalog. As discussed previously in chapter 4, the "deep fields" are comprised of 10 supernova field pointings and the COSMOS field pointing. Four of

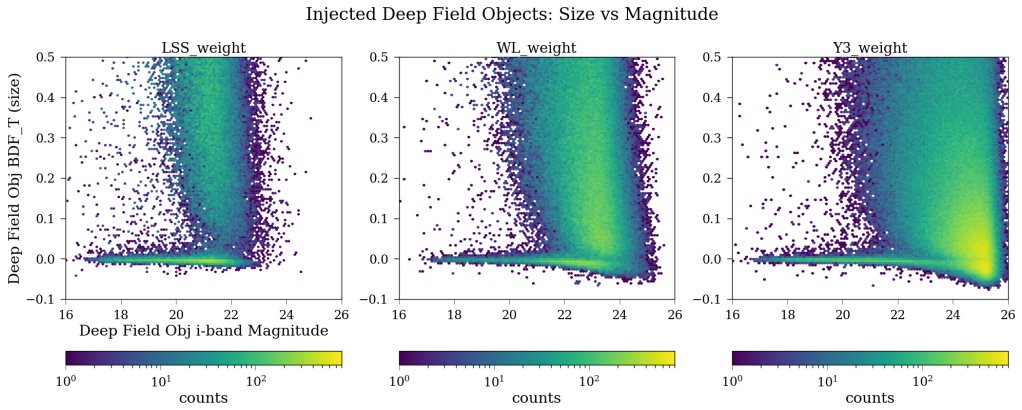


Figure 6.4: Shown here are the relative abundances of DF objects that are injected for the three Y6 injection schemes. The locust of points at bright magnitude and ∼0 size are mostly stars which would be excluded from the galaxy samples. This is the population we want to minimize in the LSS and WL injection schemes. Indeed, you can see that we have done that here. By comparing the LSS sample to the Y3 sample in the upper left hand corners of the plot, you can also see the increase of bright galaxies that we include.

these fields were selected as the "main" Deep Fields catalog in Y3, SN-C3, SN-X3, SN-E2 and COSMOS, balancing area coverage with high quality photometric data availability [Hartley et al., 2021].

The cornerstone of the SOMPZ redshift calibration technique, see chapter 7, is exploiting the mapping from deep to wide field provided by SSI and the high quality photometric redshift information in the deep fields. As such, we wanted to ensure that a high number of Deep Field injections had the necessary "high quality" redshift information, as not all deep field objects do. This definition of "high quality" was determined by the supplementary redshift information each objects has, with any one of the following satisfying the requirement. First, an object may have spectroscopic redshift information gathered from the following surveys: zCOSMOS [Lilly et al., 2009], C3R2 [Masters et al., 2017], VVDS [Le Fèvre,

O. et al., 2013], or VIPERS [Scodeggio, M. et al., 2018]. Second, an object may have 30-band photometric data from the COSMOS survey [Laigle et al., 2016]. Third, the object may have 66-band photometry from the PAUS+COSMOS combined photometric catalog [Alarcon et al., 2021]. The overlap of the four deep fields with the three "high quality" redshift data sets listed above can be seen in figure 6.5 from [Myles et al., 2021], where the green data represents deep field objects with only ugrizJHK redshift photometry. The NIR data in the, J, H, and $K_s$ bands, comes from either the VIDEO (SN-C3 SN-X3 SN-E2) or UltraVISTA (COSMOS) surveys [Jarvis et al., 2012, McCracken, H. J. et al., 2012].

While a fraction of the Deep Field objects will have high quality redshift information, I guaranteed that at least 50% of the injected objects in the "WL weight" and "LSS weight" schemes would have high quality redshift information by adding an indicator function to the probability of injections. For each 1/3 of objects injected in the "WL" and "LSS" samples, half of those injection's probabilities are multiplied by the indicator function given in equation 6.5. Where the indicator is calculated based on the requirement for "High Quality" redshift information listed above.

$$\mathbb{1}_{\text{High Quality z}}(x) \tag{6.5}$$

The resulting distribution of injections for the Y6 SSI Injection Scheme can be seen in figure 6.6.

## Results

Overall, we saw amazing improvement in the efficiency of injections that made it through to detection and past metadetection selection cuts. These results can be seen in figure 6.2. In the "Y3 weight" scheme of randomly selecting objects for injection, which represented 100% of injections in Y3, but only 1/3 of injections in Y6, we get a detection efficiency, $\eta \approx 59\%$.

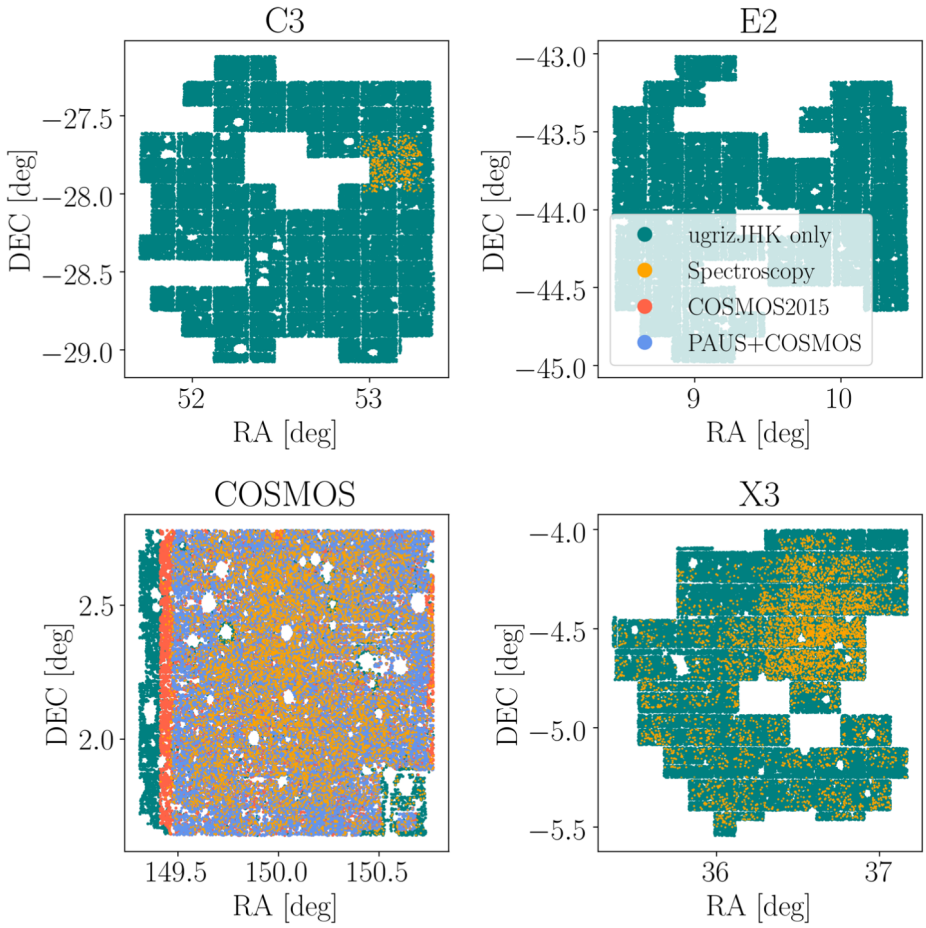


Figure 6.5: Shown here are the four DES Deep Fields that are included in the fiducial Y3 DF catalog. Shown in teal are the points where we have ugrizJHK photometry. Yellow denotes spectroscopic information as well. Red and Blue show where we have COSMOS and PAUS+COSMOS many band photometry. This also showcases why we include the COSMOS field as one of our DF pointings: we can combine outside photometric information into our redshifts calibration. [Myles et al., 2021].

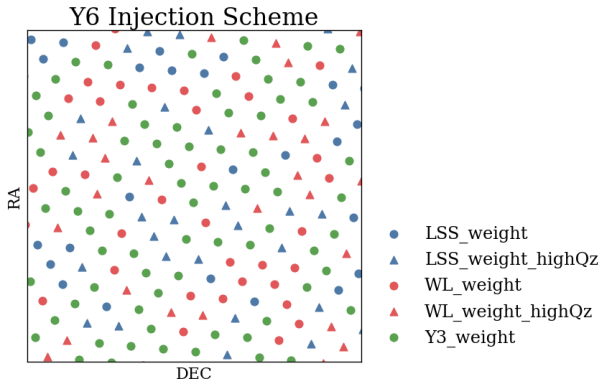


Figure 6.6: A visual of our injection scheme. Each point is a real location of an injection that was laid down in a real image. 1/3 of the points are blue, which are from our brighter bright galaxy injection weight, 1/3 are red from our fainter bright galaxy scheme, and 1/3 are green which were randomly selected DF objects. The blue and red samples are split so that half of them are injections where we have guaranteed high quality redshift information.

After applying the weak lensing source sample metadetection cuts, we only get $\eta \approx 11\%$. For the "WL weight" sample, which represents another 1/3 of the injections, we get an overall efficiency of $\eta \approx 91\%$, and $\eta \approx 39\%$ for the cut sample. Finally, for the "LSS weight" sample our overall efficiency is $\eta \approx 96\%$ and with cuts is reduced to, $\eta \approx 66\%$. These can be seen in columns 3, 2, and 1 of figures 6.1 and 6.2 respectively.

Combining all three samples together we see an overall detection efficiency in Y6 of $\eta \approx 82.0\%$ and with the cuts applied, $\eta \approx 38.6\%$. Comparing this overall efficiency after cuts to the "Y3 weight" efficiency of $\eta \approx 11\%$, shows that per tile we are increasing our number of injections that make it into the weak lensing source sample by a factor of $\sim$4. Combined with the area boost of 5x tiles, we should see an overall number increase of $\sim$20, which is amazing.

Furthermore, looking at figure 6.7 we can compare the number of detected objects that pass the metadetection cuts previously mentioned,

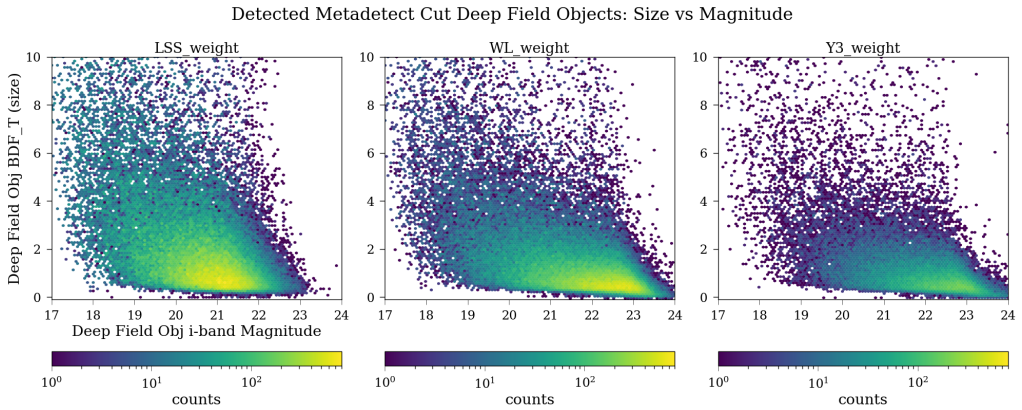


Figure 6.7: Shown here are the SSI detections which pass a Y3 Metadetection cut, one of the most simple cuts that could be applied to create a galaxy sample. The three Y6 injection schemes are shown. LSS and WL clearly have more injections that pass a metadetection cut than the Y3 random injection scheme.

for the three injection schemes. By looking at counts in a size vs magnitude space, it's clear that we have injected many more bright galaxies in the "LSS" and "WL" schemes further proving it's utility.

## 6.3 Repeat Deep Field Injection Frequency

One of the main motivations behind the new injection scheme was to have many many realizations of the same DF galaxy. How well this turned out can be seen in figure 6.8. For each type of injection scheme I am showing the histogram for the number of times the same DF objects gets injected. With the "Y3 weight" scheme most objects are injected between 1 and 10 times per 1000 tiles. However, for the "LSS weight" and "WL weight" scheme, most objects are injected between 1 and 50 times per 1000 tiles. This is the exact effect we wanted to see, more repeat injections such that specific DF objects have more statistical realizations of their mock wide

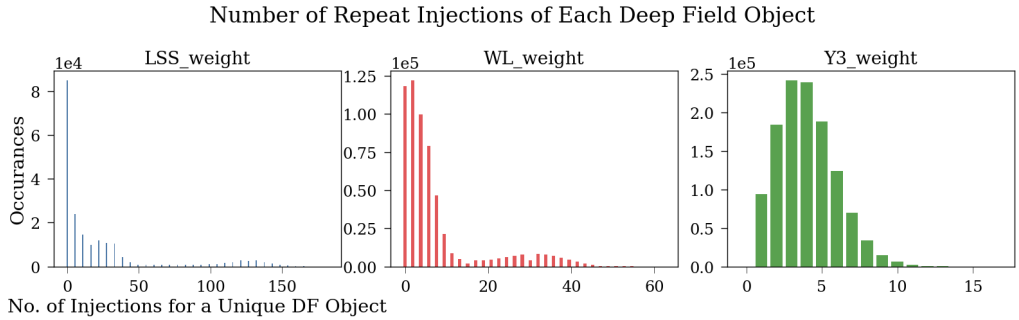


Figure 6.8: These three histograms are showing the occurrences of the number of repeat injections of the same DF object. For example in the Y3 scheme, most DF objects are injected 3 times, and the most times an object is injected is 13. Both the LSS and WL scheme boost the number of times the same DF object is injected. This is due to their, effectively, smaller source catalog sizes due to the extreme down-weighting of bright stars and faint objects. These numbers are all per 1000 tiles.

field photometry in order to better calibrate the wide field redshifts.

Specifically, for the redshift calibration method, we are only interested in objects that can pass a metadetection cut. The distributions of those are shown in figure 6.9. It's a bit more clear to see the improvement through the statistics given in table 6.1. For the Y3 weight scheme, the average DF object that would pass a Metadetection cut would have 3.01 realizations on average per 1000 tiles. With my new injection scheme that number increases to 12.27 per 1000 tiles. So the new injection scheme boosted the number by a factor of 4 alone. Plus we are boosting the area from Y3 to Y6 SSI by a factor of 5. Thus in Y3 for a Metadetection sample, the average number of realizations for a DF object was $\sim$6, and in Y6 SSI it will be $\sim$ 123, a factor of 20 more, and $\sqrt{(20)} \approx 4.5$x in statistical noise reduction. This was the huge motivation in developing the new injection scheme and spending so much time in refactoring the code so that it was able to be run on multiple supercomputers, allowing up to achieve that 5x area coverage.

| Scheme | Avg | Min | Max |
|---|---|---|---|
| Y3 | 3.01 | 1 | 16 |
| LSS | 23.67 | 1 | 180 |
| WL | 7.93 | 1 | 63 |
| Overall | 12.27 | 1 | 218 |

Table 6.1: The average number of SSI realizations of the same DF object that would pass a Metadetection cut for the various injection schemes used in Y6. Including the combined result. These numbers are per 1000 tiles of injections.

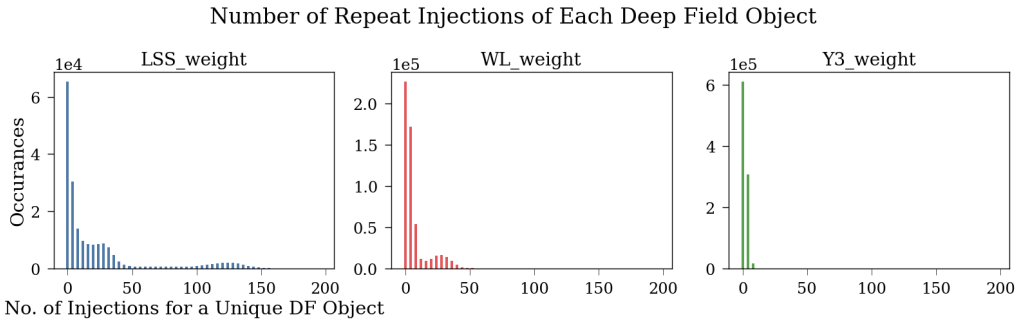


Figure 6.9: This plot is similar to the one above, showing the occurrences of the number of repeat injections of the same DF object. However, now the detections have a metadetection cut applied which is more relevant to the galaxy sample applications. For instance, the photometric redshift calibration is concerned with SSI detections which pass this cut. If we had just used the Y3 weight scheme, each object would only have $\sim$3 realizations/1000 tiles, however the combination of the new schemes boosts that to $\sim$12/1000 tiles.

## 6.4 Y6 Completeness Studies

One of the main products that we can use SSI to measure is the completeness or detection fraction as a function of injected object magnitude. Figure 6.10 shows this for each band, griz, from input object magnitude 16 to 28 as measured in the respective bands. These curves are all based on the "Y3 Weight" sub-sample of all Y6 SSI injections. What can be seen is a smooth transition from an almost complete sample to near zero around where we think the detection limit is.

On the bight end, we are nearly 100% complete until about 19th magnitude. The g-band does sink lower as you go brighter from 19th to 16th magnitude. This is a known effect that was seen in Y3 SSI as well. We believe this may be due to the fact that g is not included in the riz detection image, and so for objects bright in g but dim in other bands, they are not being picked up. I previously argued that we weren't worried about that effect, and we aren't. But what is interesting here is that we don't see a similar dip in the GOLD sample. So, we think that these objects may be over represented in the DF sample as compared to the GOLD sample. This isn't too surprising, the fact that a population of objects could be over represented, as the DF's area is about .1% the WF area, and thus are limited by cosmic variance.

An interesting feature of this plot is that we don't dip to zero on the faint end, and in fact the detection rate starts to increase. This is actually completely expected given how we handle object detection and our injection limit. Recall that the objects that are selected for detection need to have an riz *average* magnitude below 25.4. So naturally, you will have objects that are bright in some bands and not others. Imagine an object with riz magnitudes: [20, 25, 26], the riz average, 23.7, means that this object makes it into our DF catalog and gets injected. When we make the coadd detection image, with an riz combined coadd, it's easy to

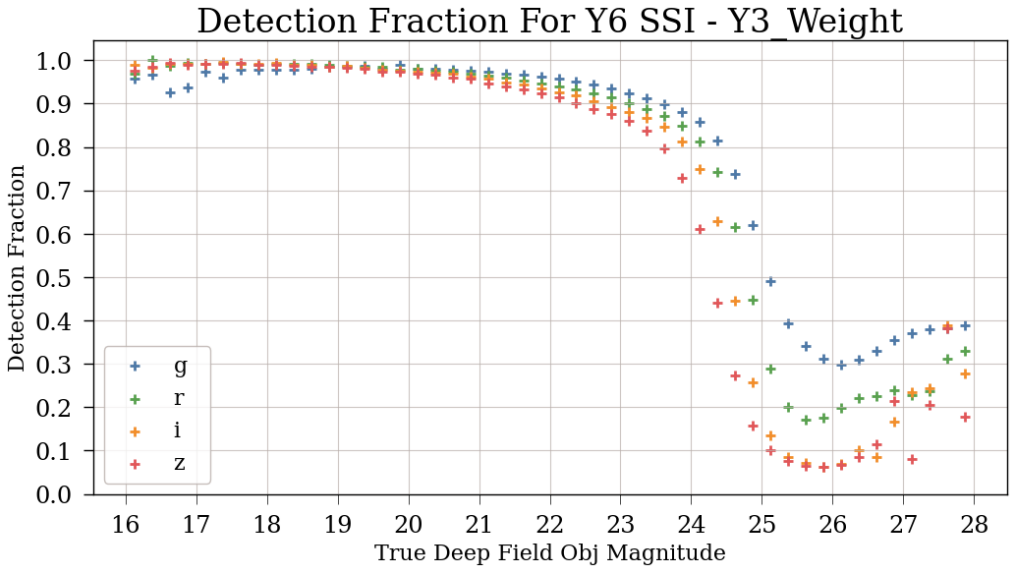


Figure 6.10: These are the Y6 completeness curves as measured with the Y6 SSI runs. These curves are only for the 1/3 of objects that are randomly sampled from the DF for injection, which best represent the true distribution of objects one might observe in the Wide Field. Note that the plateau of detection fraction above zero and the raising tail is not a real detection effect, but a consequence of choices made in our image processing pipeline. Subsequently these objects which are getting detected at very high magnitude are very low signal-to-noise, and would not be normally detected.

imagine that it gets detected. We then make MEDS stamps for this object, which in the i and z bands would probably not be detected, but due to its brightness in r, it is. On these curves in figure 6.10, in the r band, it's in the point near 20mag, but in the i and z bands it's in the tail of the curve. The reason the curves turn back up on the ends, are that they are made from objects that are dim those respective bands, but have been injected and detected due to being bright in other bands. This effect is also what is causing the g-band overall to plateau higher than the other bands.

This fact is actually backed up by looking at the flux ratios of the

| band | 98% | 95% | 90% | 75% | 50% |
|---|---|---|---|---|---|
| g | 19.53 | 22.38 | 23.55 | 24.45 | 24.86 |
| r | 19.94 | 21.72 | 23.06 | 24.16 | 24.53 |
| i | 19.42 | 21.32 | 22.67 | 23.8 | 24.2 |
| z | 19.17 | 21.01 | 22.3 | 23.36 | 23.91 |

Table 6.2: Interpolating the completeness curves from figure 6.12, I estimate the magnitude cut-off per band of various completeness levels.

different bands, as seen in figure 6.11. Here the ratio of g-band flux to r, i, and z are shown on the top. A zoom in on the faint end is shown below. These are all detections, but what is clear is that on the faint end, specifically past 26th magnitude, the ratios drop. Meaning that there is almost no g-band flux compared to the other bands, so why did these objects get detected at all? There was a higher flux in another band. While this is all very interesting to me, and a really cool example of how specific choices in our image processing pipeline create biases down the line, it means that these completeness curves are not very useful on the faint end. They don't tell us what we want to know, which is what is the probability of a 26th magnitude g-band object being detected. Our procedure for handling this is to add a signal-to-noise cut.

Shown in figure 6.12, are the completeness curves with a signal-to-noise cut of 10 applied. As can be seen, the riz curves all tend smoothly to zero, leaving just g-band behind. By interpolating the curves, I estimate the cutoffs for various completeness limits in table 6.2. We have greater than 95% completeness in all bands up to 21.01 magnitude, and we are more than 75% complete in all bands up to 23.36 magnitude.

## 6.5 Photometry Comparisons

Lastly, we will look at the differences in the recovered photometry for the initial Y6 SSI. This can be seen in figure 6.13. The three rows represent the

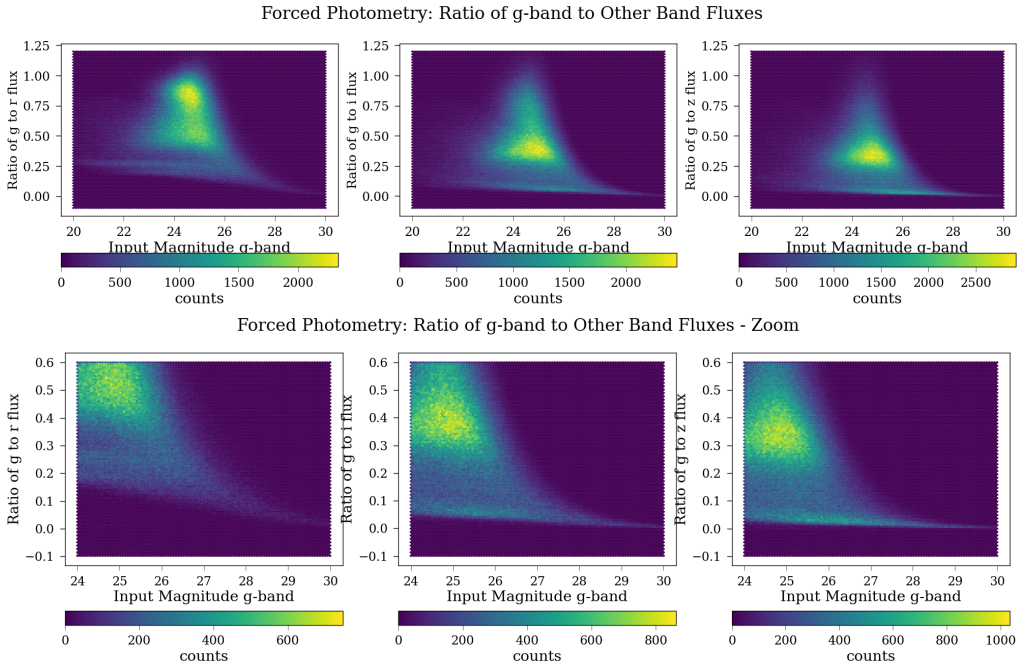


Figure 6.11: Shown here are the ratios of the g-band flux to the riz bands as a function of magnitude. The bottom plot is simply a zoom of the top plot. As can be seen, at high magnitude the g-band flux is tiny compared to the other bands. This shows that the only reason we have very faint detections past the detection limit of our survey in the above completeness curves is due to a forced photometry effect, and that objects based on the g-band flux alone would not have been detected. They are detected due to having higher fluxes in other bands and forcing measurements in the g-band.

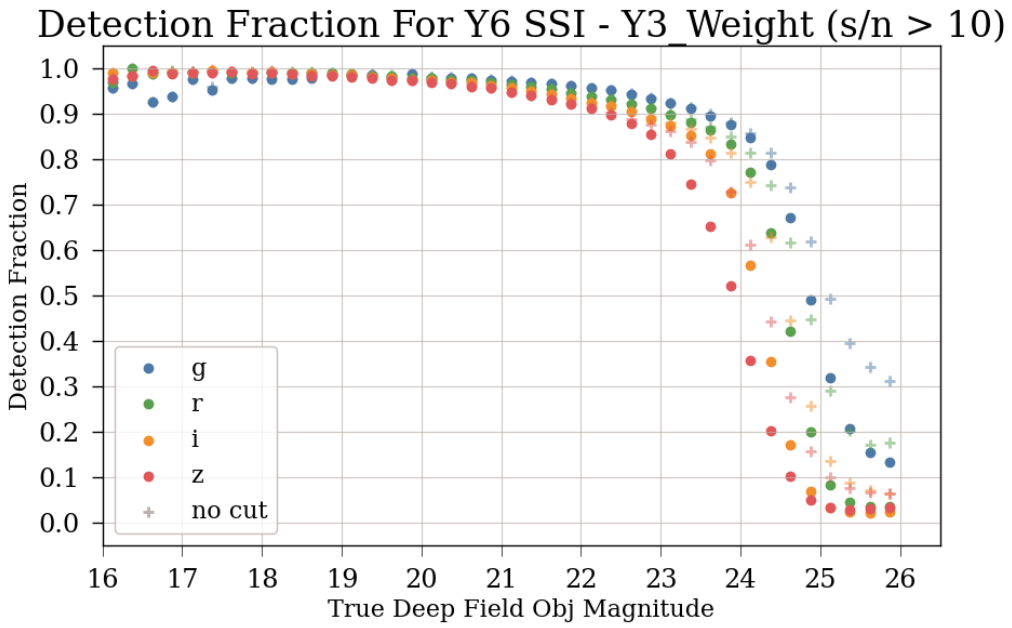


Figure 6.12: Similar to the plot above, these are the Y6 completeness curves as measured with the Y6 SSI runs. These curves are only for the 1/3 of objects that are randomly sampled from the DF for injection. Furthermore to mitigate bias from our image processing pipeline choices, a signal-to-noise cut is applied.

different injection schemes. The first plot is the measured - true magnitude of detected objects vs the true input magnitude. These are all for the i-band. The middle plot is showing the same information but as a box plot binned in true magnitude, where the means and medians are shown. Finally the third column is a histogram of the differences of magnitude for any true magnitude. Its clear to see that we are recovering the true magnitudes of objects very well up to about the 20th magnitude where the distributions diverge.

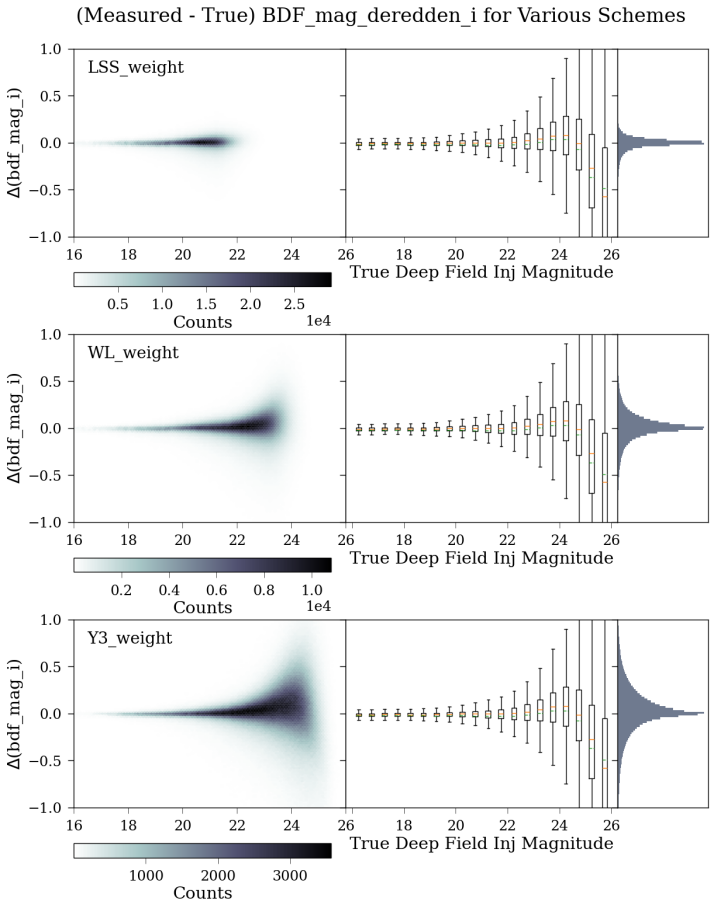


Figure 6.13: Shown here are the Measured - True i-band magnitudes for the detections in the Y6 SSI catalogs. This is the so called "transfer function". The left most column of plots shows a heat map of occurrences as a function of the difference and the true injected magnitude. The middle plots show the same information but binned in input magnitude to show the box plots including the middle 50%, mean and medians. At bright magnitude we do much better, with very tight agreement to 20th magnitude or so. The final column of plots is a histogram of differences summed across all magnitudes. The three different injection schemes are shown in rows. Note that for faint magnitudes, the recovered magnitudes are biased and non-Gaussian in a non-trivial way (non-symmetric). This highlights the need to run the Balrog process and shows where our naive intuition of Gaussianity can mislead us."

# Part III

# SSI Applications to Precision Cosmology

# SSI and Photometric Redshift Calibration

Here I outline DES's photometric redshift calibration technique which combines the SOMPZ, clustering redshifts, and shear ratios redshift distribution estimators. Particular attention is paid to highlighting how SSI is critical for the SOMPZ method, as well as contributes to the other two as well.

## 7.1 Introduction

Photometric redshift calibration of the weak lensing source sample is critical to DES's main cosmological analysis. Both the cosmic shear, and

galaxy-galaxy lensing measurements from the 3x2pt depend on the redshift distributions estimates, as well as many other analyses, see section 2.5 for more details.

In the case of cosmic shear, we want to map the matter density field through gravitational lensing. You can look at the distribution of nearer galaxies with estimated redshifts as a tracer of the matter density field, but they are a biased tracer. The only method for getting a direct connection to the underlying density field is through its affect on distant (source) galaxies by way of (weak) gravitational lensing. In order to be able to use the lensing signal to extract information about the intermediate density field, though, the distances to the lensed sources must be known.

One of the main applications of SSI in our precision cosmological analyses, is in the photometric redshift calibration of the weak lensing source galaxies. DES's method for calculating the redshift distributions of the weak lensing source galaxy sample involves combining information from three different likelihood functions: the Self-Organizing Map p(z), SOMPZ, which constrains redshifts from photometry, Clustering Redshifts, WZ, which constrains from cross-correlations of galaxy density functions, and Shear Ratios, SR, which constrains using the ratios of the galaxy-shear correlation functions at small scales. This method of combining likelihood functions ultimately assigns source galaxies to one of four tomographic bins, and estimates the redshift distributions of those bins. This method results in combined effective uncertainties of $\sigma_{\langle z \rangle} \sim 0.01$ on the mean redshift in each tomographic bin.

The following three sections will describe the three likelihood methods, with an emphasis made on the first method, SOMPZ, as the application of SSI is most directly related to this likelihood function. The other two likelihoods depend on SSI as well, but in a secondary manner through the measurement of the magnification bias, which will be discussed more in the following chapter: 8.

The overview of the SOMPZ method in particular but also the combination of all three as the redshift calibration method for DES Y3 is discussed in: *Dark Energy Survey Year 3 Results: Redshift Calibration of the Weak Lensing Source Galaxies* [Myles et al., 2021]. The Clustering Redshifts method is discussed in: *Dark Energy Survey Year 3 Results: Clustering Redshifts – Calibration of the Weak Lensing Source Redshift Distributions with redMaGiC and BOSS/eBOSS* [Gatti et al., 2021a]. And the Shear Ratios method and its applications to redshift constraints as well as its role as a probe in the 3x2pt analysis is discussed in: *Dark Energy Survey Year 3 Results: Exploiting small-scale information with lensing shear ratios* [Sá nchez et al., 2022].

## 7.2 Self-Organizing Map Photo-Zs (SOMPZ)

Ideally, if we wanted to have a catalog of galaxies for which we knew the redshift information very well, we would gather spectra for every individual galaxy, however that is not feasible here. This is discussed further in section 1.5, but there is a trade-off in photometric vs spectroscopic surveys for area vs more accurate redshifts. While we don't have precise spectra for our objects, we do have many many objects, 10s-100s of Millions of galaxies. And we do have noisy 5-band photometry for these objects, which can be thought of as a really low resolution spectral energy density (SED) curve with just 5 points.

Due to the degeneracies present in the color-redshift relationship, it's practically impossible to determine a galaxy's unique redshift from the 5 band-pass color filters we use. However, given a sample of galaxies with well known redshifts, you can find a method to re-weight that sample's n(z) such that the abundances of specific types of galaxies in that well known sample match the abundances that are detected and selected for in our much larger photometric sample. This is the heart of the SOMPZ method, which aims to characterize the DES source galaxy sample's

redshift distribution from it's photometry.

As we will see, Synthetic Source Injection plays an essential role in this method by connecting the deep fields where we have well known redshift information to the wide field where are trying to estimate the redshifts. A way to think about this is that SSI provides the mapping, or transfer function, for objects between the deep and wide fields. Specifically, SSI estimates for us what a deep field galaxy would look like in the wide field. Meaning that we could ask the reverse, "what would this wide field galaxy look like in the deep field?". Or rather, "given this wide field color-magnitude information, what deep field galaxies would have the same wide-field information, and what is their more well known redshift information?". By using SSI and specific samples with well known redshifts, we can extract more information than would seem naively possible from the 5-band noisy photometry. Where the fact that we have the deep fields catalogs and that our SSI method injects those DF objects is critical to the method.

## The Data

**Wide Field Weak Lensing Source Sample:** The source sample is a subset of the Y3 Gold data which passes metacalibration cuts. These cuts are defined in equation 7.1. The cuts were motivated to create a more homogeneous catalog and thus more accurate photometric redshifts. The bright end cuts remove close galaxies and residual stars, and the faint end cuts remove a region where the COSMOS catalog has been found to be more biased than we would like. Finally, the last two listed cuts remove unphysical colors which most likely came about from catastrophic flux measurement failures. After cuts, the weak lensing source catalog that results contains $\sim$100M galaxies.

$$
\begin{aligned}
18 < m_i < 23.5 \\
15 < m_r < 26 \\
15 < m_z < 26 \\
-1.5 < m_r - m_i < 4 \\
-4 < m_z - m_i < 1.5
\end{aligned}
\tag{7.1}
$$

**Deep Field Reference Sample:** The Deep Field sample of objects and the mock wide field photometry that SSI provides for those DF objects is the cornerstone of this method. There is a more detailed discussion of the Deep Fields in chapters 4 and 2. In general, in Y3, four fiducial Deep Fields were used, 3 within our survey footprint and one that overlaps the COSMOS field. In total there is 5.2 sq deg after masking that overlap with the UltraVISTA and VIDEO near-infrared (NIR) surveys. This results in 2.8M detections with measured ugrizJHK$_s$ photometry with limiting magnitudes 24.64, 25.57, 25.28, 24.66, 24.06, 24.02, 23.69, and 23.58 respectively. Which is considerably fainter than the faintest sources in the source galaxy sample discussed above. These Deep Fields are used to accurately measure the number density of galaxies in the deep ugrizJHK$_s$ color space where galaxy redshifts are well constrained.

**Reliable Redshift Information:** The reliable redshift information comes from the 8-band photometry of the DF objects, ugrizJHK$_s$, as well as two multi-band photo-z catalogs from the COSMOS field. The COSMOS2015 [Laigle et al., 2016] 30-band photometric redshift catalog (including 30 broad, intermediate, and narrow bands covering the UV, optical, and IR regions), and the 66-band PAUS+COSMOS [Alarcon et al., 2021] photometric redshift catalog. The spectroscopic catalogs used contains both public and private spectra from the following surveys: zCOSMOS [Lilly et al., 2009], C3R2 [Masters et al., 2017], VVDS [Le Fèvre, O. et al., 2013], and VIPERS [Scodeggio, M. et al., 2018]. These are used to create the fiducial

redshift distributions.

## Redshift Distribution Inference

The key to the redshift distribution inference method, SOMPZ, is going to be using a Self-Organized Map algorithm. This is an unsupervised dimensionality-reduction machine learning technique. In the SOM approach here, the dimensionality is reduced to 2D which makes the results highly interpretable. The locations of objects in the SOM cells represents a physical similarity, and as such you can more easily verify the methodology and identify groups of object contaminating the samples for instance. There are two SOM cells which get created, the 3-band wide SOM cells and the 8-band deep SOM cells. The wide data only utilizes the riz data, forgoing incorporating the g-band due to biases that come about from the difficulty of modeling the g-band PSF. SSI provides the link between the deep and wide SOMs as we will see next as I describe a high level overview of the SOMPZ methodology.

The probability distribution function for the redshift of a galaxy is given by equation 7.2, obtained by marginalizing over the deep photometric color, $x$. Where $\hat{x}$ is the observed wide-field color-magnitude, $\hat{s}$ is the passing of a selection function, and $\hat{\Sigma}$ is the covariance matrix.

$$p(z|\hat{x},\hat{\Sigma},\hat{s}) = \int dx\ p(z|x,\hat{x},\hat{\Sigma},\hat{s})p(x|\hat{x},\hat{\Sigma},\hat{s}) \tag{7.2}$$

This is a very high dimensionality problem that precludes direct computation. Instead, the color-magnitude spaces spanned by $x$ and $(\hat{x},\hat{\Sigma})$ are discretized into categories, $c$, and $\hat{c}$, which are referred to as cells and define a set of galaxy photometric *phenotypes*. The unsupervised machine learning method of choice used to organize these cells is a self-organizing map, or SOM. Through this SOM method, equation 7.2 turns into equation 7.3.

$$p(z|\hat{c},\hat{s}) = \sum_{c} p(z|c,\hat{c},\hat{s})p(c|\hat{c},\hat{s}) \tag{7.3}$$

Next, $\hat{c}$ is associated with tomographic bins according to a specific binning algorithm. Then the n(z) in each bin can be constructed by marginalizing of the constituent cells, $\hat{c}$ which belong to the given bin, $\hat{b}$. Every galaxy belongs to only one wide SOM cell, and each wide SOM cell belongs to only one tomographic bin. We are able to estimate the probability function as the following in equation 7.4.

$$p(z|\hat{b},\hat{s}) \approx \sum_{\hat{c}\in\hat{b}} \sum_{c} p(z|c,\hat{s})p(c|\hat{c},\hat{s})p(\hat{c}|\hat{s}) \tag{7.4}$$

This equation can be broken down into the three constituent probabilities. First, the *Lensing Weighted Wide SOM Cell Occupation*, which is the probability of a specific observed wide color-magnitude category given the passing of a selection, $p(\hat{c}|\hat{s})$. This can be estimated using the wide field data. Second, the *Lensing Weighted Transfer Matrix*, is the probability of a specific deep color-magnitude category given the observed wide category and passing of a section, $p(c|\hat{c},\hat{s})$. This is the transfer function, which is what SSI can give us. Finally, the *Lensing Weighted probability*, $p(z|c,\hat{b},\hat{s})$ is computed from the subset of the deep sample for which we have all three of the following: reliable redshifts, 8-band deep photometry, and Balrog realisations.

While the transfer function matrix is perhaps the most obvious place SSI comes into this redshift estimation, and indeed it is very important. Another interesting place that SSI factors in is in the *Lensing Weighted probability*. Here, each selected galaxy in the Balrog sample that goes into this term needs to be weighted by various quantities: the number of times it was detected, passed the selection, and assigned to the same bin; and normalized to the number of times it was injected. It is this term that motivated our new injection scheme in Y6. By optimizing the 2/3 of

the injections to be more likely to pass a metadetection cut (specifically I re-weighted the injection sample to favor bright galaxies, more details in chapter 6), there are more realizations of the same deep field galaxy to support the calculation of this term. That drives down the error in the *lensing weighted probability*.

In terms of the *Lensing Weighted Transfer Matrix*, this term benefits from more SSI realizations in general. Which is also achieved by the new weighting scheme, which by injecting brighter, has a higher overall detection efficiency. But, this is also helped by our 5x increased area coverage which was achieved through the pipeline upgrade which allowed me to run on multiple supercomputers in tandem.

**Uncertainty in the photometric n(z):** Sources of uncertainty in the redshift distributions come from several places. Sample variance affects the abundance of observed deep field galaxies at a specific color and redshift. There is shot noise in the counts of deep field galaxies. There can be uncertainties arising from bias in the reliable redshift samples used. Photometric uncertainty from the 8-band photometry used for the deep galaxies. And, uncertainty from the SOM methodology itself. As for the SSI uncertainty: variations across the footprint can affect this, In Y3, SSI covered 20% of the foot print randomly, so it is assumed to be negligible, but it's possible that there was some bias in the survey properties sampled purely through random selection. Covering the full footprint in Y6 will alleviate this possibility. In addition, it was found in Y3 that the internal noise in the SSI transfer function was negligible as compared to other sources of uncertainty in the method. However, we still strive to minimize our uncertainty as the other sources of error also get better.

## 7.3 Clustering Redshifts (WZ)

There are two other methods, Clustering Redshifts and Shear Ratios which play the essential role of providing additional, independent constraining power to validate and further constrain photometric redshift distributions. Each will be discussed briefly here.

Clustering Redshifts, also known as WZ, is the calibration of WL source galaxy n(z) distributions from clustering measurements. This works by measuring the cross-correlation signal of the unknown sample to a reference sample of high-fidelity redshifts divided into thin bins. Specifically, this method cross-correlates the WL source galaxies with the redMaGiC galaxies (luminous red galaxies with secure photometric redshifts) and spectroscopic sample from BOSS/eBOSS in order to estimate the redshift distribution. An advantage of this method is that the reference sample doesn't need to be representative of the unknown sample. The clustering method also assumes that a non-zero signal will only come about from a physical overlapping of samples in space.

In Y3, there were two methods used for WZ: "mean-matching" and "full-shape". The mean-matching method uses the clustering information to estimate a mean redshift as well as assign a likelihood for every candidate n(z) from photometric methods based on the photometric distribution's mean redshift. This is the simpler of the two methods. What was new in Y3 was the addition of the full-shape method which is more complex and accounts for magnification which can create an effect where an object crosses the detection limit or selection cut. This method also accounts for a myriad of other effects, detailed in full in [Gatti et al., 2021a]. In this method, the clustering n(z) and the photometric n(z) are used as probabilities of the observational data given a true n(z). Then we sample the full n(z) from the posterior p[n(z)] implied by multiplying these probabilities. Results were measured on simulations of the two methods as well as systematic

uncertainties tested. The systematic errors were estimated at 0.014 on the mean redshift.

It should be noted that this more complex method, full-shape, accounts for magnification, which relies the measuring of the magnification bias using SSI. This application of SSI to precision cosmology will be discussed further in the next chapter: 8.

## 7.4 Shear Ratios (SR)

The third method is Shear Ratios (SR) which uses small angular scale galaxy-galaxy lensing to constrain the redshift distributions. Specifically, the ratio between the galaxy shear two-point correlation functions using the same lens sample. This observable, the ratio, cancels out the dependency on the galaxy-matter power spectrum which at small scales has modeling issues. In fact, the "shear-ratio likelihood" not only constrains redshift uncertainties, but a number of other astrophysical parameters, including nuisance parameters, helping to better constrain our cosmological results. This complements the 3x2pt analysis by adding another probe besides the three 2pt correlation functions.

In this method we take ratios of correlation signal of different source redshift bins using the same lens bin, and then repeat for various lens bins. These ratios allow us to keep the small scale information that would otherwise have been thrown out for the standard cosmological analysis. Again, this method relies on the magnification bias which is estimated using SSI, and will be discussed further in the next chapter: 8. For Y3, shear ratios were included in the 3x2pt analysis as an extra probe, through which they helped constrain the weak lensing source redshift distributions.

## 7.5 Combined Methodological Results

The combination of the SOMPZ and Clustering Redshifts methods can be seen in figure 7.1. The consistency between the methods was tested and agreed well. The WZ constraints on the mean redshift, $\bar{z}$, are weaker than that of SOMPZ, however WZ constrains the smoothness and shape much better. This can be seen in the figure; when WZ is added to SOMPZ the curves are smoother in nature. Due to this, the combination of SOMPZ and WZ is better constraining than one alone. As stated above, the Shear Ratios were added to the 3x2pt analysis as an independent probe, through which they contribute to constraining the redshifts.

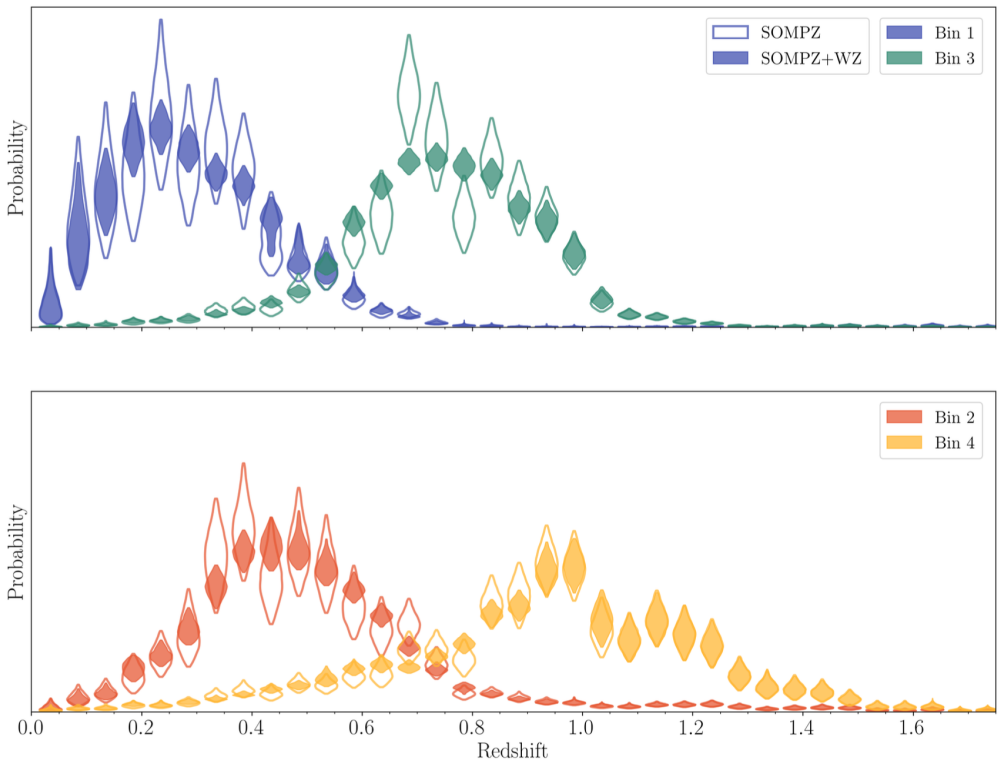


Figure 7.1: This is a visualisation of the redshift distributions where each violin represents a 95% credible interval of the probability of a galaxy in the weak lensing source sample and assigned to a given tomographic bin to have a specific redshift. The SOMPZ method alone is shown in open violins, and the combination is shown with shaded violins. The effect of adding the clustering redshift information is a narrowing of the probability range and a smoothing of the overall shape [Myles et al., 2021].

# 8

# SSI and Magnification Bias on Clustering Samples

Estimating the magnification bias coefficients of the lens galaxy sample is possible through the use of SSI, and was the fiducial method of such in DES Y3. Here, I explain the methodology for that estimation and the results from Y3.

## 8.1 Introduction

Another main application of Synthetic Source Injection in Y3 is in the estimation of the magnification coefficients. Gravitational lensing from intermediate matter creates a magnification effect on background galaxies.

This can cause them to move through the detection limit, as well as effect the selection of galaxies. In *Dark Energy Survey Year 3 results: Magnification modeling and impact on cosmological constraints from galaxy clustering and galaxy-galaxy lensing* [Elvin-Poole et al., 2023], the magnification coefficients for the two Y3 lens galaxy samples was measured and the effect of magnification on galaxy clustering and galaxy-galaxy lensing was explored. We accounted for systematics by using the Y3 SSI which naturally inherits many of the same systematics as the real data.

As statistical power increases with surveys, such as DES which has both a large area coverage and deep imaging, more subtle effects need to start being accounted for like the magnification of objects. Magnification of galaxies effects the number density of observed galaxies and thus impacts the galaxy clustering and galaxy-galaxy lensing signals. Galaxy clustering is a method to probe the underlying mass density, however it's complicated by the galaxy bias, the relationship between galaxy density and matter density. This is hard to model theoretically, so it's hard to extract cosmological information, such as the matter density, from maps of the galaxy density alone as you need to know the conversion factor, or bias. Galaxy-galaxy lensing lets us probe the total mass distribution in the foreground region and breaks the degeneracy between the galaxy bias and the amplitude of total matter clustering. This is one of the reasons we want to combine galaxy clustering with galaxy-galaxy lensing with the, so called, 2x2pt analysis. However, with the statistical power that we have from the large amount of galaxies in our samples, its necessary for these probes that we start to account for magnification effects. And it will become more and more important for future surveys to account for this effect. Here we look at the effect of magnification on both the size and flux selection, and viability and necessity of including it in the fiducial 3x2pt analysis, in addition to testing the utilization of SSI in order to measure the magnification coefficients.

## 8.2 Magnification Formalism

Magnification can be expressed in terms of the convergence, $\kappa$, and shear, $\gamma$, which stretches the source galaxy tangentially as seen in equation 8.1.

$$\mu \approx 1 + 2\kappa, \;\; \kappa \ll 1 \text{ and } \gamma \ll 1 \tag{8.1}$$

In magnification, the trajectory of the source galaxy photons is altered on its way to us by the intermediate lens mass. For a positive convergence, which magnifies the background galaxies by increasing their size, two effects take place. First, the distance between two points on the source plane is increased. Second, we observe a greater fraction of the solid angle of light emitted from the source galaxy. Through these two effects, the apparent position of the galaxy along with the distribution of light is altered in the case of magnification. For our large scale survey where we are most interested in the number density of galaxies this results in two responses. First, the distance of the centroids of galaxy images will increase, such that an area element on the unlensed sky, $\Delta\Omega$, is mapped to a larger area element on the lensed sky by a factor of $\mu$: $\Delta\Omega \rightarrow \mu\Delta\Omega$. **Thus the number density of objects in an observed area decreases by a factor of $\mu$.** Secondly, galaxy surface brightness is conserved, so that if the apparent area increases, the image size increases and the total flux of an object will increase. Objects that enter these samples are selected for based on their size and flux. **Thus, a change in the selection probability for individual galaxies occurs.**

The galaxy over-density due to magnification can be written as equation 8.2 as a function of the position on the sky, $\hat{n}$.

$$\delta_{gal}(\hat{n}, \kappa) = \frac{n(\hat{n}, \kappa)}{n(\hat{n}, 0)} - 1 \tag{8.2}$$

We can simplify this equation to the form given in equation 8.3. With

$C_{area} = -2$, the total magnification contribution is defined by a single constant dependant on the redshift bin, $i$.

$$\delta_{gal}(\hat{n}, \kappa) = \kappa(\hat{n}) \left[C_{area} + C^i_{sample}\right] \tag{8.3}$$

If the galaxy selection is simply made from a cut on magnitude, $m_{cut}$, this formula turns into equations 8.4 and 8.5. Where $N_\mu(m)$ is the cumulative number of galaxies as a function of maximum magnitude, $m$.

$$\delta^i_{gal,mag}(\hat{n}) = 2[\alpha^i(m_{cut}) - 1]\kappa^i(\hat{n}) \tag{8.4}$$

$$\alpha^i(m_{cut}) = 2.5\frac{d}{dm}\left[\log N_\mu(m)\right] \tag{8.5}$$

Although we have been talking about sources and lenses a lot, these two don't necessarily need to be the "weak lensing source sample" and the "lens sample" as we usually mean them to be in DES. In particular, in Y3, this magnification work focused on measuring the magnification of the lens sample from intermediate mass, between us, the observer, and the nearer lens galaxies. Here we will look at the observed galaxy density as given in equations 8.6 and 8.7. The weak lensing source sample magnification effects actually enter in as higher order corrections, and are ignored for now.

$$\delta^i_{g,obs} = \delta^i_{g,int} + \delta^i_{g,mag} \tag{8.6}$$

$$\delta^i_{g,mag}(\vec{l}) = C^i\kappa^i(\vec{l}) \tag{8.7}$$

Here, $\kappa$ is the convergence that the lens galaxies are subjected to in a redshift bin, $i$. And we have now moved to the harmonic transform of the density contrast. This change in density contrast will affect the galaxy clustering and galaxy-galaxy lensing correlation functions. Thus

its imperative that we can measure or model the $C^i$ factors.

## 8.3 Methodology

### Data

**Lens Sample - MagLim:** MagLim was used as the fiducial lens sample for the Y3 Cosmological analysis. MagLim, named for the fact that it's a magnitude limited sample (only), is a much simpler cut than our fiducial sample for Y1, RedMaGiC. MagLim has a magnitude cut that depends on the redshift with the following relation $i < 4z_{photo} + 18$, where $z_{photo}$ is the photometric redshift as defined by the DNF algorithm [De Vicente et al., 2016]. This sample results in 3.5 times the number of galaxies as in the RedMaGiC sample and is split into 6 tomographic bins with the following edges: $z = [0.20, 0.40, 0.55, 0.70, 0.85, 0.95, 1.05]$.

**Lens Sample - RedMaGiC:** The RedMaGiC sample was the fiducial lens sample in Y1, and was also used in Y3 along side MagLim. It selects Luminous Red Galaxies (LRGs) through the RedMaGiC Algorithm [Rozo et al., 2016]. It is divided into 5 tomographic bins with edges: $z = [0.15, 0.35, 0.50, 0.65, 0.80, 0.90]$.

Both the MagLim and RedMaGiC samples are re-weighted in order to correct for their density dependence on observational properties, discussed more in section 9.1. As well, a mask is applied such that all samples are expected to have a uniform selection function across redshift bins.
**Source Sample:** As talked about previously, the other main sample that is used in DES analyses is the weak lensing source galaxy sample. While most of the work here is devoted to characterizing the magnification of the lens samples, the source sample still plays a role in galaxy-galaxy lensing.

This sample contains 100M galaxies split into 4 tomographic bins with mean redshifts from .34 to .96 in Y3.

## Simulations

**DES Y3 SSI:** The first of three simulations that will be discussed is the use of Synthetic Source Injection. This is also the one that we will focus on as it pertains to my work in this thesis the most. In Y3, 20% of the footprint was re-run with SSI, where we injected models of Deep Field galaxies into single-epoch images, and ran these through the image processing pipeline and measured the mock wide field photometry of the deep field objects. By creating a initial "truth" catalog and a final "measured" catalog we can measure the survey transfer function. Full details about this methodology can be found in chapter 5. In addition to the $\sim$2,000 tiles run in Y3, an additional random 500 tiles were rerun with small magnifications applied to the objects. Specifically, we laid down the same objects in the same spots on the sky but with a 2% magnification applied to each image.

**N-Body Simulations:** The *Buzzard* suite contains 18 synthetic DES Y3 galaxy catalogs. Photometric errors are applied to the catalogs using error distributions created from Y3 SSI. A RedMaGiC sample is selected from each catalog with the same selection criteria as DES Y3 data. The *MICE* simulation is another large N-body simulation. RedMaGiC and MagLim sample were selected from this catalog.

## Estimating the Magnification Coefficients

As discussed in the methodology section, we want to estimate, $C$, the response of the galaxy density to the convergence, $\kappa$. $C$ can be split into two terms: $C = C_{area} + C_{sample}$, where $C_{area} = -2$. $C_{sample}$ can be measured

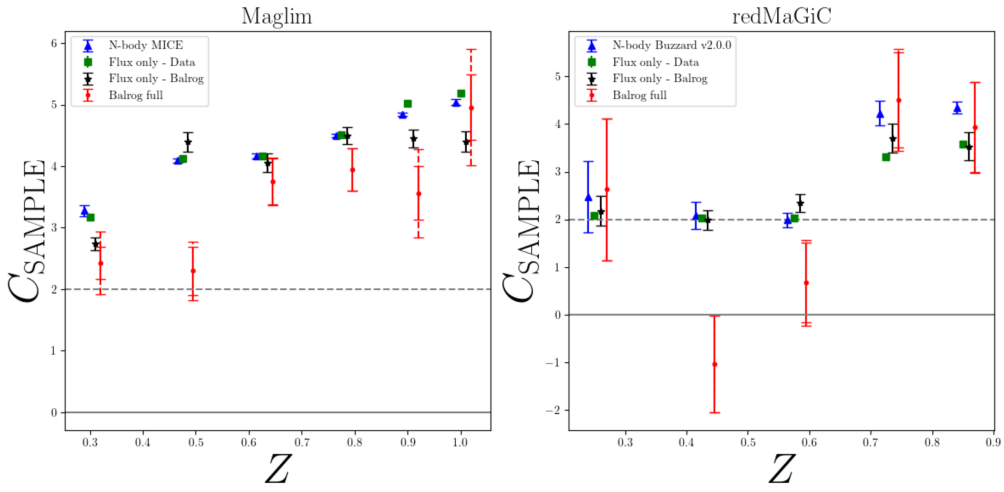


Figure 8.1: Estimations of the magnification bias parameter for the galaxy clustering sample. Blue points are from an N-body simulation, green and black points are from a simplistic estimator calculated on real data and SSI data respectively. Red points are the full estimator on the SSI data, these points were used as the fiducial estimates in Y3 for the coefficients and are thought to be the most accurate of the four [Elvin-Poole et al., 2023].

in the simulations by counting the fractional change in the number of galaxies that are selected for a small convergence, $\delta\kappa$, this is given in equation 8.8. Where N is the number of selected galaxies. This $C_{sample}$ is measured for a variety of simulations as discussed next.

$$C_{sample} = \frac{N(\delta\kappa) - N(0)}{N(0)\delta\kappa} \tag{8.8}$$

## 8.4 Y3 Results

### Y3 SSI Magnification Estimation

Our SSI magnification runs in Y3 used the same galaxies in the same locations as the original injections, but with a magnification applied of

$\delta\mu = 1.02$ or $\delta\kappa \approx 0.01$. This magnification level was chosen so that we obtain a sufficient number of detections that cross the detection limit, so that we can measure $C_{sample}$, but with a small enough $\kappa$ that we are still in the regime where equation 8.1 holds true.

RedMaGiC and MagLim selections are applied to both the regular SSI run and the magnification run. $C_{sample}$ is then estimated from equation 8.8. The results of this can be seen in figure 8.1 in the red points labelled "Balrog - full".

The shot-noise error due to the finite area of the Y3 SSI realizations is estimated in equation 8.9. Where the "only" denotes that the object was found only in that sample, without convergence for example, and not in the other sample, with convergence. The statistical error bars are shown in the figure as well.

$$\frac{\sigma^{stat}}{C^{balrog}_{sample}} = \sqrt{\frac{N(0 \text{ only}) + N(\delta\kappa \text{ only})}{[N(\delta\kappa) - N(0)]^2} + \frac{1}{N(0)} + \frac{2N(0 \text{ only})}{N(0)[N(\delta\kappa) - N(0)]}} \tag{8.9}$$

## Perturbing Measured Fluxes Estimation

This method is used on the real data from Y3, and is very simple in nature. A small flux offset, $\Delta m$, is added to the fluxes of the real objects and a new selection is made using those new perturbed fluxes. While this is a simplistic measurement on the effect of magnification that neglects many factors by not rerunning photometry, it is nonetheless useful. The measurements for this method on the real data can be seen in figure 8.1, by the green marks, "flux only - data".

This same method was run on the Y3 SSI data as well, the results of which are again shown in figure 8.1, by the black marks, "flux only - Balrog". If the SSI data was mimicking the real data exactly, we would expect the

green and black marks to overlap, however they are offset slightly. Using this a measure of additional error in the SSI realizations, new error bars are added to the figure for the red marks which denote the total error, this discrepancy to map the real data exactly in addition to the statistical error.

### N-Body Simulation Estimation

Finally, the results of the N-Body simulations can be seen in figure 8.1 in the blue marks. For MagLim the MICE simulation is shown and for RedMaGiC, the Buzzard simulation. While in the simulations you know the true convergence and they account for the change in positions and fluxes, they do not simulate the full impact of lensing. Specifically, the selection response is only due to changes in fluxes.

### Comparison of Results

As can be seen in figure 8.1, the Y3 SSI $C_{sample}$ measurements are typically lower than the other estimation methods, especially at low redshift. It can also be seen though, that the agreement between SSI and real data in the simple flux-only case does agree pretty well as can be seen by the green and black marks. Despite this tendency for SSI to measure lower values of $C_{sample}$ than the other methods, since SSI incorporates a myriad of effects and systematics that the other three methods don't, but which are representative of the real data, survey conditions, and image processing pipeline; it is believed that the SSI measurements are the most accurate method and were used as the fiducial estimates for Y3.

## 8.5 Impact on Y3 Analyses

An estimation of the impact that magnification would have on the galaxy clustering + galaxy-galaxy lensing analysis, called 2x2pt, was estimated

for Y3. It was found that magnification had the largest impact for galaxy-galaxy lensing of high redshift source bins. And for widely separated bin pairs in the clustering cross-correlation, the magnification signal was also the highest. However, the impact of this on the 3x2pt analysis is not so clear, as the largest signal contribution from galaxy-galaxy lensing on the data vector is from the lowest redshift bins, and the cross-correlation of galaxy clustering is not included in the fiducial 3x2pt analysis.

However, the impact of including these magnification estimates on the 3x2pt analysis was modeled using a noiseless data-vector. It was found that including the cross-correlation clustering signal did better constrain the cosmological parameters. It was also shown that you could let the magnification parameter vary freely without affecting the constraining power on $S_8$.

## 8.6 SSI Y6 Initial Results

We can try to estimate how much better we will be able to do in Y6 just from an increase in a number of SSI objects. Shot-noise from equation 8.9 goes like $1/\sqrt{N}$ , such that with a higher area of 5x in Y6 we expect a statistical noise reduction by a factor of $\sqrt{(5)} \approx 2.36$. But we will also get a boost in recovered objects that pass MagLim and RedMaGiC cuts due to the new injection scheme. This is difficult to estimate without DNF photo-z's for the SSI objects. But looking at the increase in objects that pass a metadetection cut can give us a rough estimate for this effect. In Y6, we get roughly a $4$x increase in number of objects that pass a metadetection cut solely from the new injection scheme. Meaning that we will have a combined $20$x increase in statistical power for a metadetection sample. Assuming this factor holds, that would be a $\sqrt{(20)} \approx 4.5$x improvement in the noise.

Furthermore, some of the disagreements between the real and SSI data

in the flux-only analysis could be due to the fact that in Y3 SSI did not replicate the image processing pipeline exactly, specifically a different single-object-fitting (sof) methodology was used for the photometry in SSI than for the wide-field data. This has been fixed in Y6, and we expect better agreement now.

# 9

# SSI and Large Scale Structure Systematics

There are many many more applications of SSI, but of particular interest to me were applications to systematics control in the context of Large Scale Structure. A few of those applications will be discussed here including independent verification of the lens galaxy sample weight maps, investigations into the impact of Galactic Cirrus on our image detection pipeline, and more.

## 9.1 Lens Galaxy Sample Weight Map Validation

There are two lens galaxy samples for DES in Y3 and Y6: the redMaGiC, a sample of Luminous Red Galaxies (LRGs) chosen with the redMaGiC algorithm [Rozo et al., 2016], and MagLim, a magnitude limited sample that is optimized for cosmological constraints [Porredon et al., 2021]. These two samples are used, in part, for the galaxy clustering two-point correlation which is one of three correlations that make up the 3x2pt analysis, or key project.

### Weight Maps for the Lens Galaxy Sample

One of the main challenges with the clustering signal, is that the lens galaxy samples contain systematics that are tied to the survey property conditions. Fluctuations in conditions, such as airmass or galactic dust, across the footprint result in observed galaxy density fluctuations which come not from cosmology but systematics. Thus in order to be able to use the lens galaxy sample reliably, these fluctuations due to survey properties need to be corrected for.

A full treatment of the re-weighting procedure is discussed in: *Dark Energy Survey Year 3 Results: Galaxy clustering and systematics treatment for lens galaxy samples* [Rodrí guez-Monroy et al., 2022], here I will give an overview.

Survey Properties (SP) alter the observed galaxy density field, and their effect needs to be mitigated. Healpix maps for the various SPs are created, the maps influence on the galaxy density is characterized, and then corrected for. The survey properties that were included in the Y3 analysis include: [airmass, fwhm, exptime, t_eff, skybrite, skyvar, sfd98, stellar_dens] among others. The summary statistics used for the maps vary including min, max, and means. Most of the maps also have separate

griz components. In total 107 SP maps were considered in Y3 for the weight-correction procedure.

By using principal component analysis, an orthogonal set of SP maps, called PC maps, is created and ordered by the total variance they capture. By keeping the 50 most important PC maps, 98% of the variance is captured. By using a smaller set of maps you reduce the likelihood of over-correcting and removing real signal.

The fiducial correction method used in Y3 was Iterative Systematics Decontamination (ISD). The procedure is as follows: identify the most significant PC map, create a weight map to correct for it, apply the weight map to the data; and repeat these steps finding the new most significant weight map. The validation of this weighting method is done on simulated catalogs. The mocks are contaminated using the inverse SP maps, and then decontaminated using the ISD methodology. The result of this decontamination on the galaxy clustering correlation function can be seen in figure 9.1. The black line is the original uncontaminated mock, the red represents the contamination of the mock with the SP maps, and the blue is the ISD decontamination method applied to the mock. Clearly, the ISD method works well to decontaminate mock, but not go so far as to over-correct and remove real signal.

## SSI Validation of the Weight Maps

While the decontamination scheme in Y3 had a preexisting validation method, we came up with an additional method using Synthetic Source Injection. One of the problems with the method described above is that it relies on us enumerating survey property maps and being able to measure and construct them. There could be contaminates from maps we didn't enumerate, or maps we can't, as we can't measure them. This is where SSI comes in. The synthetic sources, since they are injected into real images, inherit these systematics. We aren't creating a list and forward modeling

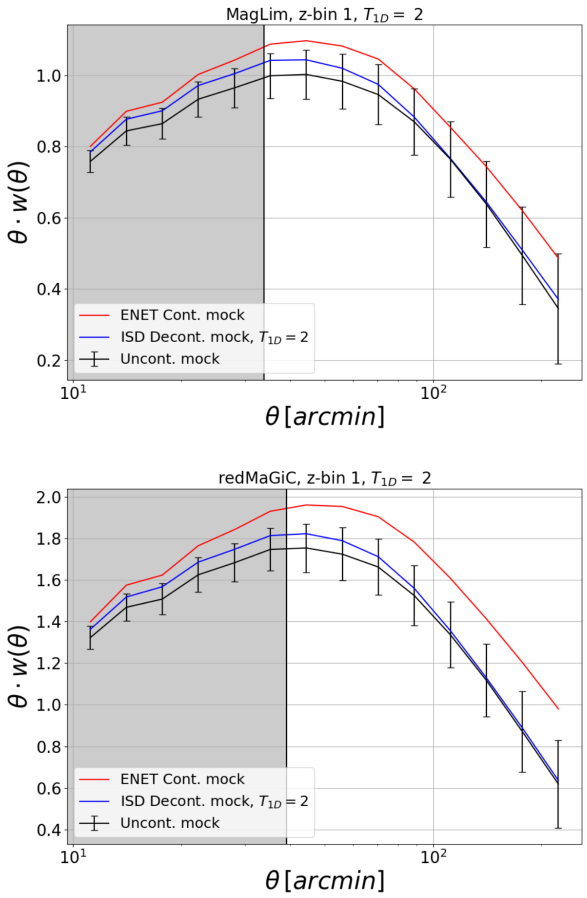


Figure 9.1: Shown here are mean angular correlation functions for mock data for both a MagLim sample (top) and a RedMaGiC sample (bottom). The black lines represent an uncontaminated mock. The Red lines are the same mock but now contaminated with DES survey properties such that the observed galaxy density depends on variations in these properties like airmass, exposure time, etc. The blue line represents the decontamination of the red line with the weight maps. As can be seen, the weight maps successfully decontaminate the mocks to a large degree, but do not over correct so as to pull real signal out of them. [Rodrí guez-Monroy et al., 2022]

the systematics, they just come along within the SSI realizations as a consequence of our methodology.

In the case of our observations, we observe the properties of a galaxy, $P_{obs}$ which is a function of both the true properties, as well as the systematics, $P_{obs}(P_{true}, \vec{S})$. If you think of the true full list of systematics as $\vec{S}$, made up from individual components such as: $\vec{S} = S_{airmass} + S_{skyvar} + ...$, in order to decontaminate the galaxies, and pull out $P_{ture}$, you need to know and characterize the full list of systematics. However, we can measure this, $\vec{S}$, with SSI. The difference between the true properties of the Deep Field galaxies we inject, $P_{true}^{SSI}$, and the measured quantities we obtain, $P_{obs}^{SSI}$, should be that full list of systematics, and a direct measurement of $\vec{S}$, with a couple caveats. The first being that in Y3 we didn't reproduce the image processing pipeline that the wide field data used perfectly. Specifically, we used a different photometry fitting method, so some small differences can be due to this. Second, there are some affects that take place before we inject that we can't account for, such as PSF modeling. So while we can't use SSI to say that all systematics are accounted for adequately in the weighting method, we can use it look for unaccounted systematics.

The key to this test is that while our SSI realizations pick up the same systematics as the real lens samples, they are laid on a grid, and shouldn't pick up any of the large scale structure signal. So, if we cross-correlate our Y3 SSI sample with the Y3 MagLim and redMaGiC samples, and see a signal, we could attribute that to an unaccounted for systematic. This is exactly what I did in Y3, and is shown in figure 9.2 for the redMaGiC and MagLim samples. The red signal is the cross-correlation without weights applied, and the purple is with weights. The blue points denote the strength of the signal for the clustering correlation function for each sample. In the circumstance where the there are no unaccounted for systematics, we would expect to see the purple line consistent with zero, meaning there is no correlation signal between the randomly injected

SSI samples containing systematics and the decontaminated lens galaxy samples. And that does appear to be true across most of the angular scales, especially for the MagLim sample. For redMaGiC, there does appear to be a slight increase in correlation signal at high angular distance, with some of the points still consistent with zero within the error.

In Y3 we used this a null-test as the statistical power of SSI wasn't great enough to make a statement about a potential signal in the high angular regions of the redMaGiC sample. However, in Y6 we will have 5x the area coverage as well as a boosted injection fraction for these lens samples which should allow us to drive down the error bars on this plot and make a more concrete statement. In addition, since the work in Y3, I along with the LSS - Systematics team have been looking into considering more systematics maps for this re-weighting methodology. SSI helped in identifying some of these maps, which will be discussed more in the following section: 9.2.

## 9.2 Galactic Cirrus Systematics

### Galactic Cirrus in DES

Galactic Cirrus, also referred to as infrared cirrus, shows up across the sky, but is typically seen in high galactic latitude away from the galactic plane. The structures, which look cloud like, thus the name, have historically been seen in the 60-100 $\mu$m range. One of the first studies of the galactic cirrus was in 1984, using data from the Infrared Astronomical Satellite (IRAS) [Low et al., 1984]. While typically studied and seen well into the infrared spectrum, deep surveys, such as DES, have been known to pick up cirrus as the dust reflects visible light. The top panel of figure 9.3, shows a DES image with little to no galactic cirrus, where as the middle panel shows a different part of the sky with significant galactic cirrus;

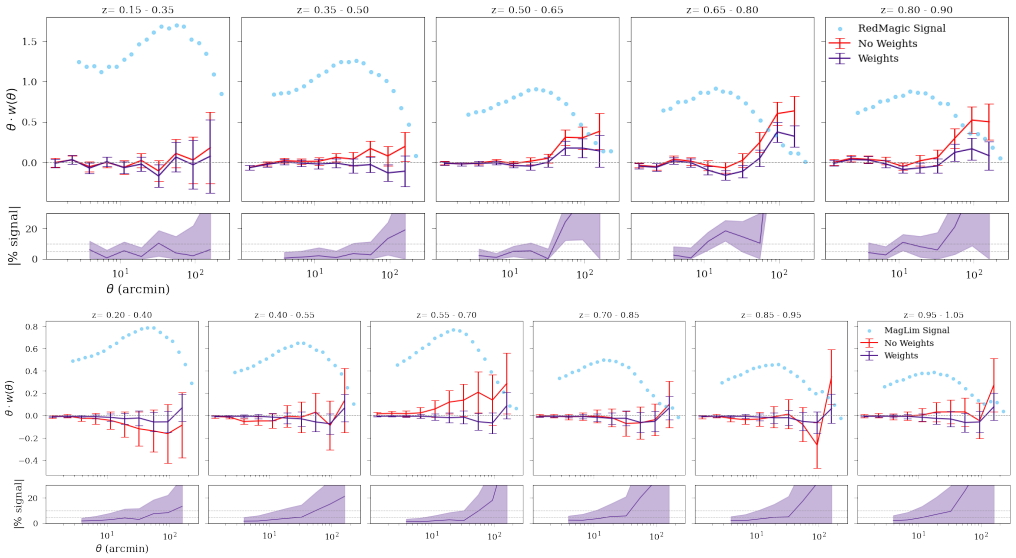


Figure 9.2: A weight map validation test using the SSI data in Y3. The RedMaGiC and MagLim galaxy samples trace real structure, where as the SSI detections, injected on a grid should not. They do both have the same survey property systematics influencing them though. Thus, a correlation in signal between the weighted galaxy samples and the SSI sample would be indicative of an unaccounted for systematic. In both samples, the correlation is consistent with zero on most scales, providing a null test for the weight maps.

appearing as wispy cloud like structures. The presence of Galactic Cirrus in our images creates issues in our image processing pipeline. The bottom panel of 9.3 shows our Y6 detections for the same region of space as the middle panel. Yellow rings denote all detections, and red denotes those that pass a GOLD cut. There are quite a few detections within the area of high cirrus on the right hand side of the image, some of which are thrown away with a gold cut and some which are not. This leads to questions about the integrity of the detections within that area that are passing the GOLD cut.

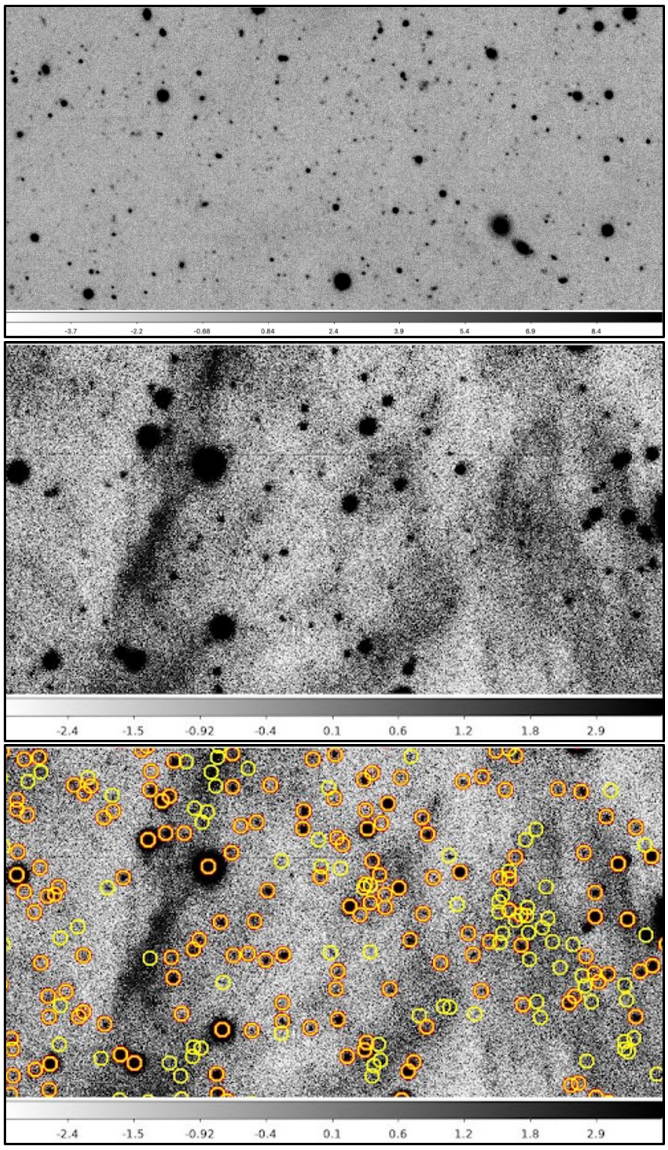


Figure 9.3: An image from DES with very little galactic cirrus (top) and a lot of Galactic Cirrus (middle). The bottom image is the same as the middle, but with Y6 detection marked. Yellow circles are all detections and orange are those that make it past a GOLD selection for quality cuts. It's clear that there are detections making it into the GOLD sample in regions of heavy Cirrus motivating our investigations of its impact on measured photometry. Images Courtesy of: Brian Yanny (DES).

## Super-Spreader Objects in DES

We will take an aside shortly to discuss a seemingly unrelated topic, but which will turn out to be heavily related to our cirrus discussion above. This topic is of a population of outlier objects that were identified and flagged by our SSI analysis in Y3; the so-called super-spreader objects. A topically humorous name given during the global pandemic of 2020.

In the Y3 SSI analysis, while looking into objects that had very high magnitude differences, $\Delta m = (\text{Measured} - \text{True})$magnitude, a population was identified that had correlated errors in the measured, cm_T, which is the characteristic size of an object (very near 0 being point like objects, stars or very distant galaxies, and larger being extended objects, galaxies). Image cut-outs or MEDS are given for 8 catastrophic [fitting] failures from Y3 in figure 9.4. Due to errors in the image processing pipeline, the MEDS stamp which is centered around the detected object, is much larger than it should be. The red ellipses show the 50% and 95% enclosed light apertures, which are clearly way too large for the objects in question. This leads to a huge flux and thus magnitude discrepancy.

While interesting to be able to identify this failure mode of the image processing pipeline, it's a very small percentage of objects that fell into this category, so you could say, "don't worry about them". However, what is really concerning here is that all these detections passed the GOLD cuts, and would typically be considered "science quality" measurements. Thus, we wanted to be able to identify these objects with a cut that could be applied to the gold catalog, such that any real objects which also fell into this catastrophic fitting failure mode were eliminated from our science sample. In coordination with the science release team, a cut was made for Y6 for the "super-spreaders" based on the size, BDF_T, and its error, BDF_T_ERROR. This was a great example and show for the utility of incorporating SSI into a survey's standard analysis playbook. In this mode, SSI served as an outlier discovery tool, and was able to improve the

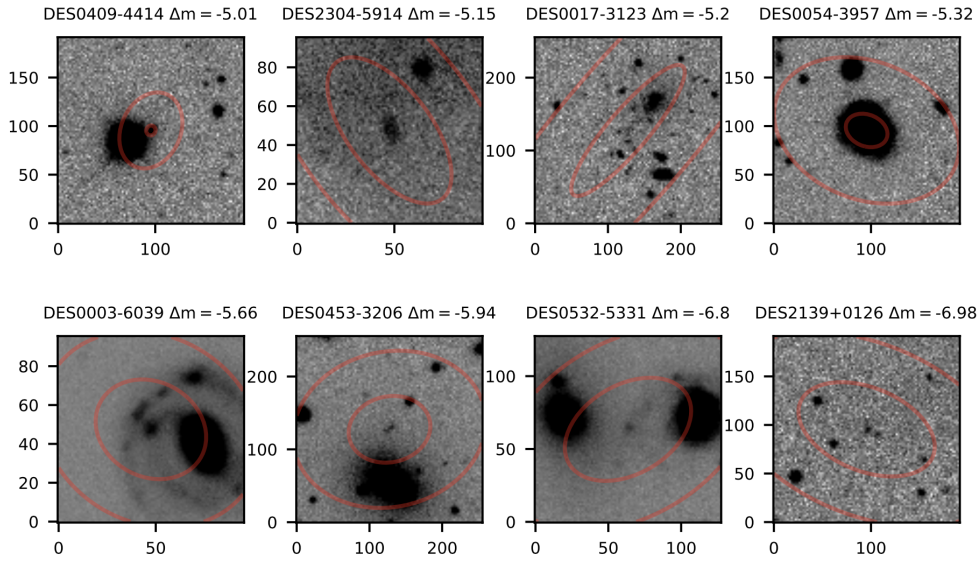


Figure 9.4: Examples of 8 catastrophic failures in photometric fitting of Y3 SSI sources. Red contours are 50th and 95th percentile flux contours for the detected object which is centered in the image. All 8 of these sources passed our GOLD cuts in Y3 [Everett et al., 2022].

accuracy of the Y6 science sample by identifying a failure mode and aiding in creating a cut to eliminate it from the science sample (more accurately, a FLAG is created, that groups may choose to cut on).

This isn't the end of the story of the super-spreaders though. We also investigated in what types of conditions does this catastrophic failure mode occur. By looking at the 8 MEDS image-cutouts in figure 9.4, in addition to many other quantities; its clear that one condition that correlates is a crowded field. We also found this occurs near bright stars, and un-flagged image artifacts. Another hypothesis that came about from this investigation was that this effect also occurred in regions with high amounts of galactic cirrus. This was one of the projects that I carried forward from Y3 into Y6 to keep investigating.

## Nebulosity Measurements

In order to investigate the link between catastrophic fitting failure modes, which are seen by super-spreader objects, and the amount of Galactic Cirrus, we needed to create a map of the Galactic Cirrus in our survey. To the best of our knowledge, such a map hasn't been created by anyone before, of the Cirrus specifically. We utilized a tool called, MaxiMask, which is a tool for identifying contaminants in astronomical images using convolutional neural networks [Paillassa et al., 2020]. Among other things, MaxiMask is able to identify nebulous, or cloud like, gas features in images. After using this program on our DES images, we obtain a "Nebulosity" healpixel map, with values ranging from 0 to 1, representing a probability that that pixel contains nebulosity. A map of nebulosity can be seen in figure 9.5. This methodology was validated by comparing the nebulosity map to individual DES images and confirming that regions with high galactic cirrus were also regions with high nebulosity probabilities.

The next question to ask was whether nebulosity correlated to super-spreader objects. You can see this by eye in figure 9.6. While on a large scale the correlation is washed out by super-spreader fluctuations, zooming into specific regions, as seen in the second column, shows a clear visual correlation between high values of nebulosity and super-spreader number density. This was further confirmed by plotting the correlation between the two, as can be seen in figure 9.7.

## Nebulosity and LSS Contamination

Now that we know that there is a correlation between our nebulosity maps and super-spreaders which are indicative of catastrophic fitting failure modes, a more general question would be what other negative effects can large amounts of Galactic Cirrus impart on our samples. This investigation then became a part of the Y6 Large Scale Structure - Systematics analysis

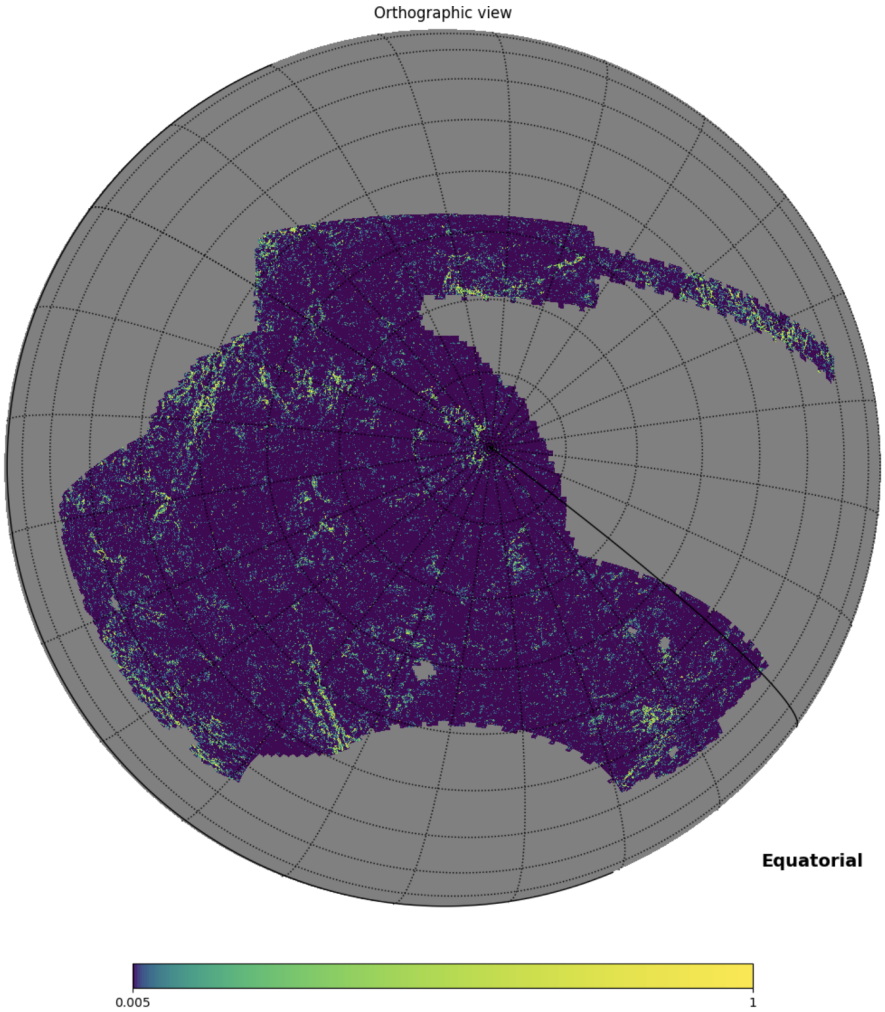


Figure 9.5: A map of the measured probability of nebulosity for the DES footprint. The map was created using MaxiMask to detect nebulous cloud like structures in images. We use it as a proxy measurement of Galactic Cirrus in our images.

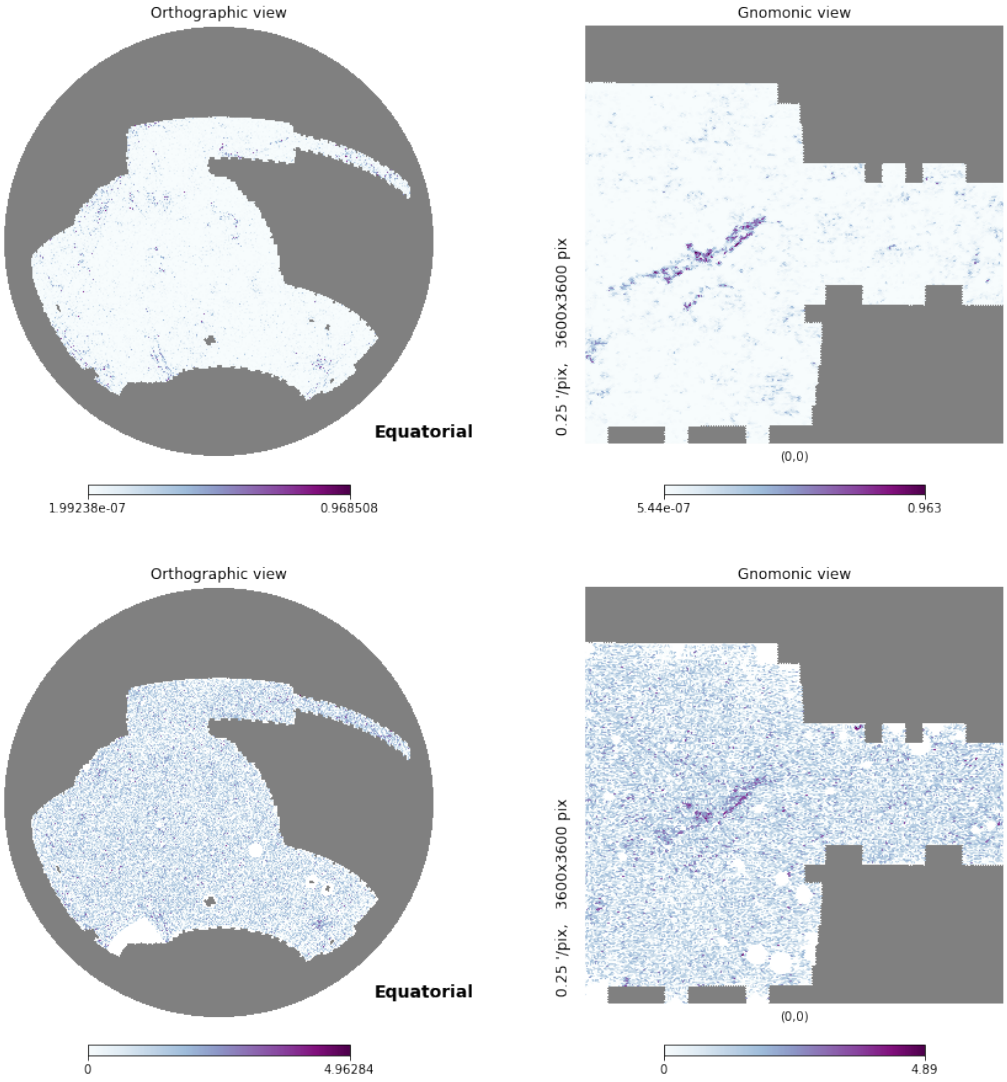


Figure 9.6: Measurements of nebulosity in our footprint (top) and counts of super-spreader objects (bottom) which have drastically too large of flux curves fit to the object. Zoom-ins of a specific region are shown in the right column. There appears to be some spatial correlation of signals.

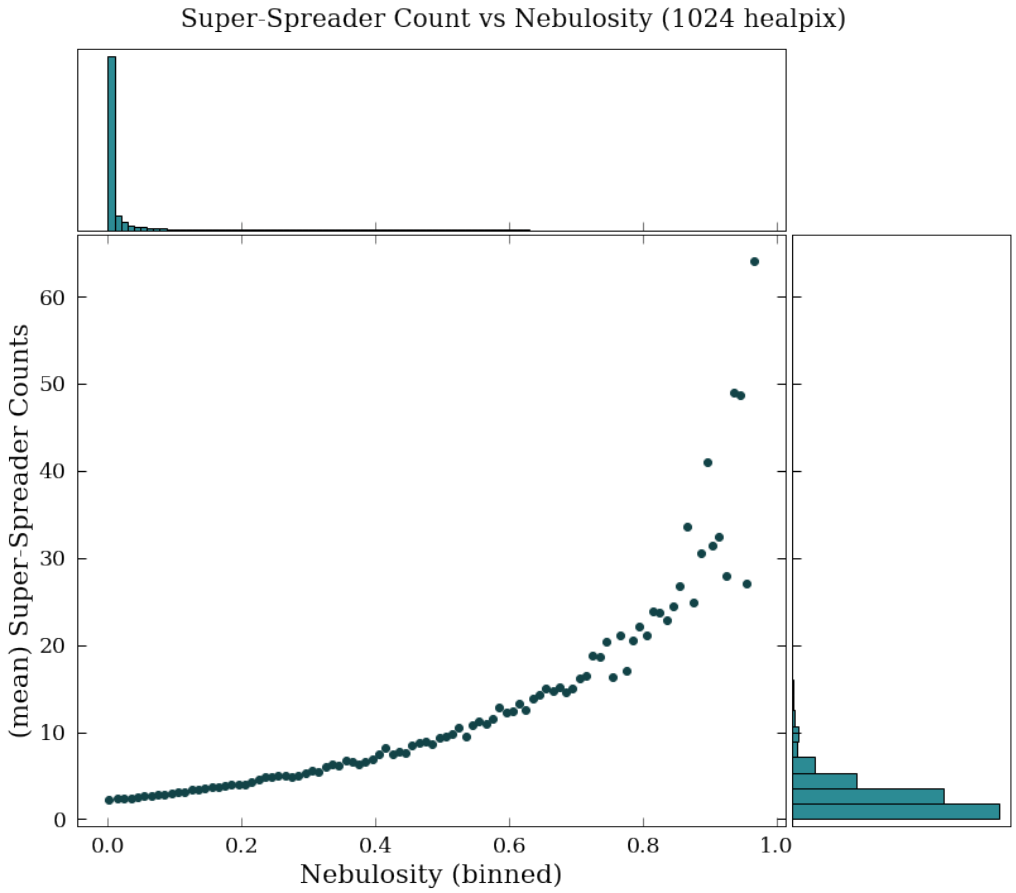


Figure 9.7: The correlations between super-spreader object counts and nebulosity values at an N=1024 Healpix resolution. There is a clear correlation between the two suggesting that Galactic Cirrus can cause catastrophic failures in our photometric measurements pipeline creating super-spreader objects.

task.

The main question that we were interested in answering was whether the nebulosity map has a correlation with measured over(and under) galaxy density, and thus needs to be accounted for in the galaxy systematics re-weighting procedure, section 9.1. An attempt was made to account for the Cirrus maps, however, due to the highly non-linear distribution of nebulosity values, the incorporation of them into the Iterative Systematics Decontamination (ISD) was unviable. It was decided then, to use nebulosity as a mask instead. A nebulosity value of $> 50\%$ was found to have significant cirrus, but only contributed to masking 1% of the pixels in our footprint at a resolution of N=4096 Healpixels.

# Part IV

# Outlook and Conclusion

# 10

# Outlook and Conclusion

Here, I will provide an examination of limitations of our SSI methodology, some expanded uses for future surveys, an outlook into SSI in the generation of survey, and a conclusion.

## 10.1 Limitations

While we made incredible changes in our SSI techniques from the first iteration of the pipeline in Y1 to it's final methodology in Y6, there are still some limitations to it which will be enumerated here.

- *Realism of the Injections:* The sources that we inject into our images are model fits of galaxies, not real images. While I was able to upgrade the architecture to inject real images, we faced a myriad of problems with the technique including accounting for noise and extraneous objects in the images. Ultimately, we decided not to inject real images

for our Y6 SSI methodology. The limitation of injecting model fits is a lack of sampling true galaxy morphology. Our results and how well we can use SSI to estimate the photometry of real objects is ultimately bounded by the model that we use for the fits.

- *Cosmic Variance of the Deep Fields* Another major limitation is that we are sampling our injections from just .1% of the footprint, leading to an issue of cosmic variance. We do test how well our injection sample matches the GOLD sample, with very good agreement, but there are still deviations. These could be due in part to variance. Furthermore, we have found evidence that objects bright in the g-band but dim in other bands are over-represented in our injection sample. The Y6 Deep Fields did expand to $\sim$2x the area of Y3 DF, an effort that I helped with by observing. But in the end, the timing of critical path projects was such that we did not use this for our input catalog. As previously stated, we did find very good agreement between our sample and the GOLD, so postponing the run wasn't justified.

- *Computing power:* A huge limitation in our technique is the massive amount of computing power needed to complete it. We are essentially reprocessing the whole footprint through most of the image processing pipeline, with the additional step of injecting into all of the images in the middle. This takes a huge amount of computational allocation and real time and effort. In fact, with larger surveys, such as LSST, injecting onto the single-epoch images just won't be feasible, they will need to be done on the coadd level.

- *Non-inherited Attributes* Due to our injection methodology, there are some attributes that we can't make a statement about such as the PSF modeling. When we inject into an image, we use the PSF that is already modeled for the image and take it as truth. There is no ability for us to make a statement about its error or bias.

## 10.2 Outlook

### Other Surveys Using SSI

As I see it, DES has really been at the forefront of showcasing the utility and criticality of SSI to its cosmological science. We were the first, with Y3 SSI, to use the method directly to help constrain cosmology. It is touched throughout many of the individual projects and applications that make up the key project and beyond. We showed in Y6 that we can optimize it for specific science cases by creating new injection schemes favoring specific samples of objects to be injected. It's been clear that SSI should be (and has been) worked into the standard playbook of redshift galaxy surveys like our own. And in fact, future generations of surveys have already starting building SSI into their data management plans.

The Rubin Observatory Legacy Survey of Space and Time (LSST) is currently in its commissioning effort and will be coming online soon with a new generation of surveys. LSST will collect data for 10 years, across 18,000 sq deg of sky. The r-band limiting magnitudes in single-epoch images is projected to be 24.5, and an incredible 27.8 in coadd images. With the incredible precision that they will measure at, in cosmic shear for example, SSI will be a critical component to their calibration and systematics control efforts.

LSST is planning on mainly doing SSI in the coadd images instead of the single-epochs, as the computational expense of SE image injection is just too large. They have shown that they can achieve the results that they need by injecting into the coadds. In addition, they have spent a lot of effort creating an SSI methodology that is both integrated into their data processing pipeline from the start, and usable by individual contributors. Neither of which we achieved in DES. Integrating it into the data processing stack from the start ensures that your SSI is processed in

exactly the same manner as the real images, it also allows you to use it as a diagnostic for your image processing pipeline as you are processing real data and in real time. Having a very user friendly system also allows individual science groups to use SSI for their specific applications. They can create the data-set that is uniquely beneficial to them, and do the SSI on their own time.

## Expanded Uses of SSI

- *Non-grid Configurations & Blending:* We inject onto a grid specifically, so that we don't create any SSI blending but you can imagine that actually you want to do the opposite. You could study the effects of blending, and object detection in different scenarios through SSI. There are other types of geometries you might want to consider as well, such as clustering or creating a dwarf galaxy.

- *As a measurement of how the presence of LSS effects object detection:* A really interesting use case for SSI is to measure how the presence of Large-Scale Structure affects our detection of galaxies. There can be a bias in the detection of galaxies due to the presence of other galaxies, specifically the observed number density depends on the true number density. This would be a type of weight that needs to be measured and accounted for, which SSI could aid in.

- *As Randoms:* Another use of SSI that wasn't talked about too much here, is the use of SSI sources as randoms for correlation function measurements. In fact, in DES SSI Y1, they did show that you could use the detected sources as randoms in order to suppress systematic noise.

- *Create Weight Maps from the Injections Themselves:* I showcased an application of SSI to validate whether the galaxy weight maps were

correcting the survey properties adequately enough, or if there were unaccounted for systematics still. One could imagine though, that you can use the SSI detections directly to create the weight maps that correct for non cosmological influences on the observed number density of stars and galaxies due to systematics.

## 10.3 Conclusion

Presented here in this thesis was the Dark Energy Survey's (DES) Synthetic Source Injection (SSI) methodology and applications to precision cosmology for our Y6 analysis of large-scale structure. The methodology is predicated on injecting models of real objects obtained from our very high signal-to-noise Deep Field observations into our single-epoch wide field images which are then processed identically to the original wide images. Inherent to this methodology, is that the synthetic sources automatically inherit the same systematics of the real wide field data, a highly sought after achievement for many systematics modeling pipelines that is nearly impossible to achieve from forward modeling techniques alone. After processing the images through the full image processing pipeline, we are left with measured wide field properties of the DF injected sources. With the measured catalogs in combination with the truth catalogs of the injected source's original photometry, we obtain a Monte Carlo sampling of the survey transfer function.

Our SSI technique touches many aspects of the cosmological analysis. There are four main ways that we do this: as a validation or test of a process, as a diagnostic tool and outlier finder, as a calibration technique, and as a measurement technique. We were able to test whether the image processing pipeline and the re-weighting of galaxies in order to correct for systematics were working correctly. We found populations of objects which are subject to catastrophic fitting failures and identified a method

for finding these objects based on their properties and flagging them in our science sample. We used the wide field photometric measurements of DF objects to calibrate the photometry for the weak lensing galaxy samples by providing more photometric information than is in the wide field photometry alone. Finally, we estimated the completeness curves for DES, and measured the magnification bias coefficient of the lens galaxy sample.

All of these combine to aid in the calculation and validation of our 3x2pt analysis and consequentially our measurement of cosmological parameter constraints. Specifically, through the photometric redshift calibration of the weak lensing sources and the magnification bias estimate for the lens galaxy samples. Both of which are critical to the measurements of the three 2-point correlation functions, cosmic shear, galaxy clustering and galaxy-galaxy lensing, from which we constrain cosmological parameters.

This methodology was first introduced in Y1 as a proof-of-concept. In Y3, of which I joined at the end, we showed the first use of SSI to directly calibrate the cosmological measurements from a WF survey. Large improvements to the methodology had been made between Y1 and Y3. The continued refinement and expansion of the methodology from Y3 to Y6 was presented here and was lead by myself and Brian Yanny. Specifically, we improved our mirroring of the WF image processing pipeline to now fully recreate it. We refactored our code-base to be able to run our SSI at multiple super-computing centers, minimizing wall time and maximizing allocations. We also developed a new injection scheme that injects sources which are preferentially more useful to the cosmological analyses. All of our updates were focused on creating a methodology and results that would have the largest impact on our down-stream analyses and our cosmological parameter constraints through our Large-Scale Structure analysis.

Through our six years of using SSI as a fundamental tool in our cosmo-

logical science, we have proven its indispensability. We have paved the way for other surveys to start using the tool and incorporating it into their pipelines from the start. And we have already seen advancements from the next generation of surveys in the manner that SSI is done, by way of building it into the data management plan from the start and creating tools that individual contributors and analysis teams are able to interface with themselves in order to utilize SSI for their particular goals. As our surveys push deeper, and into larger data sets and more precise measurements, like that of cosmic shear at a 1% level, SSI will be (and already has become) a critical calibration tool that is essential for cosmological research.

# Part V

# Appendices

# 10

# Bibliography

[DES, 2017] (2017).

[Abbott et al., 2022] Abbott, T., Aguena, M., Alarcon, A., et al. (2022). Dark energy survey year 3 results: Cosmological constraints from galaxy clustering and weak lensing. *Physical Review D*, 105(2).

[Abbott et al., 2023] Abbott, T., Aguena, M., Alarcon, A., et al. (2023). Dark energy survey year 3 results: Constraints on extensions to $\lambda$CDM with weak lensing and galaxy clustering. *Physical Review D*, 107(8).

[Abbott et al., 2021] Abbott, T. M. C., Adamó w, M., Aguena, M., et al. (2021). The dark energy survey data release 2. *The Astrophysical Journal Supplement Series*, 255(2):20.

[Alarcon et al., 2021] Alarcon, A., Gaztanaga, E., Eriksen, M., et al. (2021). The PAU Survey: an improved photo-z sample in the COSMOS field. *Monthly Notices of the Royal Astronomical Society*, 501(4):6103–6122.

[Amon et al., 2022] Amon, A., Gruen, D., Troxel, M., et al. (2022). Dark energy survey year 3 results: Cosmology from cosmic shear and robustness to data calibration. *Physical Review D*, 105(2).

[and A. G. A. Brown et al., 2018] and A. G. A. Brown, Vallenari, A., Prusti, T., et al. (2018). igaia/i data release 2. *Astronomy &amp Astrophysics*, 616:A1.

[and T. Prusti et al., 2016] and T. Prusti, de Bruijne, J. H. J., Brown, A. G. A., et al. (2016). Theigaia/imission. *Astronomy &amp Astrophysics*, 595:A1.

[Arp, 1998] Arp, H. (1998). *Seeing Red: Redshifts, Cosmology, and Academic Science*. Apeiron.

[Bertin, 2006] Bertin, E. (2006). Automatic Astrometric and Photometric Calibration with SCAMP. In Gabriel, C., Arviset, C., Ponz, D., and Enrique, S., editors, *Astronomical Data Analysis Software and Systems XV*, volume 351 of *Astronomical Society of the Pacific Conference Series*, page 112.

[Bertin et al., 2002] Bertin, E., Mellier, Y., Radovich, M., et al. (2002). The TERAPIX Pipeline. In Bohlender, D. A., Durand, D., and Handley, T. H., editors, *Astronomical Data Analysis Software and Systems XI*, volume 281 of *Astronomical Society of the Pacific Conference Series*, page 228.

[Burke et al., 2017] Burke, D. L., Rykoff, E. S., Allam, S., et al. (2017). Forward global photometric calibration of the dark energy survey. *The Astronomical Journal*, 155(1):41.

[Chang et al., 2015] Chang, C., Busha, M. T., Wechsler, R. H., et al. (2015). MODELING THE TRANSFER FUNCTION FOR THE DARK ENERGY SURVEY. *The Astrophysical Journal*, 801(2):73.

[Chen et al., 2023] Chen, M., Wang, J. J., Brandt, T. D., et al. (2023). Post-processing CHARIS integral field spectrograph data with scppyklip/scp. *RAS Techniques and Instruments*, 2(1):620–636.

[Dallant et al., 2023] Dallant, J., Langlois, M., Flasseur, O., and Éric Thiébaut (2023). Pacome: Optimal multi-epoch combination of direct imaging observations for joint exoplanet detection and orbit estimation.

[De Vicente et al., 2016] De Vicente, J., Sánchez, E., and Sevilla-Noarbe, I. (2016). DNF – Galaxy photometric redshift by Directional Neighbourhood Fitting. *Monthly Notices of the Royal Astronomical Society*, 459(3):3078–3088.

[Dodelson and Schmidt, 2021] Dodelson, S. and Schmidt, F. (2021). *Modern cosmology*. Academic Press.

[Drlica-Wagner et al., 2018] Drlica-Wagner, A., Sevilla-Noarbe, I., Rykoff, E. S., et al. (2018). Dark energy survey year 1 results: The photometric data set for cosmology. *The Astrophysical Journal Supplement Series*, 235(2):33.

[Elvin-Poole et al., 2023] Elvin-Poole, J., MacCrann, N., Everett, S., et al. (2023). Dark energy survey year 3 results: magnification modelling and impact on cosmological constraints from galaxy clustering and galaxy–galaxy lensing. *Monthly Notices of the Royal Astronomical Society*, 523(3):3649–3670.

[Everett et al., 2022] Everett, S., Yanny, B., Kuropatkin, N., et al. (2022). Dark energy survey year 3 results: Measuring the survey transfer function with balrog. *The Astrophysical Journal Supplement Series*, 258(1):15.

[Gatti et al., 2021a] Gatti, M., Giannini, G., Bernstein, G. M., et al. (2021a). Dark energy survey year 3 results: clustering redshifts – calibration of the weak lensing source redshift distributions with iredMaGiC/i and BOSS/eBOSS. *Monthly Notices of the Royal Astronomical Society*, 510(1):1223–1247.

[Gatti et al., 2021b] Gatti, M., Sheldon, E., Amon, A., et al. (2021b). Dark energy survey year 3 results: weak lensing shape catalogue. *Monthly Notices of the Royal Astronomical Society*, 504(3):4312–4336.

[Gorski et al., 2005] Gorski, K. M., Hivon, E., Banday, A. J., et al. (2005). HEALPix: A framework for high-resolution discretization and fast analysis of data distributed on the sphere. *The Astrophysical Journal*, 622(2):759–771.

[Hartley et al., 2021] Hartley, W. G. et al. (2021). Dark energy survey year 3 results: Deep field optical + near-infrared images and catalogue. *Monthly Notices of the Royal Astronomical Society*, 509(3):3547–3579.

[Huang et al., 2017] Huang, S., Leauthaud, A., Murata, R., et al. (2017). Characterization and photometric performance of the Hyper Suprime-Cam Software Pipeline. *Publications of the Astronomical Society of Japan*, 70(SP1):S6.

[Hubble, 1929] Hubble, E. (1929). A relation between distance and radial velocity among extra-galactic nebulae. *Proceedings of the National Academy of Sciences*, 15(3):168–173.

[Huterer et al., 2015] Huterer, D., Kirkby, D., Bean, R., et al. (2015). Growth of cosmic structure: Probing dark energy beyond expansion. *Astroparticle Physics*, 63:23–41.

[Jarvis et al., 2020] Jarvis, M., Bernstein, G. M., Amon, A., et al. (2020). Dark energy survey year 3 results: point spread function modelling. *Monthly Notices of the Royal Astronomical Society*, 501(1):1282–1299.

[Jarvis et al., 2016] Jarvis, M., Sheldon, E., Zuntz, J., et al. (2016). The DES science verification weak lensing shear catalogues. *Monthly Notices of the Royal Astronomical Society*, 460(2):2245–2281.

[Jarvis et al., 2012] Jarvis, M. J., Bonfield, D. G., Bruce, V. A., et al. (2012). The VISTA Deep Extragalactic Observations (VIDEO) survey. *Monthly Notices of the Royal Astronomical Society*, 428(2):1281–1295.

[Juillard et al., 2023] Juillard, S., Christiaens, V., and Absil, O. (2023). Inverse-problem versus principal component analysis methods for angular differential imaging of circumstellar disks. the mustard algorithm. *Astronomy &amp Astrophysics*.

[Kong et al., 2020] Kong, H., Burleigh, K. J., Ross, A., et al. (2020). Removing imaging systematics from galaxy clustering measurements with Obiwan: application to the SDSS-IV extended Baryon Oscillation Spectroscopic Survey emission-line galaxy sample. *Monthly Notices of the Royal Astronomical Society*, 499(3):3943–3960.

[Laigle et al., 2016] Laigle, C., McCracken, H. J., Ilbert, O., et al. (2016). The cosmos2015 catalog: Exploring the $1 < z < 6$ universe with half a million galaxies. *The Astrophysical Journal Supplement Series*, 224(2):24.

[Le Fèvre, O. et al., 2013] Le Fèvre, O., Cassata, P., Cucciati, O., et al. (2013). The vimos vlt deep survey final data release: a spectroscopic sample of 35 galaxies and agn out to z  6.7 selected with 17.5 <= iab <= 24.75. *A&A*, 559:A14.

[Lilly et al., 2009] Lilly, S. J., Brun, V. L., Maier, C., et al. (2009). The zcosmos 10k-bright spectroscopic sample*. *The Astrophysical Journal Supplement Series*, 184(2):218.

[Low et al., 1984] Low, F. J., Beintema, D. A., Gautier, T. N., et al. (1984). Infrared cirrus: new components of the extended infrared emission. , 278:L19–L22.

[Masters et al., 2017] Masters, D. C., Stern, D. K., Cohen, J. G., et al. (2017). The complete calibration of the color–redshift relation (c3r2) survey: Survey overview and data release 1. *The Astrophysical Journal*, 841(2):111.

[McClure et al., 1985] McClure, R. D., Hesser, J. E., Stetson, P. B., and Stryker, L. L. (1985). Ccd photometry of the sparse halo cluster e 3. *Publications of the Astronomical Society of the Pacific*, 97(594):665.

[McCracken, H. J. et al., 2012] McCracken, H. J., Milvang-Jensen, B., Dunlop, J., et al. (2012). Ultravista: a new ultra-deep near-infrared survey in cosmos. *A&A*, 544:A156.

[Morganson et al., 2018] Morganson, E., Gruendl, R. A., Menanteau, F., et al. (2018). The dark energy survey image processing pipeline. *Publications of the Astronomical Society of the Pacific*, 130(989):074501.

[Muir et al., 2020] Muir, J., Bernstein, G. M., Huterer, D., et al. (2020). Blinding multiprobe cosmological experiments. *Monthly Notices of the Royal Astronomical Society*, 494(3):4454–4470.

[Myles et al., 2021] Myles, J., Alarcon, A., Amon, A., et al. (2021). Dark energy survey year 3 results: redshift calibration of the weak lensing source galaxies. *Monthly Notices of the Royal Astronomical Society*, 505(3):4249–4277.

[NASA, 2012] NASA (2012).

[NOIRlab, 2023] NOIRlab (2023). Dark energy camera (decam).

[Paillassa et al., 2020] Paillassa, M., Bertin, E., and Bouy, H. (2020). MAXIMASK and MAXITRACK: Two new tools for identifying contaminants in astronomical images using convolutional neural networks. *Astronomy &amp Astrophysics*, 634:A48.

[Porredon et al., 2021] Porredon, A., Crocce, M., Fosalba, P., et al. (2021). Dark energy survey year 3 results: Optimizing the lens sample in a combined galaxy clustering and galaxy-galaxy lensing analysis. *Physical Review D*, 103(4).

[Prat et al., 2022] Prat, J., Blazek, J., Sá nchez, C., et al. (2022). Dark energy survey year 3 results: High-precision measurement and modeling of galaxy-galaxy lensing. *Physical Review D*, 105(8).

[Rodrí guez-Monroy et al., 2022] Rodrí guez-Monroy, M., Weaverdyck, N., Elvin-Poole, J., et al. (2022). Dark energy survey year 3 results: galaxy clustering and systematics treatment for lens galaxy samples. *Monthly Notices of the Royal Astronomical Society*, 511(2):2665–2687.

[Rowan-Robinson, 2004] Rowan-Robinson, M. (2004). *Cosmology*. Clarendon Press - Oxford.

[Rowe et al., 2015] Rowe, B., Jarvis, M., Mandelbaum, R., et al. (2015). Galsim: The modular galaxy image simulation toolkit.

[Rozo et al., 2016] Rozo, E., Rykoff, E. S., Abate, A., et al. (2016). redMaGiC: selecting luminous red galaxies from the DES Science Verification data. *Monthly Notices of the Royal Astronomical Society*, 461(2):1431–1450.

[Ryden, 2003] Ryden, B. (2003). *Introduction to Cosmology*. Pearson Education Inc.

[Sá nchez et al., 2022] Sá nchez, C., Prat, J., Zacharegkas, G., et al. (2022). Dark energy survey year 3 results: Exploiting small-scale information with lensing shear ratios. *Physical Review D*, 105(8).

[Scodeggio, M. et al., 2018] Scodeggio, M., Guzzo, L., Garilli, B., et al. (2018). The vimos public extragalactic redshift survey (vipers) - full spectroscopic data and auxiliary information release (pdr-2). *A&A*, 609:A84.

[Secco et al., 2022] Secco, L., Samuroff, S., Krause, E., et al. (2022). Dark energy survey year 3 results: Cosmology from cosmic shear and robustness to modeling uncertainty. *Physical Review D*, 105(2).

[Serjeant, 2010] Serjeant, S. (2010). *Observational Cosmology*. Cambridge University Press.

[Sevilla-Noarbe et al., 2021] Sevilla-Noarbe, I., Bechtol, K., Kind, M. C., et al. (2021). Dark energy survey year 3 results: Photometric data set for cosmology. *The Astrophysical Journal Supplement Series*, 254(2):24.

[Shandonay et al., 2022] Shandonay, A., Morgan, R., Bechtol, K., et al. (2022). Expediting DECam multimessenger counterpart searches with convolutional neural networks. *The Astrophysical Journal*, 925(1):44.

[Sheldon et al., 2020] Sheldon, E. S., Becker, M. R., MacCrann, N., and Jarvis, M. (2020). Mitigating shear-dependent object detection biases with metacalibration. *The Astrophysical Journal*, 902(2):138.

[Suchyta et al., 2016] Suchyta, E., Huff, E. M., Aleksić , J., et al. (2016). No galaxy left behind: accurate measurements with the faintest objects in the dark energy survey. *Monthly Notices of the Royal Astronomical Society*, 457(1):786–808.

[Planck Collaboration et al., 2020] Planck Collaboration, Aghanim, N., Akrami, Y., et al. (2020). iplanck/i2018 results. *Astronomy &amp Astrophysics*, 641:A6.

[The Dark Energy Survey Collaboration, 2018] The Dark Energy Survey Collaboration (2018). The dark energy survey: Data release 1. *The Astrophysical Journal Supplement Series*, 239(2):18.

[Valentino et al., 2021] Valentino, E. D., Mena, O., Pan, S., et al. (2021). In the realm of the hubble tension—a review of solutions*. *Classical and Quantum Gravity*, 38(15):153001.

[Vittorio, 2018] Vittorio, N. (2018). *Cosmology*. CRC Press.